UNIVERSIDAD NACIONAL AUTÓNOMA DE MEXICO

DOCTORADO EN CIENCIAS FÍSICAS
INSTITUTO DE FÍSICA

ANALYTICALLY-SUPPORTED OPTIMAL DESIGN OF HYBRID PHOTONIC-PLASMONIC CRYSTALS USING MACHINE LEARNING ALGORITHMS

TESIS
QUE PARA OPTAR POR EL GRADO DE:
DOCTOR EN CIENCIAS FÍSICAS

PRESENTA:
M. EN C. JORGE ALBERTO PERALTA ÁNGELES

DR. JORGE ALEJANDRO REYES ESQUEDA
INSTITUTO DE FÍSICA

DRA. CITLALI SÁNCHEZ AKÉ
INSTITUTO DE CIENCIAS APLICADAS Y TECNOLOGÍA

DR. ALEJANDRO VÁSQUEZ ARZOLA
INSTITUTO DE FÍSICA

CIUDAD UNIVERSITARIA, CDMX, MAYO 2022

1. Datos del alumno
Peralta
Ángeles
Jorge Alberto
55 8174 0778
Universidad Nacional Autónoma de México
Facultad de Ciencias
Física
306089190

2. Datos del tutor
Dr.
Jorge Alejandro
Reyes
Esqueda

3. Datos del sinodal 1
Dr.
Víctor Manuel
Coello
Cárdenas

4. Datos del sinodal 2
Dr.
Augusto
García
Valenzuela

5. Datos del sinodal 3
Dr.
Roberto de Jesús
León
Montiel

6. Datos del sinodal 4
Dr.
Doroteo
Mendoza
López

7. Datos del trabajo escrito
Analytically-supported optimal design of hybrid photonic plasmonic crystals using machine learning algorithms.
108 p.
2022

posgrado en ciencias físicas
u n a m

MTRA. IVONNE RAMÍREZ WENCE
DIRECTORA GENERAL DE ADMINISTRACIÓN ESCOLAR
UNIVERSIDAD NACIONAL AUTÓNOMA DE MÉXICO
PRESENTE

Con fecha 27 de mayo (Día mes) del 2022 (año), le informo que después de haber revisado el trabajo titulado: Analytically-supported optimal design of hybrid photonic-plasmonic crystals using machine learning algorithms

presentado por el alumno (a) Jorge Alberto Peralta Ángeles

del Posgrado en Ciencias Físicas, considero que Sí (SI / NO) reúne los méritos necesarios para obtener el grado de Doctor (Maestro / Maestra / Doctor / Doctora) en Ciencias (Física (Física / Física Médica)).

ATENTAMENTE

Dr. Jorge Alejandro Reyes Esqueda
GRADO, NOMBRE OFICIAL **COMPLETO** Y FIRMA

REEJ720614MX9
RFC CON HOMOCLAVE

Instituto de Física, UNAM
LUGAR DE TRABAJO (ENTIDAD ACADÉMICA O INSTITUCIÓN)

21 años
ANTIGÜEDAD EN LA UNAM

reyes@fisica.unam.mx 55 5622-5184
CORREO ELECTRÓNICO Y TELÉFONO

posgrado en ciencias físicas
unam

MTRA. IVONNE RAMÍREZ WENCE
DIRECTORA GENERAL DE ADMINISTRACIÓN ESCOLAR
UNIVERSIDAD NACIONAL AUTÓNOMA DE MÉXICO
PRESENTE

Con fecha 08 de junio del 2022 le informo que después de haber
Día mes año

revisado el trabajo titulado: _ ANALYTICALLY-SUPPORTED OPTIMAL DESIGN OF HYBRID PHOTONIC-PLASMONIC CRYSTALS USING MACHINE LEARNING ALGORITHMS

presentado por el alumno (a) Jorge Alberto Peralta Angeles

del Posgrado en Ciencias Físicas, considero que SI reúne los méritos
(SI / NO)

necesarios para obtener el grado de _Doctor en Ciencias
(Maestro / Maestra / Doctor / Doctora)

(Física).
(Física / Física Médica)

ATENTAMENTE V. Coello
Dr. Víctor Manuel Coello Cárdenas
COCV720909613

CICESE, Unidad Monterrey
LUGAR DE TRABAJO (ENTIDAD ACADÉMICA O INSTITUCIÓN)

vcoello@cicese.mx (81) 11788392, (646) 175 05 00
CORREO ELECTRÓNICO Y TELÉFONO

posgrado en ciencias físicas
unam

MTRA. IVONNE RAMÍREZ WENCE
DIRECTORA GENERAL DE ADMINISTRACIÓN ESCOLAR
UNIVERSIDAD NACIONAL AUTÓNOMA DE MÉXICO
PRESENTE

Con fecha 01 (Día) 06 (mes) del 2022 (año), le informo que después de haber revisado el trabajo titulado: ANALYTICALLY-SUPPORTED OPTIMAL DESIGN OF HYBRID PHOTONIC-PLASMONIC CRYSTALS USING MACHINE LEARNING ALGORITHMS

presentado por el alumno (a) JORGE ALBERTO PERALTA ÁNGELES

del Posgrado en Ciencias Físicas, considero que Si (SI / NO) reúne los méritos necesarios para obtener el grado de Doctor (Maestro / Maestra / Doctor / Doctora) en Ciencias (Físicas (Física / Física Médica)).

ATENTAMENTE

Dr. Augusto García Valenzuela Augusto García V.
GRADO, NOMBRE OFICIAL **COMPLETO** Y FIRMA

GAVA6711084Y6
RFC CON HOMOCLAVE

Instituto de Ciencias Aplicadas y Tecnología
LUGAR DE TRABAJO (ENTIDAD ACADÉMICA O INSTITUCIÓN)

26 años
ANTIGÜEDAD EN LA UNAM

augusto.garcia@icat.unam.mx 56228602 ext. 1145
CORREO ELECTRÓNICO Y TELÉFONO

pcf
posgrado en ciencias físicas
unam

MTRA. IVONNE RAMÍREZ WENCE
DIRECTORA GENERAL DE ADMINISTRACIÓN ESCOLAR
UNIVERSIDAD NACIONAL AUTÓNOMA DE MÉXICO
PRESENTE

Con fecha __10 de junio______ del _2022_, le informo que después de haber
Día mes año

revisado el trabajo titulado: _ANALYTICALLY-SUPPORTED OPTIMAL DESIGN OF HYBRID PHOTONIC-PLASMONIC CRYSTALS USING MACHINE LEARNING ALGORITHMS______________________________

presentado por el alumno (a) JORGE ALBERTO PERALTA ÁNGELES

del Posgrado en Ciencias Físicas, considero que ____SÍ____ reúne los méritos
(SI / NO)

necesarios para obtener el grado de _____Doctor______________ en Ciencias
(Maestro / Maestra / Doctor / Doctora)

(____Física______________).
(Física / Física Médica)

A T E N T A M E N T E

Dr. Doroteo Mendoza López
GRADO, NOMBRE OFICIAL **COMPLETO** Y FIRMA

MELD590909BY8
RFC CON HOMOCLAVE

Instituto de Investigaciones en Materiales, UNAM
LUGAR DE TRABAJO (ENTIDAD ACADÉMICA O INSTITUCIÓN)

40 años
ANTIGÜEDAD EN LA UNAM

CORREO ELECTRÓNICO Y TELÉFONO: doroteo@unam.mx, tel.5511868147

pcf
posgrado en ciencias físicas
unam

MTRA. IVONNE RAMÍREZ WENCE
DIRECTORA GENERAL DE ADMINISTRACIÓN ESCOLAR
UNIVERSIDAD NACIONAL AUTÓNOMA DE MÉXICO
PRESENTE

Con fecha 23 de mayo (Día mes) del 2022 (año), le informo que después de haber revisado el trabajo titulado: Analytically-supported optimal design of hybrid photonic-plasmonic crystals using machine learning algorithms

presentado por el alumno (a) Jorge Alberto Peralta Ángeles

del Posgrado en Ciencias Físicas, considero que SI (SI / NO) reúne los méritos necesarios para obtener el grado de Doctor (Maestro / Maestra / Doctor / Doctora) en Ciencias (Física (Física / Física Médica)).

ATENTAMENTE

DR. ROBERTO DE JESÚS LEÓN MONTIEL
GRADO, NOMBRE OFICIAL **COMPLETO** Y FIRMA

LEMR850515MH2
RFC CON HOMOCLAVE

INSTITUTO DE CIENCIAS NUCLEARES
LUGAR DE TRABAJO (ENTIDAD ACADÉMICA O INSTITUCIÓN)

5 AÑOS
ANTIGÜEDAD EN LA UNAM

roberto.leon@nucleares.unam.mx 55 7903 4193
CORREO ELECTRÓNICO Y TELÉFONO

Agradecimientos

A todas las personas que nacieron y viven en México, porque gracias a todas ellas hay ciencia, educación y conocimiento en este maravilloso país.

A la Universidad Nacional Autónoma de México, por tanta generosidad, por formarme dentro y más allá de las aulas, por darme la oportunidad de pertenecer a ella y por infinitas cosas más.

Al Posgrado en Ciencias Físicas por la formación académica y todo el apoyo brindado para realizar mi proyecto de doctorado.

Al Instituto de Física, por abrirme las puertas y ofrecerme las facilidades que me han permitido desarrollarme académicamente.

Al Consejo Nacional de Ciencia y Tecnología, por el apoyo económico brindado a través de la beca de doctorado.

Al Dr. Jorge Alejandro Reyes Esqueda le agradezco todo el apoyo, la confianza y aportaciones académicas que me ha brindado a lo largo de los años.

A mi Comité Tutor, la Dra. Citlali Sánchez Aké y el Dr. Alejandro Vásquez Arzola por todo el apoyo y retroalimentación que me brindaron para fortalecer mi formación.

A mi sínodo, los doctores Víctor Manuel Coello Cárdenas, Augusto García Valenzuela, Roberto de Jesús León Montiel y Doroteo Mendoza López, por aceptar revisar esta tesis y por las valiosas aportaciones que me ayudaron a enriquecer mi trabajo.

A los doctores Carlos Javier Villagómez Ojeda y Adrián Martínez Rivas por el apoyo en el desarrollo experimental de este trabajo.

A los miembros del Laboratorio Central de Microscopía, Fís. Roberto Hernández Reyes, Arq. Diego Quiterio Vargas, M. en C. Manuel Aguilar Franco, Dr. Samuel Tehuacanero Cuapa, Dr. Carlos Magaña y Verónica Durán Santiago por el apoyo brindado en las sesiones de microscopía electrónica.

Al M. en I. Gerardo Rayo por su apoyo técnico en el Laboratorio de Óptica de Superficies.

Al equipo del Posgrado en Ciencias Físicas, María Isabel Mendoza Romero, Jenira Cáceres, María del Carmen Andrade, Ing. Jazmín Acosta Reza, M. en I. Silvia Núñez Corona, Dr. Alberto Güijosa Hidalgo por toda la ayuda que me dieron desde la maestría,

Al proyecto PAPIIT IN112022.

A mis compañeros y amigos del Laboratorio de Óptica de Superficies, Dr. Oswaldo Sánchez Dena, Fís. Omar Alejandro Velazco Cortés, Dr. Atzin David Ruiz Pérez, M. en C. Emmanuel de la Cruz Piña.

Dedicatoria

Este trabajo se logró gracias a muchas personas que han estado siempre conmigo. Gracias a mis padres por todo lo que me han enseñado, por su apoyo, por su bondad, por su tenacidad y fortaleza ante los retos, por el inconmensurable amor, por los infinitos detalles que los hacen los mejores padres del multiverso.

A mis hermanas y a mi hermano, por todo el apoyo y amor que me dan siempre, por los momentos que hemos pasado juntos y por todos aquellos momentos que nos esperan.

A mis sobrinos, que me han permitido verlos crecer y reír con ellos.

A Rosa, Fernando y Fer, que me han enseñado que la familia también tiene diferentes apellidos.

A mis tías, tíos, primas y primos, gracias por todos esos ratos juntos.

A mis amigos Osgualdro y Omar, por todas las experiencias y risas dentro y fuera del laboratorio, por las pláticas, que no sólo son de física y óptica, y por todas las tazas de café.

A Alejandro por toda la confianza que me ha dado y por todo el apoyo académico y no académico.

A Tycho, por lo que he encontrado sin buscarlo.

A Kar, por nuestro pasado, presente y futuro, por todo lo que aprendemos juntos y por todo lo que nos falta por conocer, por siempre estar conmigo en cada momento y circunstancia, por todo el amoroso apoyo que me da, por todas las pláticas, caminatas y risas compartidas, porque contigo aprendí que las batallas no se libran desde el yo sino desde el nosotros. Gracias por todo.

Contents

List of Figures

Resumen

En este trabajo se presenta un estudio teórico y numérico sobre cristales fotónico-plasmónicos híbridos. Se desarrolla uno modelo analítico general para calcular la estructura de bandas de cristales fotónicos dieléctricos unidimensionales y bidimensionales sobre películas delgadas de oro y plata que soporten la propagación de plasmones polaritones de superficie.

Este modelo es aplicado en cuatro estructuras particulares potencialmente fabricables mediante litografía de haz de electrones. Para cristales fotónico-plasmónicos unidimensionales, las estructuras mencionadas son barras de polimetilmetacrilato (PMMA por sus siglas en inglés) apiladas en dirección al eje x. Para sistemas bidimensionales, las estructuras son arreglos periódicos de columnas de PMMA de sección transversal rectangular y elíptica. Los arreglos periódicos corresponden a tres redes cristalinas bidimensionales: las redes cuadrada, triangular y rectangular.

La validez del modelo teórico propuesto es corroborada calculando la estructura de bandas para dos fracciones de llenado distintas, es decir, para dos tamaños de sección transversal diferentes. Estas estructuras de bandas son equivalentes con la relación de dispersión de plasmones polaritones de superficie en las interfases correspondientes a tales fracciones de llenado.

Con el modelo se estudia el efecto que inducen, en la estructura de bandas, la constante de red y el tamaño de la sección transversal. En los sistemas bidimensionales se producen *bandgaps* completos en la estructura de bandas en redes cristalinas triangulares para algunas fracciones de llenado. Por su parte, en redes cristalinas cuadradas y rectangulares, se producen *bandgaps* parciales para ciertas orientaciones del cristal. Sin embargo, en la red cristalina rectangular, es posible obtener *bandgaps* completos acortando la trayectoria de los puntos de alta simetría.

El modelo analítico es de gran utilidad para calcular las propiedades ópticas a través de la estructura de bandas partiendo las propiedades cristalinas, en cambio, sintonizar la respuesta óptica usándolo puede resultar en un proceso ineficiente. Lo anterior se debe a la intrincada relación entre la respuesta óptica y las propiedades estructurales del sistema.

Para sintonizar la respuesta óptica de estas estructuras, se generaron, con el modelo propuesto, conjuntos de datos variando la constante de red y la fracción de llenado. Estos conjuntos de datos se usaron para entrenar varios algoritmos de *machine learning* para realizar el diseño hacia adelante, es decir, predecir la respuesta óptica en función de las características cristalinas, y para implementar el diseño inverso, es decir, predecir las propiedades estructurales como función de una respuesta óptica objetivo.

Los algoritmos utilizados son capaces de realizar con una precisión alta el diseño hacia adelante, mientras que sólo las redes neuronales artificiales son capaces de implementar el diseño

inverso con una precisión alta. Los resultados obtenidos con los algoritmos de *machine learning* son comparados con los obtenidos a través del modelo teórico, que a su vez son corroborados mediante simulaciones numéricas. Todos estos resultados son compatibles entre sí, lo que infiere que el modelo propuesto es consistente la física estudiada.

En resumen, en el trabajo presentado se proponen herramientas teóricas y numéricas para calcular y sintonizar la respuesta óptica de cristales fotónico-plasmónicos híbridos para aplicaciones potenciales en guías de onda plasmónicas, nanocavidades, espejos, entre otras.

Abstract

In this work, a theoretical and numerical study on hybrid photonic-plasmonic crystals is presented. A general analytical model is developed to calculate the band structure of one- and two-dimensional dielectric photonic crystals on gold and silver thin films supporting surface plasmon polariton propagation.

This model is applied to four particular structures potentially manufacturable by electron beam lithography. For one-dimensional photonic-plasmonic crystals, the structures mentioned are Polymethyl methacrylate (PMMA) rods stacked in the x-axis direction. For two-dimensional systems, the structures are periodic arrays of PMMA columns of a rectangular and elliptical cross-section. The periodic arrays correspond to three two-dimensional crystal lattices: square, triangular and rectangular lattices.

The validity of the proposed theoretical model is corroborated by calculating the band structure for two different filling fractions, that is, for two different cross-section sizes. These band structures are equivalent to the dispersion relation of surface plasmons and polaritons in the polariton dispersion ratio at the interfaces corresponding to such filling fractions.

The model studies the effect that the lattice constant and the size of the cross-section induce on the band structure. In two-dimensional systems, complete bandgaps occur in the band structure in triangular crystal lattices for some filling fractions. On the other hand, in square and rectangular crystal lattices, partial bandgaps are produced for certain orientations of the crystal. However, in the rectangular crystal lattice, it is possible to obtain complete bandgaps by shortening the path of the high symmetry points.

The analytical model is very useful to calculate the optical properties through the band structure starting from the crystalline properties, however, tuning the optical response using it can result in an inefficient process. This is due to the intricate relationship between the optical response and the structural properties of the system.

To tune the optical response of these structures, data sets were generated with the proposed model by varying the lattice constant and the filling fraction. These data sets were used to train various machine learning algorithms to perform forward design, that is, predict the optical response based on crystalline features. Likewise, the generated data sets are used to implement the inverse design, that is, to predict the structural properties as a function of a target optical response.

The algorithms used are capable of performing forward design with high precision, while only artificial neural networks are capable of implementing the inverse design with high precision. The results obtained with the machine learning algorithms are compared with those obtained

through the theoretical model, which in turn are corroborated through numerical simulations. All these results are compatible with each other, which infers that the proposed model is consistent with the studied physics.

In summary, in the presented work theoretical and numerical tools are proposed to calculate and tune the optical response of hybrid photonic-plasmonic crystals for potential applications in plasmonic waveguides, nanocavities, mirrors, among others.

Chapter 1

Introduction

Surface Plasmons Polaritons (SPPs) are electromagnetic waves coupled to charge oscillation at an dielectric-metal interface [1]. One of the main attractions for their study are the potential applications that can be given to them in various scientific and technological disciplines. Among these applications, one of the most outstanding is plasmonic circuits, since the use of light would solve the speed limit of electronics and overcome the diffraction limit of light [1, 2].

Photonic devices are often composed of dielectric elements and their dimensions are sometimes relatively large. In contrast, plasmonic devices can be constructed with dimensions smaller than the wavelength of light. In both cases, it is possible to tune their optical properties from their structural characteristics [3]. The combination of these elements would be a path to a wide variety of possible applications.

The simplest structure for propagating SPPs is a metallic thin film [4, 5, 6, 7]. The excitation and propagation of SPPs is explained by solving Maxwell's equations at the interface formed between the metallic medium and the dielectric medium. At such interfaces, there is good confinement of the electromagnetic field in the direction perpendicular to the propagation but laterally such confinement is very weak.

To control the SPPs propagation there are various types of nanostructures such as metallic thin films, nanoparticle chains, nanowires, grooves, stripes and others have been proposed to guide SPPs [1]. The intention is to achieve the confinement of electromagnetic energy by the nanostructures near the interface beyond the diffraction limit of light [1].

Each of the structures designed to guide SPPs has its advantages and disadvantages, and depending on the application a particular waveguide may be chosen. For example, nanowires have low losses, so they can propagate SPPs over long distances, but in many cases, these waveguides are only straight [1].

In the V-groove metallic waveguide, there are fundamental modes and "higher" modes called channel plasmon modes (CPP). Confinement is achieved at different positions, while the propagation distance is tuned as a function of the groove angle and depth [8, 9], as shown in Fig. 1.1.

Like the groove guide, in wedge waveguides the propagation of SPPs is controlled by the taper angle, where the smaller the angle the more confined the electromagnetic field is. Wedge waveguides are similar to the groove waveguide but in this case, the electromagnetic field is

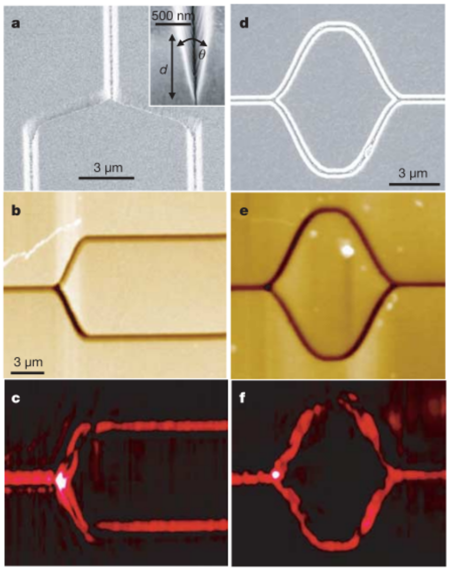

Figure 1.1: Modes in wedge waveguides. Modified from Bozhevolnyi, *et al.*, 2006.

confined at the edge [1, 10], as shown in Fig. 1.2. On the other hand, nanoparticle chains, although they function as waveguides, are not very efficient since they have a high dissipative loss due to their rough surfaces [1].

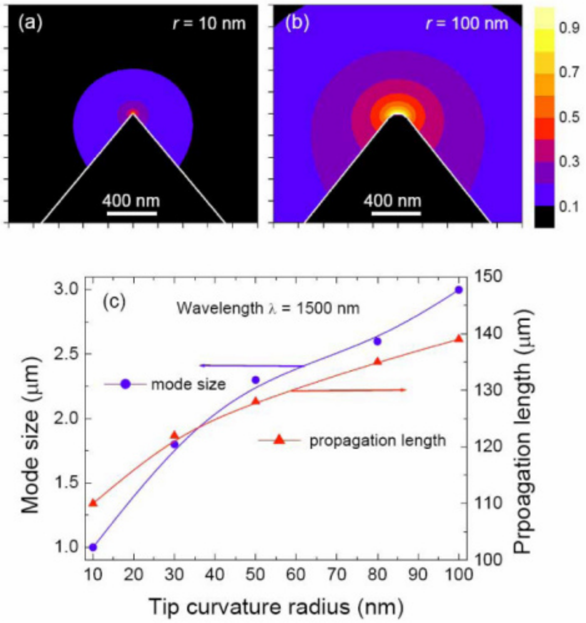

Figure 1.2: Modes in wedge waveguides. Modified from Boltasseva, *et al.*, 2008.

Another way to laterally confine SPPs propagation is with a dielectric stripe over the metallic thin film. These structures, called dielectric-loaded surface plasmon-polariton waveguides, work due to the contrast of effective refractive indexes of the interfaces [11]. Propagation is controlled by adjusting the width and height of the stripe, which in turn changes the effective refractive index [11].

One of the disadvantages of this type of waveguide is the losses introduced by the dielectric. The larger the refractive index and the height of the stripe, the confinement is stronger and the propagation length decreases, since the effective refractive index increases [12], which has been experimentally demonstrated [13].

To avoid losses due to the dielectric on the metal film, some alternatives can be used. One of them is to use a metal film of finite height and width, which allows SPPs to propagate over long distances, which has been studied theoretically and experimentally [14]. Using silver stripes and with certain parameters, the propagation of SPPs over distances greater than 10 mm has been reported [14].

The study of these straight stripes has led to the realization of passive integrated structures. Among these elements are S-bends of varying radii of curvature, sharp angle bends stripes, Y junctions, Mach-Zehnder interferometers, and couplers with variable spacing between the arms [14]. Perhaps the most important contribution of these works is that they demonstrated the possibility of creating plasmonic circuits where propagation occurs over very large extensions compared to the wavelength.

However, these bends are sometimes limited to moderate curvatures due to radiation losses, mainly dielectric-loaded surface plasmon-polariton waveguides since their principle of operation is based on total internal reflection. Photonic crystals, which are structures with a refractive index periodically modulated in space, can modify the density of electromagnetic states inside the structure, forming a photonic bandgap [15].

In these media, waveguides can be constructed by introducing linear defects into the structure [16, 17, 18], as shown in Fig. 1.3. Since they are capable of efficiently reflecting the light incident on them without relying on internal reflection, the defects can guide electromagnetic waves through corners [15]. One of the advantages of this type of photonic system is that losses can be very small over a wide frequency range, even for radios curvature of the order of the wavelength [15].

The existence of an effect analogous to that of photonic bandgaps in plasmonic structures has been demonstrated experimentally [19]. The structures studied are triangular arrays of spaced scatters with a period of 300 nm on a silver thin film. From the experimental results, it was found a bandgap centered at 634.537 nm, with a width of 29.211 nm [19].

Guidance of SPPs in defects fabricated in triangular arrays of metal cylinders on a gold thin film has also been reported [20]. In this case, the authors first show the existence of the photonic bandgap in these periodic arrays and then studies the propagation in linear defects. However, no guiding of SPPs in defects is observed for the $\Gamma - \mathrm{K}$ orientation, but rather in the $\Gamma - \mathrm{M}$ orientation [20], where Γ, K, and M are the high symmetry point of the triangular lattice.

In the same sense, the propagation of SPPs has been studied in linear defects with curves, where it has been observed that, as the angle increases, the losses also do [21]. Likewise, an

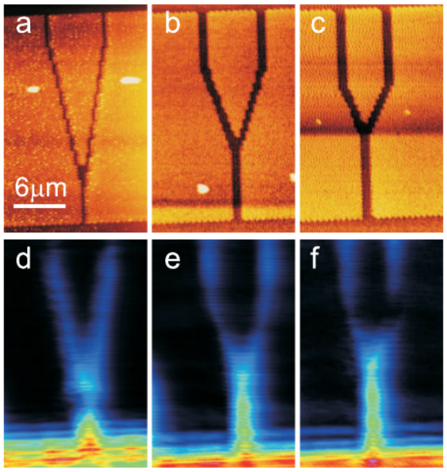

Figure 1.3: Defects in a periodic array. Modified from Radko, *et al.*, 2009.

analogous phenomenon has been experimentally verified in Y junctions, where, with increasing angles, the losses are higher [15].

The problem has also been studied numerically [22]. Using FDTD calculations, the propagation of SPPs in these triangular arrays in the $\Gamma - \mathrm{K}$ and $\Gamma - \mathrm{M}$ orientations has been simulated. The results suggest that the propagation of SPPs in the $\Gamma - \mathrm{K}$ orientation only occurs when the defect is wide enough. The numerical analysis performed has been extended to the bent linear defects, where SPPs guidance also occurs [22].

One of the problems with this type of structure is that complete bandgaps are not always produced. This limits the possibility of propagating SPPs in all orientations of the structure [23]. One of the proposed alternatives is to adiabatically bend a linear defect that propagates SPPs so that the orientation is maintained. Figure 1.4 shows the structure describe above. Experimental and numerical results show efficient guiding of SPPs through the adiabatically curved linear defect [15, 23].

The optical properties of these structures have been extensively studied. In particular, numerical and experimental evidence highlights the influence of period and scatter size [24, 25]. The period is a determining factor in defining the center of the bandgap, which is shifted toward shorter wavelengths for smaller periods. On the other hand, the size of the scatters significantly affects the bandgap width [24, 25]. These numerical and experimental results suggest that the propagation of SPPs can be controlled through the appropriate characteristics of the scatters array.

The metallic photonic crystals just mentioned are effective devices for producing bandgaps, but this effect can also be achieved with dielectric photonic crystals. Numerical and experimental studies have demonstrated the possibility of using dielectric ridge stacks as one-dimensional plasmonic crystals that produce bandgaps in the SPPs dispersion relation [26]. Through stacked PMMA ridges it has been shown that these structures control the propagation of SPPs by reflection.

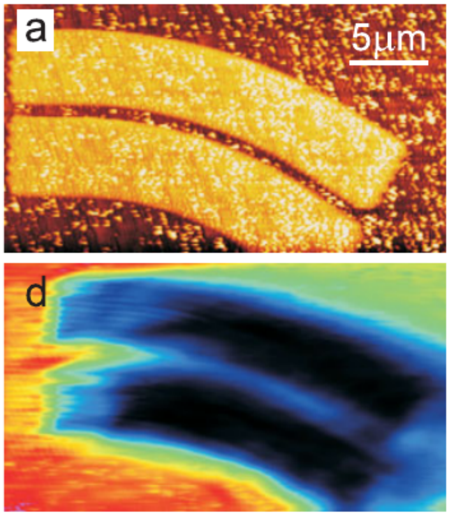

Figure 1.4: Structure adiabatically rotated. Modified from Radko, *et al.*, 2009.

Under this same concept, hybrid photonic-plasmonic crystals have been designed. The reported numerical results show the bandgaps produced by dielectric photonic crystals in a triangular lattice on a silver film [27, 28]. This suggests that they can be applied in a wide range of plasmonic devices such as nanocavities, nanolasers, reflectors or waveguides.

As for the theoretical aspects of the problem, several analytical studies have been implemented to model the optical response of these plasmonic systems. Some of them have been performed under the multiple scattering dipole approach [29], with which the propagation of SPPs in a triangular array is modeled.

Another method that has been used for the theoretical study is based on the Lippmann-Schwinger integral equation [29], which allows calculating the transmission and reflection of SPPs in these structures. In addition, using the homogeneous form of the reduced Rayleigh equation, it is possible to calculate the band structure and study the formation of complete bandgaps [30].

A technique frequently used to calculate the band structure of conventional photonic crystals is the plane-wave expansion method. Although conventionally used for dielectric photonic crystals, it can also be extended to hybrid photonic-plasmonic structures. This technique has been applied to square arrays of silicon columns on an aluminum film, where it has been shown theoretically and experimentally to be possible to produce broad bandgaps using a high refractive index contrast [31].

The design of photonic-plasmonic devices considered so far only addresses the behavior of the optical response as a function of the structural properties of the photonic-plasmonic crystals. This approach is known as «forward design», where the optical response is studied from the composition of the photonic-plasmonic crystal, its crystal lattice, the lattice constant or period, the geometry and size of the scatterers and the filling fraction.

Another approach to designing photonic devices is «inverse design», which consists of recovering the proper structure for a desired optical response [32]. This approach is particularly useful when one wants to tune the optical response of photonic systems. Frequently, this design starts from random parameters and the result is compared with the target optical response, and from this comparison, the parameters are updated [33]. This process known as optimization is carried out iteratively until the expected result is achieved [33], however, it can consume a lot of time and resources.

In contrast to the above, there are novel tools such as machine learning algorithms that allow optimization of the design of photonic structures [32, 33]. These algorithms can be applied in two different ways, first by using the structural parameters to predict the optical response. This is useful to avoid the optimization cycle, which can sometimes be computationally expensive [33]. The second way to use the algorithms is through the inverse design, which would allow to efficiently obtain the structural properties from the objective optical response [32, 33].

This thesis is composed of different sections, in addition to the introduction. In chapter 2, a theoretical model is presented to calculate the band structure and the optical response of hybrid photonic-plasmonic crystals. It starts from the general theory of photonic crystals in two and three dimensions to calculate the band structure using the plane wave expansion method. Subsequently, the theoretical model is proposed to study a general structure of hybrid photonic-plasmonic crystals consisting of a dielectric photonic crystal on a thin film of gold or silver.

The third chapter describes the techniques used to carry out the research. A brief description of the fundamentals of the machine learning algorithms implemented for both, forward and inverse design, is made.

Chapter 4 presents the results of the investigation. First, the results obtained from the analysis of particular structures of hybrid photonic-plasmonic crystals consisting of PMMA photonic crystals on a thin gold or silver film are shown. The analysis is performed for a one-dimensional structure and three two-dimensional structures, considering scatters with two different cross-sections. The effect of the lattice constant and the filling fraction on the properties of bandgap is also studied.

The results obtained by machine learning algorithms for both forward and inverse designs are shown below. These results are compared with those obtained with the analytical model to corroborate its validity. To close the section, the results of the design of hybrid photonic-plasmonic crystals tuned to a target optical response are presented. These designs are done with machine learning algorithms and are supported by numerical simulations.

Finally, the last section presents the conclusions of the work. Also, this work includes an appendix with the experimental techniques that would be used to experimentally corroborate the proposed theoretical model and The the results of the implementation of the experimental setup to perform the optical characterization.

Objectives

General objective

- Develop an efficient methodology to design plasmonic devices based on photonic-plasmonic crystals.

Particular objectives

- Propose a theoretical model to calculate the band structure of plasmonic photonic crystals.
- Study theoretically the optical properties of photonic-plasmonic crystals of different two-dimensional lattices.
- Implement machine learning algorithms to compute the optical properties of two-dimensional photonic-plasmonic crystals.
- Implement machine learning algorithms to optimize the tuning of the optical properties of two-dimensional photonic-plasmonic two-dimensional photonic-plasmonic crystals.
- Verify numerically the correct operation of the proposed plasmonic structures.

Hypothesis

- The plane-wave expansion method allows studying the bandgap structure of photonic-plasmonic systems. Moreover, integrating it with optimization tools, such as machine learning algorithms, allows tuning the bandgap properties in the band structure.

References

[1] Yurui Fang and Mengtao Sun. Nanoplasmonic waveguides: towards applications in integrated nanophotonic circuits. *Light: Science & Applications*, 4(6):e294–e294, 2015.

[2] William L Barnes, Alain Dereux, and Thomas W Ebbesen. Surface plasmon subwavelength optics. *Nature*, 424(6950):824–830, 2003.

[3] Mark L Brongersma and Pieter G Kik. *Surface plasmon nanophotonics*, volume 131. Springer, 2007.

[4] Stefan A. Maier. *Plasmonics: Fundamentals and Applications.* Springer, 2007.

[5] Satoshi Kawata, Motoichi Ohtsu, and Masahiro Irie. *Near-field optics and surface plasmon polaritons*, volume 81. Springer Science & Business Media, 2001.

[6] Anatoly V. Zayats, Igor I. Smolyaninov, and Alexei A. Maradudin. Nano-optics of surface plasmon polaritons. *Physics Reports*, 408(3):131–314, 2005.

[7] H. Raether. *Surface Plasmons.* Springer, Berlin, 1988.

[8] Valentyn S Volkov, Sergey I Bozhevolnyi, Sergio G Rodrigo, Luis Martin-Moreno, Francisco J Garcia-Vidal, Eloise Devaux, and Thomas W Ebbesen. Nanofocusing with channel plasmon polaritons. *Nano letters*, 9(3):1278–1282, 2009.

[9] Sergey I Bozhevolnyi, Valentyn S Volkov, Eloise Devaux, Jean-Yves Laluet, and Thomas W Ebbesen. Channel plasmon subwavelength waveguide components including interferometers and ring resonators. *Nature*, 440(7083):508–511, 2006.

[10] Alexandra Boltasseva, Valentyn S. Volkov, Rasmus B. Nielsen, Esteban Moreno, Sergio G. Rodrigo, and Sergey I. Bozhevolnyi. Triangular metal wedges for subwavelength plasmon-polariton guiding at telecom wavelengths. *Opt. Express*, 16(8):5252–5260, Apr 2008.

[11] B. Steinberger, A. Hohenau, H. Ditlbacher, F. R. Aussenegg, A. Leitner, and J. R. Krenn. Dielectric stripes on gold as surface plasmon waveguides: Bends and directional couplers. *Applied Physics Letters*, 91(8):081111, 2007.

[12] Zhanghua Han and Sergey I Bozhevolnyi. Radiation guiding with surface plasmon polaritons. *Reports on Progress in Physics*, 76(1):016402, dec 2012.

[13] J. Grandidier, S. Massenot, G. Colas des Francs, A. Bouhelier, J.-C. Weeber, L. Markey, A. Dereux, J. Renger, M. U. González, and R. Quidant. Dielectric-loaded surface plasmon polariton waveguides: Figures of merit and mode characterization by image and fourier plane leakage microscopy. *Phys. Rev. B*, 78:245419, Dec 2008.

[14] Pierre Berini. Long-range surface plasmon polaritons. *Adv. Opt. Photon.*, 1(3):484–588, Nov 2009.

[15] Ilya P Radko, Valentyn S Volkov, Jonas Beermann, Andrey B Evlyukhin, Thomas Søndergaard, Alexandra Boltasseva, and Sergey I Bozhevolnyi. Plasmonic metasurfaces for waveguiding and field enhancement. *Laser & Photonics Reviews*, 3(6):575–590, 2009.

[16] Igor A. Sukhoivanov and Igor V. Guryev. *Photonic crystals.* Springer, 2009.

[17] Kazuaki Sakoda. *Optical Properties of Photonic Crystals.* Springer, 2005.

[18] John D. Joannopoulos, Steven G. Johnson, Joshua N. Winn, and Robert D. Meade. *Photonic crystals: molding the flow of light.* Princeton University Press, Princeton,New Jersey, 2008.

[19] S. C. Kitson, W. L. Barnes, and J. R. Sambles. Full photonic band gap for surface modes in the visible. *Phys. Rev. Lett.*, 77:2670–2673, Sep 1996.

[20] Sergey I. Bozhevolnyi, John Erland, Kristjan Leosson, Peter M. W. Skovgaard, and Jørn M. Hvam. Waveguiding in surface plasmon polariton band gap structures. *Phys. Rev. Lett.*, 86:3008–3011, Apr 2001.

[21] Sergey I. Bozhevolnyi, Valentyn S. Volkov, Kristjan Leosson, and Alexandra Boltasseva. Bend loss in surface plasmon polariton band-gap structures. *Applied Physics Letters*, 79(8):1076–1078, 2001.

[22] FI Baida, Daniel Van Labeke, Y Pagani, B Guizal, and M Al Naboulsi. Waveguiding through a two-dimensional metallic photonic crystal. *Journal of microscopy*, 213(2):144–148, 2004.

[23] Ilya P. Radko, Thomas Søndergaard, and Sergey I. Bozhevolnyi. Adiabatic bends in surface plasmon polariton band gap structures. *Opt. Express*, 14(9):4107–4114, May 2006.

[24] VS Volkov, Sergei I Bozhevolnyi, K Leosson, and Alexandra Boltasseva. Experimental studies of surface plasmon polariton band gap effect. *Journal of microscopy*, 210(3):324–329, 2003.

[25] A.-L. Baudrion, J.-C. Weeber, A. Dereux, G. Lecamp, P. Lalanne, and S. I. Bozhevolnyi. Influence of the filling factor on the spectral properties of plasmonic crystals. *Phys. Rev. B*, 74:125406, Sep 2006.

[26] Sukanya Randhawa, María Ujué González, Jan Renger, Stefan Enoch, and Romain Quidant. Design and properties of dielectric surface plasmon bragg mirrors. *Opt. Express*, 18(14):14496–14510, Jul 2010.

[27] Tsung li Liu, Kasey J. Russell, Shanying Cui, and Evelyn L. Hu. Two-dimensional hybrid photonic/plasmonic crystal cavities. *Opt. Express*, 22(7):8219–8225, Apr 2014.

[28] Shereena Joseph and Joby Joseph. Photonic-plasmonic hybrid 2d-pillar cavity for mode confinement with subwavelength volume. *IEEE Photonics Technology Letters*, 31(17):1433–1436, 2019.

[29] T. Søndergaard and S. I. Bozhevolnyi. Vectorial model for multiple scattering by surface nanoparticles via surface polariton-to-polariton interactions. *Phys. Rev. B*, 67:165405, Apr 2003.

[30] M. Kretschmann. Phase diagrams of surface plasmon polaritonic crystals. *Phys. Rev. B*, 68:125419, Sep 2003.

[31] Liang Feng, Ming-Hui Lu, Vitaliy Lomakin, and Yeshaiahu Fainman. Plasmonic photonic crystal with a complete band gap for surface plasmon polariton waves. *Applied Physics Letters*, 93(23):231105, 2008.

[32] Wei Ma, Zhaocheng Liu, Zhaxylyk A. Kudyshev, Alexandra Boltasseva, Wenshan Cai, and Yongmin Liu. Deep learning for the design of photonic structures. *Nature Photonics*, 15(2):77–90, 2021.

[33] Dianjing Liu, Yixuan Tan, Erfan Khoram, and Zongfu Yu. Training deep neural networks for the inverse design of nanophotonic structures. *ACS Photonics*, 5(4):1365–1369, 2018.

Chapter 2

Theoretical model

2.1 General theory for photonic crystals

Photonic crystals are media formed by regular arrays of materials with different refractive indexes so that the dielectric function is periodically modulated in space [1, 2]. They are characterized by a lattice constant, which is the physical dimension of the unit cells of the crystal lattice, that is, the period of the basic stack of the structure, as shown in Fig. 2.1. In general, photonic crystals are classified into one-, two- and three-dimensional crystals depending on the stacking direction [1, 2], shown schematically in the figure above.

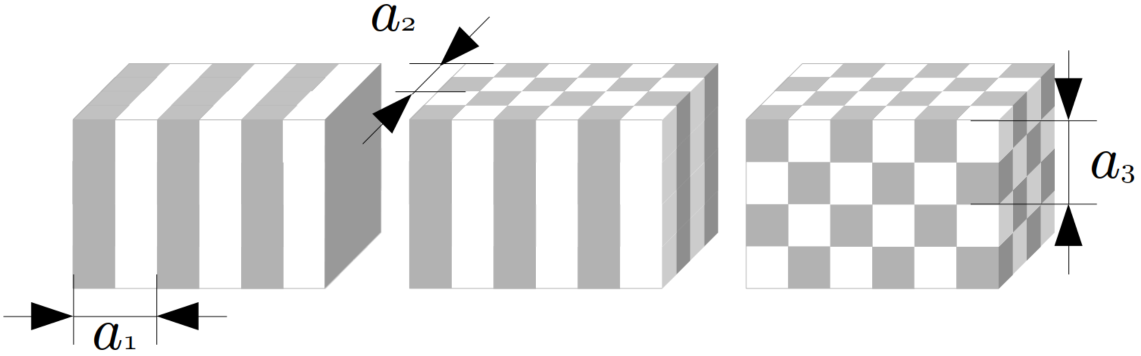

Figure 2.1: One-dimensional, two-dimensional, and three-dimensional photonic crystals with their respective lattice constant in each direction.

It is important to keep in mind that the periodicity of the photonic crystal involves

$$\epsilon(\mathbf{r}+\mathbf{R}) = \epsilon(\mathbf{r}), \tag{2.1.1}$$

where $\mathbf{R}$ are the lattices vectors given by

$$\mathbf{R} = m_1\boldsymbol{a}_1 + m_2\boldsymbol{a}_2 + m_3\boldsymbol{a}_3, \tag{2.1.2}$$

$\boldsymbol{a}_i$ are the elementary lattice vectors of the photonic crystal and m_i are integers, with $i = 1, 2, 3$ [1, 2].

In these optical systems, an interesting phenomenon called photonic bandgap occurs, where light cannot propagate in the photonic crystal in a certain frequency range, that is, "there appears a frequency range where no electromagnetic eigenmode exists" [1]. The above is important because it opens up the possibility of controlling the propagation of light through these structures with the proper design of the photonic crystal.

The study of light in a photonic crystal is carried out with Maxwell's equations, which in matter are expressed by

$$\nabla \cdot \mathbf{D} = \rho_f \tag{2.1.3}$$

$$\nabla \cdot \mathbf{B} = 0 \tag{2.1.4}$$

$$\nabla \times \mathbf{E} = -\frac{\partial \mathbf{B}}{\partial t} \tag{2.1.5}$$

$$\nabla \times \mathbf{H} = \mathbf{j}_f + \frac{\partial \mathbf{D}}{\partial t}. \tag{2.1.6}$$

In addition, the **E** and **D** fields and the **H** and **B** fields are linked through constitutive relations, which for homogeneous, linear and isotropic materials are:

$$\mathbf{D}(\mathbf{r}, t) = \epsilon_0 \epsilon(\mathbf{r}) \mathbf{E}(\mathbf{r}, t), \tag{2.1.7}$$

$$\mathbf{B}(\mathbf{r}, t) = \mu_0 \mu(\mathbf{r}) \mathbf{H}(\mathbf{r}, t). \tag{2.1.8}$$

Assuming that there are no free charges or currents, applying the rotational operator to equation (2.1.5), and considering that $\nabla \times (\nabla \times \mathbf{v}) = \nabla(\nabla \cdot \mathbf{v}) - \nabla^2 \mathbf{v}$, the wave equations for the electric and magnetic fields can be obtained:

$$\frac{1}{\epsilon(\mathbf{r})} \nabla \times \{\nabla \times \mathbf{E}(\mathbf{r}, t)\} = -\frac{\omega^2}{c^2} \mathbf{E}(\mathbf{r}, t), \tag{2.1.9}$$

$$\nabla \times \left\{ \frac{1}{\epsilon(\mathbf{r})} \nabla \times \mathbf{H}(\mathbf{r}, t) \right\} = -\frac{\omega^2}{c^2} \mathbf{H}(\mathbf{r}, t), \tag{2.1.10}$$

whose solutions are of the form

$$\mathbf{E}(\mathbf{r}, t) = \mathbf{E}_0(\mathbf{r}) e^{i\omega t}, \tag{2.1.11}$$

$$\mathbf{H}(\mathbf{r}, t) = \mathbf{H}_0(\mathbf{r}) e^{i\omega t}, \tag{2.1.12}$$

where $\mathbf{E}_0$ and $\mathbf{H}_0$ can be considered as eigenfunctions with an eigenvalues ω^2/c^2 if they satisfy the eigenvalue equations [1, 2, 3]

$$\mathcal{L}_E \mathbf{E}_0(\mathbf{r}) \equiv \frac{1}{\epsilon(\mathbf{r})} \nabla \times \{\nabla \times \mathbf{E}_0(\mathbf{r})\} = -\frac{\omega^2}{c^2} \mathbf{E}_0(\mathbf{r}), \tag{2.1.13}$$

$$\mathcal{L}_H \mathbf{H}_0(\mathbf{r}) \equiv \nabla \times \left\{ \frac{1}{\epsilon(\mathbf{r})} \nabla \times \mathbf{H}_0(\mathbf{r}) \right\} = -\frac{\omega^2}{c^2} \mathbf{H}_0(\mathbf{r}). \tag{2.1.14}$$

It is useful to take some concepts from conventional solid state crystals and apply them to photonic crystals. Because ϵ is periodic in space, it is possible to apply Bloch's theorem such that $\mathbf{E}_0$ and $\mathbf{H}_0$ are characterized by a wave vector $\mathbf{k}$ in the first Brillouin zone and a band index n [1]. With the above, it is possible to write the eigenfunctions $\mathbf{E}_0(\mathbf{r})$ and $\mathbf{H}_0(\mathbf{r})$ as [1, 2, 3]

$$\mathbf{E}_0(\mathbf{r}) = \mathbf{E}_{\mathbf{k},n}(\mathbf{r})e^{i\mathbf{k}\cdot\mathbf{r}}, \tag{2.1.15}$$

$$\mathbf{H}_0(\mathbf{r}) = \mathbf{H}_{\mathbf{k},n}(\mathbf{r})e^{i\mathbf{k}\cdot\mathbf{r}}, \tag{2.1.16}$$

where $\mathbf{E}_{\mathbf{k},n}(\mathbf{r})$ and $\mathbf{H}_{\mathbf{k},n}(\mathbf{r})$ are periodic vector functions and satisfy

$$\mathbf{E}_{\mathbf{k},n}(\mathbf{r}+\mathbf{R}) = \mathbf{E}_{\mathbf{k},n}(\mathbf{r}), \tag{2.1.17}$$

$$\mathbf{H}_{\mathbf{k},n}(\mathbf{r}+\mathbf{R}) = \mathbf{E}_{\mathbf{k},n}(\mathbf{r}), \tag{2.1.18}$$

and $\mathbf{R}$ are the lattice vectors.

Since $\mathbf{E}_0(\mathbf{r})$, $\mathbf{H}_0(\mathbf{r})$ and the inverse of the dielectric function $1/\epsilon(\mathbf{r})$ are periodic functions, they can be expanded in Fourier series as follows

$$\mathbf{E}_0(\mathbf{r}) = \sum_{\mathbf{G}} \mathcal{E}(\mathbf{G})e^{i(\mathbf{k}+\mathbf{G})\cdot\mathbf{r}}, \tag{2.1.19}$$

$$\mathbf{H}_0(\mathbf{r}) = \sum_{\mathbf{G}} \mathcal{H}(\mathbf{G})e^{i(\mathbf{k}+\mathbf{G})\cdot\mathbf{r}}, \tag{2.1.20}$$

$$\frac{1}{\epsilon(\mathbf{r})} = \sum_{\mathbf{G}} \xi(\mathbf{G})e^{i\mathbf{G}\cdot\mathbf{r}}, \tag{2.1.21}$$

where $\{\mathbf{G}\}$ are the reciprocal vectors of the lattice, and $\mathcal{E}(\mathbf{G})$, $\mathcal{H}$, $(\mathbf{G})$ and $\xi(\mathbf{G})$ are the Fourier coefficients defined by

$$\mathcal{E}(\mathbf{G}) = \frac{1}{V}\int_V \mathbf{E}_{\mathbf{k},n}e^{-i\mathbf{G}\cdot\mathbf{r}}d\mathbf{r}, \tag{2.1.22}$$

$$\mathcal{H}(\mathbf{G}) = \frac{1}{V}\int_V \mathbf{H}_{\mathbf{k},n}e^{-i\mathbf{G}\cdot\mathbf{r}}d\mathbf{r}, \tag{2.1.23}$$

$$\xi(\mathbf{G}) = \frac{1}{V}\int_V \frac{1}{\epsilon(\omega)}e^{-i\mathbf{G}\cdot\mathbf{r}}d\mathbf{r}. \tag{2.1.24}$$

On the other hand, the reciprocal vectors are given by

$$\mathbf{G} = m_1'\boldsymbol{b}_1 + m_2'\boldsymbol{b}_2 + m_3'\boldsymbol{b}_3, \tag{2.1.25}$$

where m_i' are integers, and the reciprocal elementary vectors of lattice $\{\boldsymbol{b}_i\}$ are defined from the lattice vectors $\{\boldsymbol{a}_i\}$ by means of

$$\boldsymbol{b}_1 = 2\pi\frac{\boldsymbol{a}_2\times\boldsymbol{a}_3}{\boldsymbol{a}_1\cdot\boldsymbol{a}_2\times\boldsymbol{a}_3}, \tag{2.1.26}$$

$$\boldsymbol{b}_2 = 2\pi\frac{\boldsymbol{a}_3\times\boldsymbol{a}_1}{\boldsymbol{a}_1\cdot\boldsymbol{a}_2\times\boldsymbol{a}_3}, \tag{2.1.27}$$

$$\boldsymbol{b}_3 = 2\pi\frac{\boldsymbol{a}_1\times\boldsymbol{a}_2}{\boldsymbol{a}_1\cdot\boldsymbol{a}_2\times\boldsymbol{a}_3}, \tag{2.1.28}$$

so that

$$\boldsymbol{a}_i \cdot \boldsymbol{b}_j = \delta_{ij} 2\pi, \tag{2.1.29}$$

and

$$\mathbf{G} \cdot \mathbf{R} = m_1' \boldsymbol{b}_1 + m_2' \boldsymbol{b}_2 + m_3' \boldsymbol{b}_3 \cdot m_1 \boldsymbol{a}_1 + m_2 \boldsymbol{a}_2 + m_3 \boldsymbol{a}_3 = 2\pi N, \tag{2.1.30}$$

with N integer [1, 2].

Inserting (2.1.19) and (2.1.21) into (2.1.13), it is obtained

$$\sum_{\mathbf{G}''} \xi(\mathbf{G}'') e^{i(\mathbf{k}+\mathbf{G}'')\cdot\mathbf{r}} \nabla \times \left[\nabla \times \sum_{\mathbf{G}'} \mathcal{E}(\mathbf{G}') e^{i(\mathbf{k}+\mathbf{G}')\cdot\mathbf{r}} \right] = \frac{\omega^2}{c^2} \sum_{\mathbf{G}} \mathcal{E}(\mathbf{G}) e^{i(\mathbf{k}+\mathbf{G})\cdot\mathbf{r}}. \tag{2.1.31}$$

On the other hand,

$$\nabla \times \sum_{\mathbf{G}'} \mathcal{E}(\mathbf{G}') e^{i(\mathbf{k}+\mathbf{G}')\cdot\mathbf{r}} = \sum_{\mathbf{G}'} \nabla \times \left[\mathcal{E}(\mathbf{G}') e^{i(\mathbf{k}+\mathbf{G}')\cdot\mathbf{r}} \right], \tag{2.1.32}$$

considering that

$$\nabla \times \left[\mathcal{E}(\mathbf{G}') e^{i(\mathbf{k}+\mathbf{G}')\cdot\mathbf{r}} \right] = i\left(\mathbf{k}+\mathbf{G}'\right) \times \mathcal{E}(\mathbf{G}') e^{i(\mathbf{k}+\mathbf{G}')\cdot\mathbf{r}}, \tag{2.1.33}$$

is possible to associate the operator ∇ with the vectors $\mathbf{k}$ and $\mathbf{G}$

$$\nabla \rightarrow i\left(\mathbf{k}+\mathbf{G}\right), \tag{2.1.34}$$

so that the equation (2.1.31) becomes

$$\begin{aligned} -\sum_{\mathbf{G}''} \xi(\mathbf{G}'') e^{i(\mathbf{k}+\mathbf{G}'')\cdot\mathbf{r}} \left(\mathbf{k}+\mathbf{G}'\right) \times \left[\left(\mathbf{k}+\mathbf{G}'\right) \times \sum_{\mathbf{G}'} \mathcal{E}(\mathbf{G}') e^{i(\mathbf{k}+\mathbf{G}')\cdot\mathbf{r}} \right] = \\ = \frac{\omega^2}{c^2} \sum_{\mathbf{G}} \mathcal{E}(\mathbf{G}) e^{i(\mathbf{k}+\mathbf{G})\cdot\mathbf{r}}. \end{aligned} \tag{2.1.35}$$

The above implies

$$\mathbf{G} = \mathbf{G}' + \mathbf{G}'' \quad \Rightarrow \quad \mathbf{G}'' = \mathbf{G} - \mathbf{G}', \tag{2.1.36}$$

therefore, comparing the coefficients in the exponential function, it may be obtained

$$-\sum_{\mathbf{G}'} \xi(\mathbf{G}-\mathbf{G}')(\mathbf{k}+\mathbf{G}') \times \{(\mathbf{k}+\mathbf{G}') \times \mathcal{E}(\mathbf{G}')\} = \frac{\omega^2}{c^2} \mathcal{E}(\mathbf{G}). \tag{2.1.37}$$

In an analogue way, inserting (2.1.19) and (2.1.21) into (2.1.14) and with some algebraic manipulations, it is obtains

$$-\sum_{\mathbf{G}'} \xi(\mathbf{G}-\mathbf{G}')(\mathbf{k}+\mathbf{G}) \times \{(\mathbf{k}+\mathbf{G}') \times \mathcal{H}(\mathbf{G}')\} = \frac{\omega^2}{c^2} \mathcal{H}(\mathbf{G}) \tag{2.1.38}$$

These equations are the «Master equations» of the electric and magnetic field respectively, and by solving them, the eigenstates of the photonic crystal are obtained.

2.1.1 2D photonic crystal

The geometry of two-dimensional photonic crystals is shown in Fig. 2.2. This system is a periodic array of columns such that the dielectric function is periodically modulated in the x and y directions. For electromagnetic waves, the propagation vector $\mathbf{k}$ is parallel to the two-dimensional $x-y$ plane, so there are two polarizations, TE or H when the H_z, E_x and E_y components are non-zero, and TM or E when E_z, H_x and H_y are non-zero.

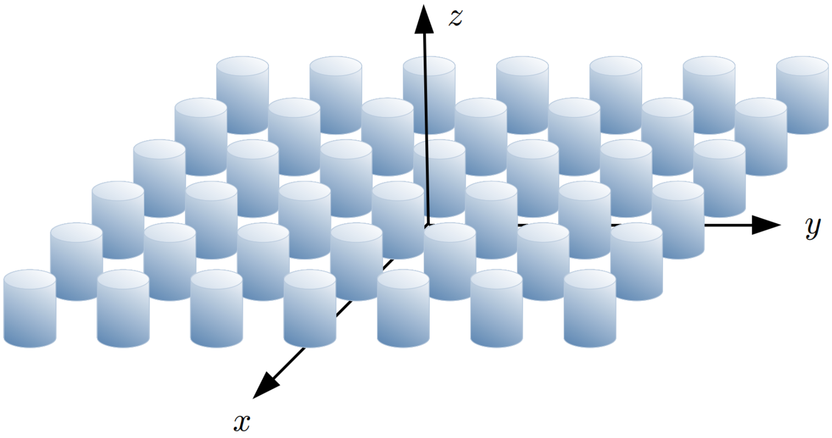

Figure 2.2: Dielectric photonic crystal in two-dimensions.

Thus, from equations (2.1.5) and (2.1.6), it is possible to obtain the following set of equations for TE polarization

$$\frac{\partial}{\partial y}H_z(\mathbf{r}_\parallel,t) = \epsilon_0\epsilon(\mathbf{r}_\parallel)\frac{\partial}{\partial t}E_x(\mathbf{r}_\parallel,t), \tag{2.1.39}$$

$$\frac{\partial}{\partial x}H_z(\mathbf{r}_\parallel,t) = -\epsilon_0\epsilon(\mathbf{r}_\parallel)\frac{\partial}{\partial t}E_y(\mathbf{r}_\parallel,t), \tag{2.1.40}$$

$$\frac{\partial}{\partial x}E_y(\mathbf{r}_\parallel,t) - \frac{\partial}{\partial y}E_x(\mathbf{r}_\parallel,t) = -\mu_0\mu(\mathbf{r}_\parallel)\frac{\partial}{\partial t}H_z(\mathbf{r}_\parallel,t), \tag{2.1.41}$$

and the following set of equations for TM polarization

$$\frac{\partial}{\partial y}E_z(\mathbf{r}_\parallel,t) = -\mu_0\mu(\mathbf{r}_\parallel)\frac{\partial}{\partial t}H_x(\mathbf{r}_\parallel,t), \tag{2.1.42}$$

$$\frac{\partial}{\partial x}E_z(\mathbf{r}_\parallel,t) = \mu_0\mu(\mathbf{r}_\parallel)\frac{\partial}{\partial t}H_y(\mathbf{r}_\parallel,t), \tag{2.1.43}$$

$$\frac{\partial}{\partial x}H_y(\mathbf{r}_\parallel,t) - \frac{\partial}{\partial y}H_x(\mathbf{r}_\parallel,t) = \epsilon_0\epsilon(\mathbf{r}_\parallel)\frac{\partial}{\partial t}E_z(\mathbf{r}_\parallel,t), \tag{2.1.44}$$

where $\mathbf{r}_\parallel$ is a vector in the plane $x-y$. With the above, the eigenvalue equations (2.1.13) and (2.1.14) are reduced to

$$\hat{\mathcal{O}}_H H_z(\mathbf{r}_\parallel) \equiv -\left\{\frac{\partial}{\partial x}\frac{1}{\epsilon(\mathbf{r}_\parallel)}\frac{\partial}{\partial x} + \frac{\partial}{\partial y}\frac{1}{\epsilon(\mathbf{r}_\parallel)}\frac{\partial}{\partial y}\right\} H_z(\mathbf{r}_\parallel) = \frac{\omega^2}{c^2}H_z(\mathbf{r}_\parallel) \tag{2.1.45}$$

for TE polarization and

$$\hat{\mathcal{O}}_E E_z(\mathbf{r}_\parallel) \equiv -\frac{1}{\epsilon(\mathbf{r}_\parallel)} \left\{ \frac{\partial^2}{\partial x^2} + \frac{\partial^2}{\partial y^2} \right\} E_z(\mathbf{r}_\parallel) = \frac{\omega^2}{c^2} E_z(\mathbf{r}_\parallel), \tag{2.1.46}$$

for TM polarization [1, 2].

Using Bloch's theorem for TM polarization, the z-component of the electric field E_z and the inverse of the dielectric function $1/\epsilon$ can be expressed as

$$E_z(\mathbf{r}_\parallel) = \sum_{\mathbf{G}_\parallel} \mathcal{E}_z(\mathbf{G}_\parallel) e^{i(\mathbf{k}_\parallel + \mathbf{G}_\parallel)\cdot \mathbf{r}_\parallel} \tag{2.1.47}$$

$$\frac{1}{\epsilon(\mathbf{r}_\parallel)} = \sum_{\mathbf{G}''_\parallel} \xi(\mathbf{G}''_\parallel) e^{i\mathbf{G}''_\parallel \cdot \mathbf{r}_\parallel} \tag{2.1.48}$$

where $\mathbf{r}_\parallel$ is a vector in the plane $x-y$ and $\mathbf{k}_\parallel$ and $\mathbf{G}_\parallel$ are vectors parallels to the $x-y$ plane in reciprocal space.

Renaming the variables $\mathbf{G}_\parallel$ and $\mathbf{r}_\parallel$ as

$$\mathbf{G}_\parallel \to \mathbf{G} \quad \text{and} \quad \mathbf{r}_\parallel \to \mathbf{r},$$

and inserting these equations into (2.1.46), it is obtained

$$-\sum_{\mathbf{G}''} \xi(\mathbf{G}'') e^{i\mathbf{G}''\cdot\mathbf{r}} \sum_{\mathbf{G}'} \left[(k_x + G'_x)^2 + \left(k_y + G'_y\right)^2 \right] \mathcal{E}_z(\mathbf{G}') e^{i(\mathbf{k}+\mathbf{G}')\cdot\mathbf{r}} = \\ = \frac{\omega^2}{c^2} \sum_{\mathbf{G}} \mathcal{E}_z(\mathbf{G}) e^{i(\mathbf{k}+\mathbf{G})\cdot\mathbf{r}}, \tag{2.1.49}$$

but

$$(k_x + G'_x)^2 + \left(k_y + G'_y\right)^2 = |\mathbf{k} + \mathbf{G}'|^2 \tag{2.1.50}$$

so,

$$-\sum_{\mathbf{G}''} \xi(\mathbf{G}'') e^{i\mathbf{G}''\cdot\mathbf{r}} \sum_{\mathbf{G}'} |\mathbf{k} + \mathbf{G}'|^2 \mathcal{E}_z(\mathbf{G}') e^{i(\mathbf{k}+\mathbf{G}')\cdot\mathbf{r}} = \frac{\omega^2}{c^2} \sum_{\mathbf{G}} \mathcal{E}_z(\mathbf{G}) e^{i(\mathbf{k}+\mathbf{G})\cdot\mathbf{r}}. \tag{2.1.51}$$

The equation (2.1.51) can be written as

$$-\sum_{\mathbf{G}''} \sum_{\mathbf{G}'} \xi(\mathbf{G}'') |\mathbf{k} + \mathbf{G}'|^2 \mathcal{E}_z(\mathbf{G}') e^{i\mathbf{G}''\cdot\mathbf{r}} e^{i\mathbf{G}'\cdot\mathbf{r}} e^{i\mathbf{k}\cdot\mathbf{r}} = \frac{\omega^2}{c^2} \sum_{\mathbf{G}} \mathcal{E}_z(\mathbf{G}) e^{i\mathbf{G}\cdot\mathbf{r}} e^{i\mathbf{k}\cdot\mathbf{r}}. \tag{2.1.52}$$

By comparing terms, the arguments of exponential functions must satisfy

$$\mathbf{G}'' + \mathbf{G}' = \mathbf{G}, \tag{2.1.53}$$

so that

$$\mathbf{G}'' = \mathbf{G} - \mathbf{G}', \tag{2.1.54}$$

and the equation (2.1.52) can be written as

$$-\sum_{\mathbf{G}-\mathbf{G}'}\sum_{\mathbf{G}'}\xi(\mathbf{G}-\mathbf{G}')|\mathbf{k}+\mathbf{G}'|^2\mathcal{E}_z(\mathbf{G}')e^{i\mathbf{G}\cdot\mathbf{r}}=\frac{\omega^2}{c^2}\sum_{\mathbf{G}}\mathcal{E}_z(\mathbf{G})e^{i\mathbf{G}\cdot\mathbf{r}}. \tag{2.1.55}$$

To make the equation (2.1.55) more transparent, summing over $\mathbf{G}$ from $\mathbf{G}_{-l}$ to $\mathbf{G}_l$

$$\begin{aligned}-\sum_{\mathbf{G}'}|\mathbf{k}+\mathbf{G}'|^2\mathcal{E}_z(\mathbf{G}')\left[\xi\left(\mathbf{G}_{-l}-\mathbf{G}'\right)e^{i\mathbf{G}_{-l}\cdot\mathbf{r}}+\ldots+\xi\left(\mathbf{G}_{l}-\mathbf{G}'\right)e^{i\mathbf{G}_{l}\cdot\mathbf{r}}\right]&=\\ =\frac{\omega^2}{c^2}\left[\mathcal{E}_z(\mathbf{G}_{-l})e^{i\mathbf{G}_{-l}\cdot\mathbf{r}}+\ldots+\mathcal{E}_z(\mathbf{G}_{l})e^{i\mathbf{G}_{l}\cdot\mathbf{r}}\right]&. \end{aligned}\tag{2.1.56}$$

Comparing terms it is obtains

$$-\sum_{\mathbf{G}'}|\mathbf{k}+\mathbf{G}'|^2\mathcal{E}_z(\mathbf{G}')\xi\left(\mathbf{G}_m-\mathbf{G}'\right)=\frac{\omega^2}{c^2}\mathcal{E}_z(\mathbf{G}_m),\quad\forall\, m\in[-l,\ldots,l]\,. \tag{2.1.57}$$

This way, the equation (2.1.56) becomes

$$\sum_{\mathbf{G}'}\xi(\mathbf{G}-\mathbf{G}')|\mathbf{k}+\mathbf{G}'|^2\mathcal{E}_z(\mathbf{G}')=\frac{\omega^2}{c^2}\mathcal{E}_z(\mathbf{G}) \tag{2.1.58}$$

This is the Master equation for TM polarization. Similarly, it is possible to obtain a master equation for TE polarization, given by

$$\sum_{\mathbf{G}'_{\|}}\xi(\mathbf{G}_{\|}-\mathbf{G}'_{\|})\left(\mathbf{k}_{\|}+\mathbf{G}_{\|}\right)\cdot\left(\mathbf{k}_{\|}+\mathbf{G}'_{\|}\right)\mathcal{H}_z(\mathbf{G}')=\frac{\omega^2}{c^2}\mathcal{H}_z(\mathbf{G}) \tag{2.1.59}$$

Since SPPs are electromagnetic waves with TM polarization, the analysis will focus only on equation (2.1.58). This master equation can be written as

$$\sum_{l,m}\xi_{q-l,s-m}|\mathbf{k}+\mathbf{G}_{l,m}|^2\mathcal{E}_{z,l,m}=\frac{\omega^2}{c^2}\mathcal{E}_{z,q,s} \tag{2.1.60}$$

where $l,m,q,s=-n\ldots n$. Thus, for n plane waves, a system of $(2n+1)^2$ algebraic equations is obtained:

$$\begin{array}{ccccccc}\xi_{0,0}K^2_{-n,-n}\mathcal{E}_{-n,-n}+ & \xi_{0,-1}K^2_{-n,-n+1}\mathcal{E}_{-n,-n+1} & +\ldots+ & \xi_{-2n,-2n}K^2_{n,n}\mathcal{E}_{n,n} & = & \frac{\omega^2}{c^2}\mathcal{E}_{-n,-n}\\ \xi_{0,1}K^2_{-n,-n}\mathcal{E}_{-n,-n}+ & \xi_{0,0}K^2_{-n,-n+1}\mathcal{E}_{-n,-n+1} & +\ldots+ & \xi_{-2n,-2n-1}K^2_{n,n}\mathcal{E}_{n,n} & = & \frac{\omega^2}{c^2}\mathcal{E}_{-n,-n+1}\\ \vdots & \vdots & \ddots & \vdots & \vdots & \\ \xi_{2n,2n}K^2_{-n,-n}\mathcal{E}_{-n,-n}+ & \xi_{2n,2n-1}K^2_{-n,-n+1}\mathcal{E}_{-n,-n+1} & +\ldots+ & \xi_{0,0}K^2_{n,n}\mathcal{E}_{n,n} & = & \frac{\omega^2}{c^2}\mathcal{E}_{n,n}\end{array} \tag{2.1.61}$$

This equations system can be written as a matrix product as

$$\begin{pmatrix} \xi_{0,0} & \xi_{0,-1} & \cdots & \xi_{-2n,-2n} \\ \xi_{0,1} & \xi_{0,0} & \cdots & \xi_{-2n,-2n+1} \\ \vdots & \vdots & \ddots & \vdots \\ \xi_{2n,2n} & \xi_{2n,2n-1} & \cdots & \xi_{0,0} \end{pmatrix} \begin{pmatrix} K^2_{-n,-n} & 0 & \cdots & 0 \\ 0 & K^2_{-n,-n+1} & \cdots & 0 \\ \vdots & \vdots & \ddots & \vdots \\ 0 & 0 & \cdots & K^2_{n,n} \end{pmatrix} \begin{pmatrix} \mathcal{E}_{-n,-n} \\ \mathcal{E}_{-n,-n+1} \\ \vdots \\ \mathcal{E}_{n,n} \end{pmatrix} = \tag{2.1.62}$$

$$= \frac{\omega^2}{c^2} \begin{pmatrix} \mathcal{E}_{-n,-n} \\ \mathcal{E}_{-n,-n+1} \\ \vdots \\ \mathcal{E}_{n,n} \end{pmatrix}$$

where $K^2_{l,m} = |\mathbf{k} + \mathbf{G}_{l,m}|^2$. It is possible to reformulate this equation as an eigenvalue problem:

$$\hat{\mathbf{\Xi}}\hat{\mathbf{K}}\mathcal{E} = \hat{\mathbf{M}}\mathcal{E} = \frac{\omega^2}{c^2}\mathcal{E} \tag{2.1.63}$$

where $\hat{\mathbf{\Xi}}$ is a matrix constructed by the quantities $\xi_{q-l,s-m}$, $\hat{\mathbf{K}}$ is a diagonal matrix constructed by the quantities $K^2_{l,m}$, $\hat{\mathbf{M}}$ is the matrix representation of the operator $\hat{\mathcal{O}}_E$, and ω^2/c^2 are the eigenvalues. This problem can be solved by finding the eigenvalues of the matrix $\hat{\mathbf{M}}$ for a particular problem.

2.2 Two-dimensional hybrid photonic-plasmonic crystals

SPPs are electromagnetic excitations propagating at an interface formed by a dielectric medium and a metallic medium. When these media have a semi-infinite width, the dispersion relation is [4]

$$\beta = \frac{\omega}{c}\sqrt{\frac{\epsilon_d \epsilon_m}{\epsilon_d + \epsilon_m}}, \tag{2.2.1}$$

where β is the SPP propagation constant, ϵ_d is the dielectric function of the dielectric medium and $\epsilon_m = \epsilon_m(\omega)$ is the (frequency-dependent) dielectric function of the metallic medium. From this equation, the effective refractive index is defined as [4]

$$n_{eff} = \sqrt{\frac{\epsilon_d \epsilon_m}{\epsilon_d + \epsilon_m}}, \tag{2.2.2}$$

so the effective dielectric function for SPPs is

$$\epsilon_{eff} = \frac{\epsilon_d \epsilon_m}{\epsilon_d + \epsilon_m}, \tag{2.2.3}$$

and the inverse of the effective dielectric function is

$$\frac{1}{\epsilon_{eff}} = \frac{\epsilon_d + \epsilon_m}{\epsilon_d \epsilon_m}. \tag{2.2.4}$$

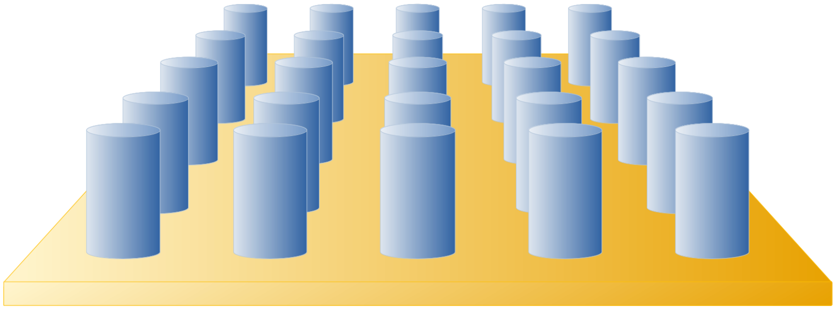

Figure 2.3: Dielectric photonic crystal over a metal thin film.

It is important to consider that the quantity $\epsilon_{eff}(\omega)$ is a frequency-dependent function since ϵ_m is a frequency-dependent function.

The system under analysis is a dielectric photonic crystal supported on a metallic thin film with permittivity ϵ_m, as shown in Fig. 2.3. Furthermore, the photonic crystal is formed by a dielectric matrix with permittivity ϵ_a and a periodic array of columns with permittivity ϵ_b embedded in the matrix mentioned above. Both dielectric functions are considered to be frequency independent. This way, there are two interfaces, one formed by the dielectric a (matrix with permittivity ϵ_a) and the metallic thin film, and the other formed by the dielectric b (dielectric columns with permittivity ϵ_b) and the metallic thin film itself. With the above, the system has two effective refractive indexes, so the inverse dielectric functions are given by

$$\frac{1}{\epsilon_1(\omega)} = \frac{\epsilon_a + \epsilon_m}{\epsilon_a \epsilon_m} \quad \text{and} \quad \frac{1}{\epsilon_2(\omega)} = \frac{\epsilon_b + \epsilon_m}{\epsilon_b \epsilon_m}. \tag{2.2.5}$$

In the description of the physical system, a «base» is the repeating element, that is, the interface formed by the dielectric b and the metallic thin film. Figure 2.4 shows three rectangular unit cells with three different bases. For the interface represented by the white zone in the unit

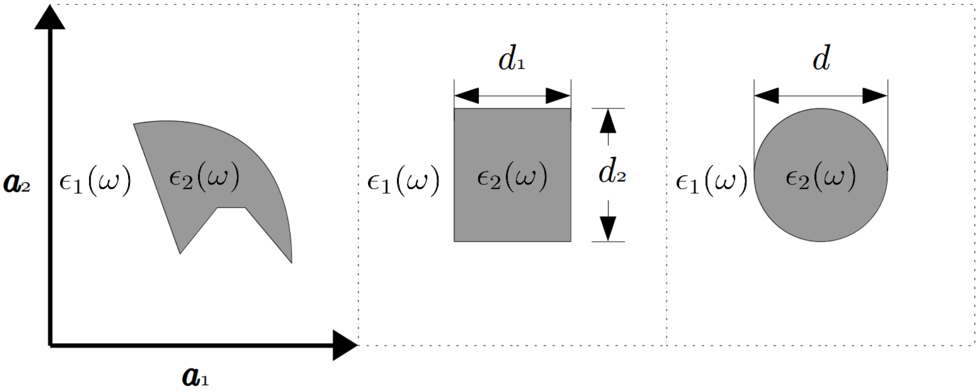

Figure 2.4: Rectangular lattice with an arbitrary shape base (left), rectangular base (center) and circular base (right).

cell, the effective dielectric function is described by $\epsilon_1 = \epsilon_a\epsilon_m/(\epsilon_a+\epsilon_m)$, while for the interface represented by the gray zone, the effective dielectric function is described by $\epsilon_2 = \epsilon_b\epsilon_m/(\epsilon_b+\epsilon_m)$.

The inverse of the dielectric function in a unit cell, as shown in Fig. 2.4, is described by $1/\epsilon_1(\omega)$ in the white zone and $1/\epsilon_2(\omega)$ in the gray zone. In general, the inverse of the effective dielectric function over the whole unit cell is

$$\frac{1}{\epsilon_{eff}(\omega)} = \frac{1}{\epsilon_1(\omega)} + \left(\frac{1}{\epsilon_2(\omega)} - \frac{1}{\epsilon_1(\omega)}\right) F(\mathbf{r}) = \frac{1}{\epsilon_1(\omega)} + \Delta\xi F(\mathbf{r}), \tag{2.2.6}$$

where $F(\mathbf{r}) = 1$, if $\mathbf{r}$ is within the gray, zone and $F(\mathbf{r}) = 0$ otherwise.

The inverse of the effective dielectric function can be expanded into a Fourier series as

$$\frac{1}{\epsilon(\omega)} = \sum_{\mathbf{G}'} \xi(\mathbf{G}')e^{i\mathbf{G}'\cdot\mathbf{r}}, \tag{2.2.7}$$

where $\mathbf{G}'$ are the reciprocal vectors and $\xi(\mathbf{G}')$ are the Fourier coefficients given by

$$\xi(\mathbf{G}') = \frac{1}{A_0}\int_{A_0} \frac{1}{\epsilon(\omega)} e^{-i\mathbf{G}'\cdot\mathbf{r}} d\mathbf{r}, \tag{2.2.8}$$

where A_0 is the area of the unit cell. Given the above, considering that ϵ_a and ϵ_b are frequency-independent quantities, the Fourier coefficients, for a two-dimensional unit cell, are as follows.

$$\begin{aligned}\xi(\mathbf{G}') &= \frac{1}{A_0}\int_{A_0} \left[\frac{1}{\epsilon_1(\omega)} + \left(\frac{1}{\epsilon_2(\omega)} - \frac{1}{\epsilon_1(\omega)}\right) F(\mathbf{r}) e^{-i\mathbf{G}'\cdot\mathbf{r}}\right] d\mathbf{r} \\ &= \frac{1}{A_0}\int_{A_0} \frac{1}{\epsilon_1(\omega)} d\mathbf{r} + \int_{A_0} \left(\frac{1}{\epsilon_2(\omega)} - \frac{1}{\epsilon_1(\omega)}\right) F(\mathbf{r}) e^{-i\mathbf{G}'\cdot\mathbf{r}} d\mathbf{r} \\ &= \frac{1}{\epsilon_1(\omega)}\delta^2(\mathbf{G}') + \frac{1}{A_0}\left(\frac{1}{\epsilon_2(\omega)} - \frac{1}{\epsilon_1(\omega)}\right)\mathcal{F}(\mathbf{G}'),\end{aligned} \tag{2.2.9}$$

where $\delta^2(\mathbf{G}')$ is the two-dimensional Dirac delta function and $\mathcal{F}(\mathbf{G}')$ is the Fourier transform of $F(\mathbf{r})$.

The term in parentheses is reduced to

$$\begin{aligned}\Delta\xi &= \frac{1}{\epsilon_2(\omega)} - \frac{1}{\epsilon_1(\omega)} = \frac{\epsilon_b+\epsilon_m}{\epsilon_a\epsilon_m} - \frac{\epsilon_a+\epsilon_m}{\epsilon_b\epsilon_m} = \frac{\epsilon_a\epsilon_b+\epsilon_a\epsilon_m}{\epsilon_a\epsilon_b\epsilon_m} - \frac{\epsilon_a\epsilon_b+\epsilon_b\epsilon_m}{\epsilon_a\epsilon_b\epsilon_m} \\ &= \frac{\epsilon_a\epsilon_b+\epsilon_a\epsilon_m-\epsilon_a\epsilon_b-\epsilon_b\epsilon_m}{\epsilon_a\epsilon_b\epsilon_m} = \frac{\epsilon_a\epsilon_m-\epsilon_b\epsilon_m}{\epsilon_a\epsilon_b\epsilon_m} = \frac{\epsilon_a-\epsilon_b}{\epsilon_a\epsilon_b}.\end{aligned} \tag{2.2.10}$$

It is important to note that this quantity is not frequency-dependent if both ϵ_a and ϵ_b are frequency-independent. Thus, equation (2.2.9) can be expressed as

$$\xi(\mathbf{G}') = \frac{1}{\epsilon_1(\omega)}\delta^2(\mathbf{G}') + \frac{1}{V}\Delta\xi\mathcal{F}(\mathbf{G}'), \tag{2.2.11}$$

and the first member on the right-hand side of the equation is the only one frequency-dependent. In terms of the labels l, m, q and s, as in equation (2.1.60), it is possible to express this quantity as

$$\xi_{q-l,s-m} = \begin{cases} \frac{1}{\epsilon_1(\omega)} + \frac{1}{V}\Delta\xi\mathcal{F}(0,0) & \text{, if } q-l=0, s-m=0 \\ \\ \frac{1}{V}\Delta\xi\mathcal{F}(q-l,s-m) & \text{, if } q-l\neq 0, s-m\neq 0. \end{cases} \tag{2.2.12}$$

Thus, the quantity $\xi_{q-l,s-m}$ is frequency-dependent when $q-l=0$ and $s-m=0$, that is, only the $\xi_{0,0}$ term frequency-dependent. This will be useful in solving the eigenvalue problem.

The matrix $\hat{\boldsymbol{\Xi}}'$ in the equation (2.1.62) given by

$$\begin{aligned} \hat{\boldsymbol{\Xi}}' &= \begin{pmatrix} \xi_{0,0} & \xi_{0,-1} & \cdots & \xi_{-2n,-2n} \\ \xi_{0,1} & \xi_{0,0} & \cdots & \xi_{-2n,-2n+1} \\ \vdots & \vdots & \ddots & \vdots \\ \xi_{2n,2n} & \xi_{2n,2n-1} & \cdots & \xi_{0,0} \end{pmatrix} \\ &= \begin{pmatrix} \frac{1}{\epsilon_1(\omega)} + \frac{1}{V}\Delta\xi\mathcal{F}(0,0) & \frac{1}{V}\Delta\xi\mathcal{F}(0,-1) & \cdots & \frac{1}{V}\Delta\xi\mathcal{F}(-2n,-2n) \\ \frac{1}{V}\Delta\xi\mathcal{F}(0,1) & \frac{1}{\epsilon_1(\omega)} + \frac{1}{V}\Delta\xi\mathcal{F}(0,0) & \cdots & \frac{1}{V}\Delta\xi\mathcal{F}(-2n,-2n+1) \\ \vdots & \vdots & \ddots & \vdots \\ \frac{1}{V}\Delta\xi\mathcal{F}(2n,2n) & \frac{1}{V}\Delta\xi\mathcal{F}(2n,2n-1) & \cdots & \frac{1}{\epsilon_1(\omega)} + \frac{1}{V}\Delta\xi\mathcal{F}(0,0) \end{pmatrix}, \end{aligned} \tag{2.2.13}$$

can be separated into the sum of two matrices, one frequency-dependent and the other frequency-independent, thus expressed as

$$\hat{\boldsymbol{\Xi}}' = \hat{\boldsymbol{\Xi}}_{\mathbf{0}}(\omega) + \hat{\boldsymbol{\Xi}} \tag{2.2.14}$$

with

$$\hat{\boldsymbol{\Xi}}_{\mathbf{0}}(\omega) = \frac{1}{\epsilon_1(\omega)}\hat{\mathbf{1}} = \frac{1}{\epsilon_1(\omega)} \begin{pmatrix} 1 & 0 & \cdots & 0 \\ 0 & 1 & \cdots & 0 \\ \vdots & \vdots & \ddots & \vdots \\ 0 & 0 & \cdots & 1 \end{pmatrix} \tag{2.2.15}$$

where $\hat{\mathbf{1}}$ is a unitary matrix of size $(2n+1)^2$ and

$$\hat{\boldsymbol{\Xi}} = \begin{pmatrix} \frac{1}{V}\Delta\xi\mathcal{F}(0,0) & \frac{1}{V}\Delta\xi\mathcal{F}(0,-1) & \cdots & \frac{1}{V}\Delta\xi\mathcal{F}(-2n,-2n) \\ \frac{1}{V}\Delta\xi\mathcal{F}(0,1) & \frac{1}{V}\Delta\xi\mathcal{F}(0,0) & \cdots & \frac{1}{V}\Delta\xi\mathcal{F}(-2n,-2n+1) \\ \vdots & \vdots & \ddots & \vdots \\ \frac{1}{V}\Delta\xi\mathcal{F}(2n,2n) & \frac{1}{V}\Delta\xi\mathcal{F}(2n,2n-1) & \cdots & \frac{1}{V}\Delta\xi\mathcal{F}(0,0) \end{pmatrix}. \tag{2.2.16}$$

Then, the eigenvalue equation (2.1.63) can be written as

$$\left(\frac{1}{\epsilon_1(\omega)}\hat{\mathbf{1}} + \hat{\boldsymbol{\Xi}}\right)\hat{\mathbf{K}}\mathcal{E} = \frac{\omega^2}{c^2}\mathcal{E} \tag{2.2.17}$$

In particular, Au or Ag thin films are considered, since the Au-dielectric or Ag-dielectric interfaces support the propagation of SPP. The inverse of the dielectric function described by equation (2.2.4) for dielectric-Au or dielectric-Ag interfaces can be approximated, over a suitable frequency range, by a function expressed as follows:

$$\frac{1}{\epsilon_{eff}(\omega)} \approx \frac{1}{\epsilon_d} + \gamma_1 \left(\frac{\omega}{c} - b\right)^{-2} + \gamma_2 \left(\frac{\omega}{c} - b\right)^{-1} + \gamma_3 \left(\frac{\omega}{c} - b\right), \tag{2.2.18}$$

where the parameters γ_i and b are determined as a function of the dielectric constants ϵ_d and ϵ_m. With the change of variable $\alpha = \omega/c - b$, the inverses of the dielectric functions $1/\epsilon_1(\omega)$ and $1/\epsilon_2(\omega)$ are.

$$\frac{1}{\epsilon_1} = \frac{1}{\epsilon_a} + \gamma_1\alpha^{-2} + \gamma_2\alpha^{-1} + \gamma_3\alpha, \tag{2.2.19}$$

$$\frac{1}{\epsilon_2} = \frac{1}{\epsilon_b} + \gamma_1\alpha^{-2} + \gamma_2\alpha^{-1} + \gamma_3\alpha. \tag{2.2.20}$$

As an example, Fig. 2.5a shows the inverse of the dielectric function data for an air-Au interface (black circles), and a PMMA-Au interface (black squares), in the range of wavelength range 548.6-1937 nm. Figure 2.5b shows the inverse of the dielectric function data for an air-Ag interface (black circles) and a PMMA-Ag interface (black squares), in the wavelength range of 331.5-1937 nm. In all cases, the inverse of the dielectric function was calculated using Johnson & Christy permittivity data for Au and Ag [5]. In addition, the solid and dashed lines are the data fitted to equation (2.2.18).

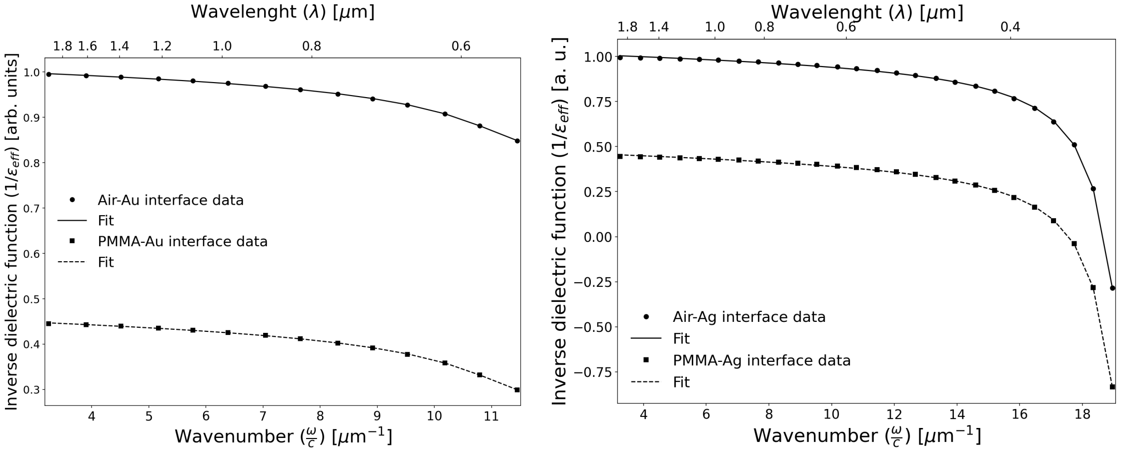

(a) Air-Au and PMMA-Au interfaces.

(b) Air-Ag and PMMA-Ag interfaces.

Figure 2.5: Inverse dielectric function and data fitting for two different interfaces.

Taking into account the equations (2.2.19) and $\alpha = \omega/c - b$, the eigenvalue equation (2.2.17) becomes

$$\left(\gamma_1\alpha^{-2}\hat{\mathbf{1}} + \gamma_2\alpha^{-1}\hat{\mathbf{1}} + \frac{1}{\epsilon_a}\hat{\mathbf{1}} + \hat{\mathbf{\Xi}} + \gamma_3\alpha\hat{\mathbf{1}}\right)\hat{\mathbf{K}}\mathcal{E} = \left(b^2 + 2b\alpha + \alpha^2\right)\mathcal{E}. \tag{2.2.21}$$

Ordering terms in the last equation

$$\left[\alpha^{-2}\gamma_1\hat{\mathbf{K}}+\alpha^{-1}\gamma_2\hat{\mathbf{K}}+\left(\frac{1}{\epsilon_a}\hat{\mathbf{K}}+\hat{\boldsymbol{\Xi}}\hat{\mathbf{K}}-b^2\hat{\mathbf{1}}\right)+\alpha\left(\gamma_3\hat{\mathbf{K}}-2b\hat{\mathbf{1}}\right)\right]\mathcal{E}=\alpha^2\mathcal{E} \tag{2.2.22}$$

Let $\hat{\mathbf{A}}=\gamma_1\hat{\mathbf{K}}$, $\hat{\mathbf{B}}=\gamma_2\hat{\mathbf{K}}$, $\hat{\mathbf{C}}=(\frac{1}{\epsilon_a}\hat{\mathbf{1}}+\hat{\boldsymbol{\Xi}})\hat{\mathbf{K}}-b^2\hat{\mathbf{1}}$ and $\hat{\mathbf{D}}=\gamma_3\hat{\mathbf{K}}-2b\hat{\mathbf{1}}$, such that the equation (2.2.22) is rewritten as

$$\left(\alpha^{-2}\hat{\mathbf{A}}+\alpha^{-1}\hat{\mathbf{B}}+\hat{\mathbf{C}}+\alpha\hat{\mathbf{D}}\right)\mathcal{E}=\alpha^2\mathcal{E} \tag{2.2.23}$$

Now, the problem has become a nonlinear eigenvalue equation, however, it can be solved with an extended matrix $\hat{\mathbf{M}}_{ext}$ to treat it as a linear eigenvalue problem [6, 7]. This extended matrix acts on an extended vector $\mathcal{E}_{ext}$ as follows

$$\hat{\mathbf{M}}_{ext}\mathcal{E}_{ext}=\begin{pmatrix}\hat{\mathbf{0}}&\hat{\mathbf{1}}&\hat{\mathbf{0}}&\hat{\mathbf{0}}\\\hat{\mathbf{0}}&\hat{\mathbf{0}}&\hat{\mathbf{1}}&\hat{\mathbf{0}}\\\hat{\mathbf{0}}&\hat{\mathbf{0}}&\hat{\mathbf{0}}&\hat{\mathbf{1}}\\\hat{\mathbf{A}}&\hat{\mathbf{B}}&\hat{\mathbf{C}}&\hat{\mathbf{D}}\end{pmatrix}\begin{pmatrix}\alpha^{-2}\mathcal{E}\\\alpha^{-1}\mathcal{E}\\\mathcal{E}\\\alpha\mathcal{E}\end{pmatrix}=\begin{pmatrix}\alpha^{-1}\mathcal{E}\\\mathcal{E}\\\alpha\mathcal{E}\\\left(\alpha^{-2}\hat{\mathbf{A}}+\alpha^{-1}\hat{\mathbf{B}}+\hat{\mathbf{C}}+\alpha\hat{\mathbf{D}}\right)\mathcal{E}\end{pmatrix}=\alpha\begin{pmatrix}\alpha^{-2}\mathcal{E}\\\alpha^{-1}\mathcal{E}\\\mathcal{E}\\\alpha\mathcal{E}\end{pmatrix}, \tag{2.2.24}$$

where $\hat{\mathbf{0}}$ is a square matrix of zeros of size $(2n+1)^2$. The eigenfrequencies for the original problem can be obtained by finding the eigenvalues of the matrix $\hat{\mathbf{M}}_{ext}$.

2.2.1 Fourier coefficients for the inverse dielectric function

In this subsection, the Fourier coefficients ξ of the inverse of the dielectric function will be calculated. Two different bases will be considered, a rectangular one, which physically corresponds to a dielectric column with a rectangular cross-section, and an elliptical one, which corresponds to a dielectric column with an elliptical cross-section.

Rectangular base

The dielectric function is described by

$$\epsilon(\mathbf{r},\omega)=\epsilon_1(\mathbf{r},\omega)+\left[\epsilon_2(\mathbf{r},\omega)-\epsilon_1(\mathbf{r},\omega)\right]\operatorname{rect}\left(\frac{x}{d_x}\right)\operatorname{rect}\left(\frac{y}{d_y}\right) \tag{2.2.25}$$

where the rectangule function is defined as [8]

$$\operatorname{rect}\left(\frac{x}{d_x}\right)\operatorname{rect}\left(\frac{y}{d_y}\right)=\begin{cases}1 & \text{if } |x|<d_x/2,\ |y|<d_y\\ \frac{1}{2} & \text{if } |x|=d_x,\ |y|=d_y/2\\ 0 & \text{if } |x|>d_x,\ |y|>d_y/2\end{cases} \tag{2.2.26}$$

where d_x is the side of the rectangle in the x-direction and d_y is the side of the rectangle in the y-direction.

For a homogeneous medium $\epsilon_i(\mathbf{r},\omega) = \epsilon_i(\omega)$, with $i = 1, 2$, the inverse of the dielectric function can be written as

$$\frac{1}{\epsilon(\mathbf{r},\omega)} = \frac{1}{\epsilon_1(\omega)} + \left[\frac{1}{\epsilon_2(\omega)} - \frac{1}{\epsilon_1(\omega)}\right] \mathrm{rect}\left(\frac{x}{d_x}\right) \mathrm{rect}\left(\frac{y}{d_y}\right) \tag{2.2.27}$$

So, the function $\xi(\mathbf{G}_\parallel)$ is given by

$$\xi(\mathbf{G}_\parallel) = \frac{1}{\epsilon_1(\omega)}\delta^2(\mathbf{G}_\parallel) + \frac{1}{A_0}\left[\frac{1}{\epsilon_2(\omega)} - \frac{1}{\epsilon_1(\omega)}\right] \int_{A_0} \mathrm{rect}\left(\frac{x}{d_x}\right) \mathrm{rect}\left(\frac{y}{d_y}\right) e^{-i\mathbf{G}_\parallel\cdot\mathbf{r}_\parallel} dxdy \tag{2.2.28}$$

with A_0 the area of the unit cell.

For $\mathbf{G}_\parallel = \mathbf{0}$, the quantity $\xi(\mathbf{0})$ is

$$\begin{aligned}
\xi(\mathbf{0}) &= \frac{1}{\epsilon_1(\omega)} + \frac{1}{A_0}\left[\frac{1}{\epsilon_2(\omega)} - \frac{1}{\epsilon_1(\omega)}\right] \int_{-d_y/2}^{d_y/2}\int_{-d_x/2}^{d_x/2} dxdy & (2.2.29)\\
&= \frac{1}{\epsilon_1(\omega)} + \frac{1}{A_0}\left[\frac{1}{\epsilon_2(\omega)} - \frac{1}{\epsilon_2(\omega)}\right] d_x d_y \\
&= \frac{1}{\epsilon_1(\omega)} + \frac{A_b}{A_0}\left[\frac{1}{\epsilon_2(\omega)} - \frac{1}{\epsilon_1(\omega)}\right] = \frac{1}{\epsilon_1(\omega)} + f\Delta\xi & (2.2.30)
\end{aligned}$$

where $A_b = d_x d_y$ is the area of the base, $f = A_b/A_0$ is the filling fraction and $\Delta\xi$ is given by the equation (2.2.10). In contrast, for $\mathbf{G}_\parallel \neq \mathbf{0}$

$$\begin{aligned}
\xi(\mathbf{G}_\parallel) &= \frac{1}{A_0}\left[\frac{1}{\epsilon_2(\omega)} - \frac{1}{\epsilon_2(\omega)}\right] \int_{A_0} \mathrm{rect}\left(\frac{x}{d_x}\right) \mathrm{rect}\left(\frac{y}{d_y}\right) e^{-i\mathbf{G}_\parallel\cdot\mathbf{r}_\parallel} dxdy \\
&= \frac{1}{A_0}\left[\frac{1}{\epsilon_2(\omega)} - \frac{1}{\epsilon_2(\omega)}\right] \int_{-d_y/2}^{d_y/2}\int_{-d_x/2}^{d_x/2} e^{-i\mathbf{G}_\parallel\cdot\mathbf{r}_\parallel} dxdy. & (2.2.31)
\end{aligned}$$

Taking into account that

$$\mathbf{G}_\parallel \cdot \mathbf{r}_\parallel = G_x x + G_y y, \tag{2.2.32}$$

the integral in equation (2.2.31) is

$$\begin{aligned}
\int_{-d_y/2}^{d_y/2}\int_{-d_x/2}^{d_x/2} e^{-i\mathbf{G}_\parallel\cdot\mathbf{r}_\parallel} dxdy &= \int_{-d_y/2}^{d_y/2}\int_{-d_x/2}^{d_x/2} e^{-iG_x x} e^{-iG_y y} dxdy \\
&= \int_{-d_x/2}^{d_x/2} e^{-iG_x x} \int_{-d_y/2}^{d_y/2} e^{-iG_y y} dxdy \\
&= \left(\frac{e^{-iG_x d_x/2} - e^{iG_x d_x/2}}{iG_x}\right)\left(\frac{e^{-iG_y d_y/2} - e^{iG_y d_x/2}}{iG_y}\right). & (2.2.33)
\end{aligned}$$

Recalling that

$$\sin\theta = \frac{e^{i\theta} - e^{-i\theta}}{2i}, \tag{2.2.34}$$

hence

$$\begin{aligned}
\int_{-d_y/2}^{d_y/2}\int_{-d_x/2}^{d_x/2} e^{-i\mathbf{G}_\parallel\cdot\mathbf{r}_\parallel} dxdy &= \frac{2}{G_x}\left(\frac{e^{iG_xd_x/2}-e^{-iG_xd_x/2}}{2i}\right)\frac{2}{G_y}\left(\frac{e^{iG_yd_y/2}-e^{-iG_yd_x/2}}{2i}\right)\\
&= \frac{2}{G_x}\sin\left(G_xd_x/2\right)\frac{2}{G_y}\sin\left(G_yd_y/2\right)\\
&= d_x\frac{1}{G_xd_x/2}\sin\left(G_xd_x/2\right)d_y\frac{1}{G_yd_y/2}\sin\left(G_yd_y/2\right). \qquad (2.2.35)
\end{aligned}$$

Defining the function sinc(x) as [8]

$$\text{sinc}(x) = \frac{\sin(x)}{x} \qquad (2.2.36)$$

$$\int_{-d_y/2}^{d_y/2}\int_{-d_x/2}^{d_x/2} e^{-i\mathbf{G}_\parallel\cdot\mathbf{r}_\parallel} dxdy = d_x\text{sinc}\left(\frac{G_xd_x}{2}\right)d_y\text{sinc}\left(\frac{G_yd_y}{a}\right). \qquad (2.2.37)$$

Thus, the equation (2.2.31) is

$$\begin{aligned}
\xi(\mathbf{G}_\parallel) &= \frac{1}{A_0}\left[\frac{1}{\epsilon_2(\omega)}-\frac{1}{\epsilon_2(\omega)}\right]d_x\text{sinc}\left(\frac{G_xd_x}{2}\right)d_y\text{sinc}\left(\frac{G_yd_y}{2}\right)\\
&= \frac{A_b}{A_0}\Delta\xi\text{sinc}\left(\frac{G_xd_x}{2}\right)\text{sinc}\left(\frac{G_yd_y}{2}\right) \qquad (2.2.38)
\end{aligned}$$

In general, the quantity ξ is given by

$$\xi(\mathbf{G}_\parallel) = \begin{cases} \frac{1}{\epsilon_1(\omega)} + f\Delta\xi & \text{if } \mathbf{G}_\parallel = \mathbf{0} \\ \\ f\Delta\xi\text{sinc}\left(\frac{G_xd}{2}\right)\text{sinc}\left(\frac{G_yd}{2}\right) & \text{if } \mathbf{G}_\parallel \neq \mathbf{0} \end{cases} \qquad (2.2.39)$$

considering $f = d_xd_y/A_0 = A_b/A_0$.

Elliptical base

To calculate the Fourier coefficients of an elliptical base, first the Fourier coefficients for a circular base will be calculated. Subsequently, through the similarity theorem, the Fourier coefficients for an elliptic basis will be generalized.

The dielectric function is described as

$$\epsilon\left(\mathbf{r},\omega\right) = \epsilon_1\left(\mathbf{r},\omega\right) + \left[\epsilon_2\left(\mathbf{r},\omega\right) - \epsilon_1\left(\mathbf{r},\omega\right)\right]\text{circ}\left(r\right), \qquad (2.2.40)$$

where the circle function circ (r) is defined by [8]

$$\text{circ}\left(r\right) = \begin{cases} 1 & \text{if } r < 1 \\ \frac{1}{2} & \text{if } r = 1, \\ 0 & \text{if } r > 1 \end{cases} \qquad (2.2.41)$$

where $r = \sqrt{x^2 + y^2}$.

As in the previous case, for homogeneous medium, $\epsilon_i(\mathbf{r}, \omega) = \epsilon_i(\omega)$, with $i = 1, 2$, and the inverse of the dielectric function can be written as

$$\frac{1}{\epsilon(\mathbf{r}, \omega)} = \frac{1}{\epsilon_1(\omega)} + \left[\frac{1}{\epsilon_2(\omega)} - \frac{1}{\epsilon_1(\omega)}\right] \mathrm{circ}(r). \tag{2.2.42}$$

Thus, the function $\xi(\mathbf{G}_\parallel)$ is given by

$$\xi(\mathbf{G}_\parallel) = \frac{1}{\epsilon_1(\omega)} \delta^2(\mathbf{G}_\parallel) + \frac{1}{A_0} \left[\frac{1}{\epsilon_2(\omega)} - \frac{1}{\epsilon_2(\omega)}\right] \int_{A_0} \mathrm{circ}(r) e^{-i\mathbf{G}_\parallel \cdot \mathbf{r}_\parallel} dA \tag{2.2.43}$$

with $A_0 = a^2$ the area of the unit cell.

The analysis is separated into two cases, for $\mathbf{G}_\parallel = \mathbf{0}$ and $\mathbf{G}_\parallel \neq \mathbf{0}$. When $\mathbf{G}_\parallel = \mathbf{0}$

$$\begin{aligned}
\xi(\mathbf{0}) &= \frac{1}{\epsilon_1(\omega)} + \frac{1}{A_0} \left[\frac{1}{\epsilon_2(\omega)} - \frac{1}{\epsilon_2(\omega)}\right] \int_0^1 r dr \int_0^{2\pi} d\varphi \\
&= \frac{1}{\epsilon_1(\omega)} + \frac{1}{A_0} \left[\frac{1}{\epsilon_2(\omega)} - \frac{1}{\epsilon_2(\omega)}\right] \left(\frac{1}{2}\right) (2\pi) \\
&= \frac{1}{\epsilon_1(\omega)} + \frac{A_b}{A_0} \left[\frac{1}{\epsilon_2(\omega)} - \frac{1}{\epsilon_2(\omega)}\right] = \frac{1}{\epsilon_1(\omega)} + f\Delta\xi
\end{aligned} \tag{2.2.44}$$

where $A_b = \pi$ is the area of the base since the base is a circle of radius $r_b = 1$, $f = A_b/A_0$ is the filling fraction and $\Delta\xi$ is given by the equation (2.2.10).

When $\mathbf{G}_\parallel \neq \mathbf{0}$

$$\xi(\mathbf{G}_\parallel) = \frac{1}{A_0} \left[\frac{1}{\epsilon_2(\omega)} - \frac{1}{\epsilon_2(\omega)}\right] \int_0^1 \int_0^{2\pi} e^{-i\mathbf{G}_\parallel \cdot \mathbf{r}_\parallel} r dr d\varphi \tag{2.2.45}$$

In this case the integral can be evaluated as follows, considering that

$$\mathbf{G}_\parallel \cdot \mathbf{r}_\parallel = Gr\cos(\theta) = -Gr\sin\left(\theta - \frac{\pi}{2}\right)$$

where θ is the angle between $\mathbf{G}_\parallel$, and $\mathbf{r}_\parallel$ and $G = \sqrt{G_x^2 + G_y^2}$ and $r = \sqrt{x^2 + y^2}$ are the magnitud of the vectors $\mathbf{G}_\parallel$ and $\mathbf{r}_\parallel$ respectively. It is also important having in account that [1, 9]

$$e^{ix\sin\phi} = \sum_{l=-\infty}^{\infty} J_l(x) e^{il\phi} \quad \text{and} \quad \frac{d}{dx}\left[x^l J_l(x)\right] = x^l J_{l-1}(x)$$

where $J_l(x)$ is the Bessel function of the lth order[1]. So, the previous integral becomes

$$\begin{aligned}\int_0^d \int_0^{2\pi} e^{-i\mathbf{G}_\parallel \cdot \mathbf{r}_\parallel} r dr d\varphi &= \int_0^1 \int_0^{2\pi} e^{iGr\sin\left(\theta - \frac{\pi}{2}\right)} r dr d\varphi \\ &= \int_0^1 dr \int_0^{2\pi} r \sum_{l=-\infty}^{\infty} J_l(Gr) e^{il\varphi} d\varphi \\ &= 2\pi \int_0^1 r J_0(Gr) dr \\ &= \frac{2\pi}{G} J_1(G) \qquad (2.2.46)\end{aligned}$$

hence

$$\xi(\mathbf{G}_\parallel \neq 0) = \xi_{o,p} = 2\frac{A_b}{A_0}\left[\frac{1}{\epsilon_2(\omega)} - \frac{1}{\epsilon_2(\omega)}\right]\frac{J_1(G)}{G} = 2f\Delta\xi\frac{J_1(G)}{G} \qquad (2.2.47)$$

In general, with the variable changes $o \to q - l$ and $p \to s - m$, the quantity ξ is given by

$$\xi(\mathbf{G}_\parallel) = \begin{cases} \frac{1}{\epsilon_1(\omega)} + f\Delta\xi & \text{if } \mathbf{G}_\parallel = \mathbf{0} \\ \\ 2f\Delta\xi\frac{J_1(G)}{G} & \text{if } \mathbf{G}_\parallel \neq \mathbf{0} \end{cases} \qquad (2.2.48)$$

For an elliptic basis the similarity theorem is used [8]:

Theorem 1 (Similarity)**.** *If $\mathcal{F}\{g(x,y)\} = G(f_x, f_y)$, where $G(f_x, f_y)$ is the Fourier transform of $g(x,y)$ and f_x and f_y are the spatial frequencies, then*

$$\mathcal{F}\{g(ax, by)\} = \frac{1}{|ab|} G\left(\frac{f_x}{a}, \frac{f_y}{b}\right) \qquad (2.2.49)$$

with a and b constants.

For an elliptical base, the dielectric function is described as

$$\epsilon(\mathbf{r}, \omega) = \epsilon_1(\mathbf{r}, \omega) + [\epsilon_2(\mathbf{r}, \omega) - \epsilon_1(\mathbf{r}, \omega)] \operatorname{circ}\left(\sqrt{\frac{x^2}{r_x^2} + \frac{y^2}{r_y^2}}\right), \qquad (2.2.50)$$

where r_x and r_y are the semi-axis in x and y directions, respectively.

Considering that

$$\mathcal{F}\left\{\operatorname{circ}\left(\sqrt{x^2 + y^2}\right)\right\} = \frac{2\pi}{G} J_1(G) = 2\pi \frac{J_1\left(\sqrt{G_x^2 + G_y^2}\right)}{\sqrt{G_x^2 + G_y^2}}, \qquad (2.2.51)$$

and using the similarity theorem, the Fourier transform for an elliptical base is

$$\mathcal{F}\left\{\operatorname{circ}\left(\sqrt{\frac{x^2}{r_x^2} + \frac{y^2}{r_y^2}}\right)\right\} = 2\pi r_x r_y \frac{J_1\left(\sqrt{r_x^2 G_x^2 + r_y^2 G_y^2}\right)}{\sqrt{r_x^2 G_x^2 + r_y^2 G_y^2}}. \qquad (2.2.52)$$

If $r_x = r_y$ the Fourier coefficients corresponds to a circular base of radius $r_0 = r_x = r_y$.

This way, for an elliptical base, the Fourier coefficients are given by

$$\xi(\mathbf{G}_\parallel) = \begin{cases} \frac{1}{\epsilon_1(\omega)} + f\Delta\xi & \text{if } \mathbf{G}_\parallel = \mathbf{0} \\ 2f\Delta\xi \frac{J_1\left(\sqrt{r_x^2 G_x^2 + r_y^2 G_y^2}\right)}{\sqrt{r_x^2 G_x^2 + r_y^2 G_y^2}}, & \text{if } \mathbf{G}_\parallel \neq \mathbf{0} \end{cases} \tag{2.2.53}$$

where $f = A_b/A_0$ is the filling fraction, $A_b = \pi r_x r_y$ is the ellipse area, and A_0 is the base area.

2.2.2 Square lattice

For a square lattice, the lattice vectors are given by

$$\boldsymbol{a}_1 = a\hat{\boldsymbol{e}}_{\boldsymbol{x}} \tag{2.2.54}$$

$$\boldsymbol{a}_2 = a\hat{\boldsymbol{e}}_{\boldsymbol{y}} \tag{2.2.55}$$

where $\hat{\boldsymbol{e}}_x$ and $\hat{\boldsymbol{e}}_y$ are the unit vectors in x and y directions, respectively, and $\boldsymbol{a}$ is the size of the unit cell or lattice constant.

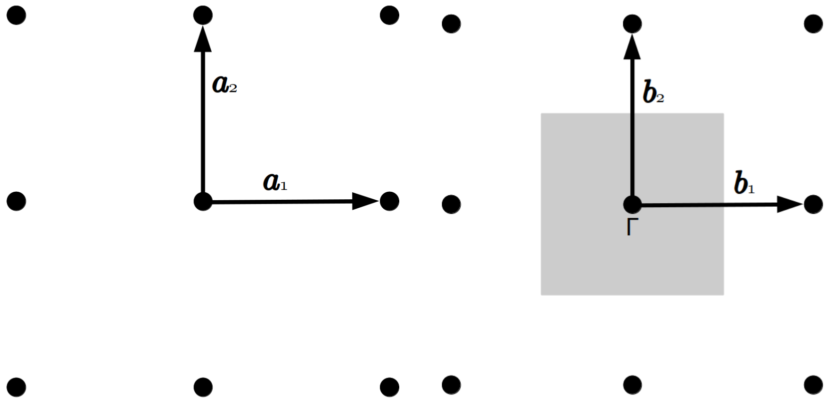

(a) Direct lattice (b) Reciprocal lattice

Figure 2.6: Square lattice.

On the other hand, the reciprocal vectors, using the equations (2.1.26) and (2.1.27) are

$$\boldsymbol{b}_1 = \frac{2\pi}{a}\hat{\boldsymbol{e}}_{\boldsymbol{x}} \tag{2.2.56}$$

$$\boldsymbol{b}_2 = \frac{2\pi}{a}\hat{\boldsymbol{e}}_{\boldsymbol{y}} \tag{2.2.57}$$

so,

$$\mathbf{G}_\parallel = \mathbf{G} = o\boldsymbol{b}_1 + p\boldsymbol{b}_2 = o\frac{2\pi}{a}\hat{\boldsymbol{e}}_{\boldsymbol{x}} + p\frac{2\pi}{a}\hat{\boldsymbol{e}}_{\boldsymbol{y}} \tag{2.2.58}$$

with o and p integers and $G_x = 2\pi o/a$ and $G_y = 2\pi p/a$. Hence

$$\mathbf{G} \cdot \mathbf{r} = \left(o\frac{2\pi}{a}\hat{\boldsymbol{e}}_{\boldsymbol{x}} + p\frac{2\pi}{a}\hat{\boldsymbol{e}}_{\boldsymbol{y}} \right) \cdot (x\hat{\boldsymbol{e}}_{\boldsymbol{x}} + y\hat{\boldsymbol{e}}_{\boldsymbol{y}}) = o\frac{2\pi}{a}x + p\frac{2\pi}{a}y \tag{2.2.59}$$

The reciprocal lattice of a square lattice is also another square lattice, but the dimension of the unit cell is different.

2.2.3 Triangular lattice

For a triangular lattice, the lattice vectors have a x-component and a y-component given by

$$\boldsymbol{a}_1 = \frac{a}{2}\hat{\boldsymbol{e}}_{\boldsymbol{x}} + \frac{\sqrt{3}}{2}\hat{\boldsymbol{e}}_{\boldsymbol{y}} \tag{2.2.60}$$

$$\boldsymbol{a}_2 = \frac{a}{2}\hat{\boldsymbol{e}}_{\boldsymbol{x}} - \frac{\sqrt{3}}{2}\hat{\boldsymbol{e}}_{\boldsymbol{y}} \tag{2.2.61}$$

where a is the size of the unit cell or lattice constant. These vectors are shown in Fig. 2.7a.

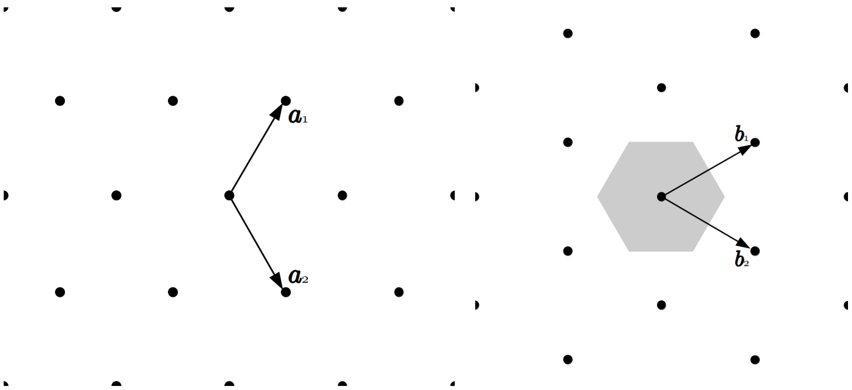

(a) Direct lattice. (b) Reciprocal lattice.

Figure 2.7: Triangular lattice.

Again, using the equations (2.1.26) and (2.1.27), the reciprocal vectors are

$$\boldsymbol{b}_1 = \frac{2\pi}{a}\left(\hat{\boldsymbol{e}}_{\boldsymbol{x}} + \frac{1}{\sqrt{3}}\hat{\boldsymbol{e}}_{\boldsymbol{y}}\right) \tag{2.2.62}$$

$$\boldsymbol{b}_2 = \frac{2\pi}{a}\left(\hat{\boldsymbol{e}}_{\boldsymbol{x}} - \frac{1}{\sqrt{3}}\hat{\boldsymbol{e}}_{\boldsymbol{y}}\right) \tag{2.2.63}$$

as shown in Fig. 2.7b.

In this case

$$\mathbf{G}_{\|} = \mathbf{G} = o\boldsymbol{b}_1 + p\boldsymbol{b}_2 = \frac{2\pi(o+p)}{a}\hat{\boldsymbol{e}}_{\boldsymbol{x}} + \frac{2\pi(o-p)}{\sqrt{3}a}\hat{\boldsymbol{e}}_{\boldsymbol{y}} \tag{2.2.64}$$

with o and p integers and

$$|\mathbf{G}| = G = G_{o,p} = \frac{2\pi}{a}\sqrt{(o+p)^2 + \frac{(o-p)^2}{3}} \tag{2.2.65}$$

This quantity is important to calculate the coefficients ξ.

2.2.4 Rectangular lattice

The lattice vectors are given by

$$\boldsymbol{a}_1 = a_x \hat{\boldsymbol{e}}_{\boldsymbol{x}} \tag{2.2.66}$$

$$\boldsymbol{a}_2 = a_y \hat{\boldsymbol{e}}_{\boldsymbol{y}} \tag{2.2.67}$$

where a_x and a_y are the rectangular sides in x and y directions respectively, as shown in Fig. 2.8a. Through the equations (2.1.26) and (2.1.27) the reciprocal vectors are

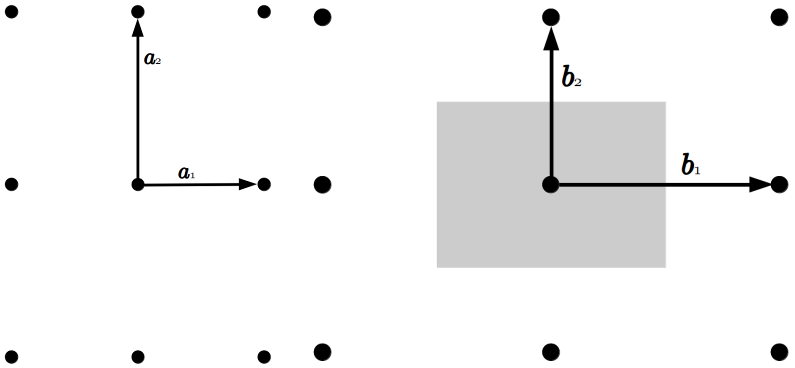

(a) Direct lattice. (b) Reciprocal lattice.

Figure 2.8: Triangular lattice.

$$\boldsymbol{b}_1 = \frac{2\pi}{a_x} \hat{\boldsymbol{e}}_{\boldsymbol{x}} \tag{2.2.68}$$

$$\boldsymbol{b}_2 = \frac{2\pi}{a_y} \hat{\boldsymbol{e}}_{\boldsymbol{y}} \tag{2.2.69}$$

and

$$\mathbf{G}_{\|} = \mathbf{G} = o\boldsymbol{b}_1 + p\boldsymbol{b}_2 = o\frac{2\pi}{a_x}\hat{\boldsymbol{e}}_{\boldsymbol{x}} + p\frac{2\pi}{a_y}\hat{\boldsymbol{e}}_{\boldsymbol{y}} \tag{2.2.70}$$

where o and p are integers.

This way,

$$\mathbf{G}\cdot\mathbf{r} = \left(o\frac{2\pi}{a_x}\hat{\boldsymbol{e}}_{\boldsymbol{x}} + p\frac{2\pi}{a_y}\hat{\boldsymbol{e}}_{\boldsymbol{y}}\right)\cdot(x\hat{\boldsymbol{e}}_{\boldsymbol{x}} + y\hat{\boldsymbol{e}}_{\boldsymbol{y}}) = o\frac{2\pi}{a_x}x + p\frac{2\pi}{a_y}y. \tag{2.2.71}$$

In this case, the reciprocal lattice is a rectangular lattice.

References

[1] Kazuaki Sakoda. *Optical Properties of Photonic Crystals.* Springer, 2005.

[2] Igor A. Sukhoivanov and Igor V. Guryev. *Photonic crystals.* Springer, 2009.

[3] John D. Joannopoulos, Steven G. Johnson, Joshua N. Winn, and Robert D. Meade. *Photonic crystals: molding the flow of light.* Princeton University Press, Princeton,New Jersey, 2008.

[4] Stefan A. Maier. *Plasmonics: Fundamentals and Applications.* Springer, 2007.

[5] P. B. Johnson and R. W. Christy. Optical constants of the noble metals. *Phys. Rev. B*, 6:4370–4379, Dec 1972.

[6] G. Peters and J. H. Wilkinson. $ax = \lambda bx$ and the generalized eigenproblem. *SIAM Journal on Numerical Analysis*, 7(4):479–492, 1970.

[7] Axel Ruhe. Algorithms for the nonlinear eigenvalue problem. *SIAM Journal on Numerical Analysis*, 10(4):674–689, 1973.

[8] J.W. Goodman. *Introduction to Fourier Optics.* McGraw-Hill physical and quantum electronics series. W. H. Freeman, 2005.

[9] George B. Arfken and Hans Jürgen Weber. *Mathematical Methods for Physicists.* Elsevier, 2005.

Chapter 3

Computational techniques

This chapter describes the computational techniques required to meet the established objectives. Several machine learning algorithms were implemented to choose the one with the best performance; each of them is described. Regarding the experimental techniques, in the appendix, a brief description is made of the physical fundamentals of two methods to fabricate nanostructures, which would be adequate to synthesize the systems described in the previous chapter.

Machine learning algorithms

Machine learning is a discipline that involves the development and evaluation of algorithms that enable a computer «learn» that is, to extract «functions» from instances or examples contained in a dataset. On the other hand, a function is a deterministic mapping from a set of input values to one or more output values, that means that, for a specific set of inputs, a function will always return the same outputs [1]. In mathematical language, machine learning algorithms try to learn a function f that predict an output variable Y from an input variable X [2]

$$Y = f(X). \tag{3.0.1}$$

Machine learning algorithms are powerful tools to search a process designed to choose the optimal function, from several of possible functions, with aim to extract insigths and explain the relationships between features in a dataset. The machine learning process involves two step processes: training and inference. In training, a machine learning algorithm processes a part of the dataset and finds the function that best matches the patterns in the data. That function is translated in a computer program called "model", and the analysis of the data to fit the dataset to the model is often referred to as training the model [1].

When the training stage has finished, the model is fixed and the second stage starts. In the inference stage, the model is applied to new instances or examples, which have an unknown output value, aiming the model to accurate predictions. One of the fundamental problem in machine learning is to train accurate models able to do inference on new examples [1].

The main keys to machine learning are to have a dataset of examples or historical instances, a family of possible functions from which the algorithm will search to choose the one that best matches the dataset, and some measured system for evaluating how well each candidate function fits the data [1].

Using the proposed analytical model in this thesis work (see section 2.2 and equation (2.2.24), the optical response of hybrid photonic-plasmonic crystals (PhPl crystals) was calculed for different structural parameters. With the data generated from these calculations, several machine learning algorithms were trained to predict the optical response from the structural parameters, in what is known as "forward design". There is another approach to apply these algorithms, in this case to predict the structural parameters from the particular desired optical response. The latter is known as "inverse design" [3].

In this subsection, a brief description of the implemented machine learning algorithms in this work will be presented. Since these algorithms are a tool for the purpose of the thesis, the description is intended to explain the basic operation of these algorithms, avoiding falling into an exhaustive explanation of the technical details.

Linear and polynomial regression

Regression is a model that assumes a linear or polynomial relation between the input variables and the single output variable [2]. Learning or training a regression model means finding the values of the coefficients used to fit the data available to a linear or polynomial relation [2]. In linear regression, there is an input $\mathbf{x} \in \mathbb{R}^n$ and an output $y \in \mathbb{R}$, and the linear function $h : \mathbb{R}^n \mapsto \mathbb{R}$ that best approximates the relationship between the input and ouput variables is sought [4]. The predictors in linear regression are a set o linear functions

$$\mathcal{H}_{reg} = L_n = \{\mathbf{x} \mapsto \langle \mathbf{w}, \mathbf{x} \rangle + b : \mathbf{w} \in \mathbb{R}^n, b \in \mathbb{R}\}, \tag{3.0.2}$$

where $\langle \ , \ \rangle$ denotes the inner product, while $\mathbf{w}$ and b are parameters of the model that are learned [2, 4, 5].

A «loss function» is defined to determine if $h(\mathbf{x})$ correctly predicts y, measuring the error magnitud [4, 6]. A common way to do this is by means of the «squared loss function» defined as [4]

$$l(h, (\mathbf{x}, y)) = (h(\mathbf{x}) - y)^2. \tag{3.0.3}$$

For a given set $\mathcal{H}$ of linear functions, the regression problem consists in finding a function $h \in \mathcal{H}$ with «small expected loss» or «generalization error» [6]. This error function is defined as [4, 6]

$$L_S = \frac{1}{n}\sum_{i=1}^{n} (h(\mathbf{x}_i) - y_i)^2 . \tag{3.0.4}$$

Finally, the optimization problem consists in finding the parameters $\mathbf{w}$ and b that minimize the loss and error functions, that is [4, 6]

$$\min_{\mathbf{w},b} L_S(h_{\mathbf{w},b}) = \min_{\mathbf{w},b} \frac{1}{n}\sum_{i=1}^{n} (\langle \mathbf{w}, \mathbf{x}_i \rangle + b - y_i)^2 . \tag{3.0.5}$$

This last equation is the base of the «Least squares» technique.

In other cases, a complex model is necessary to model the data available. For polynomial regression, the predictors are polynomials of the form

$$p(x) = a_0 + a_1 x + a_2 x^2 + \ldots + a_n x^n. \tag{3.0.6}$$

For simplicity, consider one-dimensional class of predictors

$$\mathcal{H}_{pol}^n = \{x \mapsto p(x)\} \tag{3.0.7}$$

where $p(x)$ is a polynomial of degree n parameterized by a vector of coefficients $(a_0, a_1, \ldots, a_n)$ [4].

The problem can be solved by reduction to the problem of linear regression. To do this, a map $\psi : \mathbb{R} \to \mathbb{R}^{n+1}$ is defined, so that $\psi(x) = (1, x, x^2, \ldots, x^n)$, and the problem is reduced to

$$p(\psi(x)) = a_0 + a_1 x + a_2 x^2 + \ldots + a_n x^n = \langle \mathbf{a}, \psi(x) \rangle. \tag{3.0.8}$$

Finally, using the least squares algorithm, the optimal coefficients **a** can be found [4].

Decision Trees

Another machine learning algorithm used in regression, classification, and clustering tasks, is decision trees. This technique is based in the learning of a hierarchy of if/else questions, leading to a decision [5]. Decision tree algorithm works by splitting the input space, where different split points or nodes are tried and tested using a «cost function»[2].

Usually the splitting is based in some features of input data, although it is also possible to define a set of splitting rules [4]. This way, each interior node of a decision tree corresponds to a question about the features, where the question can be numerical as $x_i \leqslant a$ for a feature variable x_i and some threshold $a \in \mathbb{R}$ [6].

As an example, Fig. 3.1 shows a decision tree to classify a new pair (x_1, x_2) with two features X_1 and X_2 in five possible labels R_1, R_2, R_3, R_4 and R_5. In this example, the questions are numerical of the form $x_i \leqslant a_j$ and, depending of the result, the the pair (x_1, x_2) is classified in some label R_j, with $j \in \{1, \ldots, 5\}$.

As in the regression problem, there is a cost function, and the split with the best cost, that is, lowest cost, is selected [2]. The cost function of a decision tree used for regression, is the sum squared error given by the equation (3.0.4) [2].

k-nearest neighbors

Unlike the previous algorithms, in k-nearest neighbors, the model stores the training dataset to memorize it, and to predict the label of any new instance on the basis of the labels of its closest neighbors in the training set [2, 4, 5]. This way, there is no learning required, since the predictions for a new instance are made by searching through the entire training set for the k most similar neighbors instances [2].

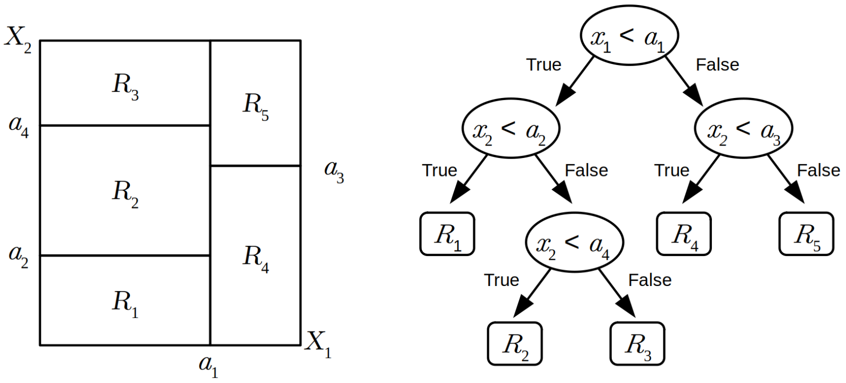

Figure 3.1: Left: Two-dimensional diagram for two features space divided in five domains. Right: Decision tree to classify a pair (x_1, x_2).

A distance measure is used to determine the k-nearest neighbors to a new instance, that is, to the most similar instances in the training dataset [2]. Therefore, the training instances X are assigned a metric function ρ. This way, the metric function $\rho : X \times X \rightarrow \mathbb{R}$ returns the distance between any two elements of X [4]. When the training instances are real values, one of the most popular distance measure used is Euclidean distance.

For example, for $X = \mathbb{R}^n$, the Euclidean distance is defined as [2, 4]

$$\rho(\mathbf{x}, \mathbf{x}') = \| \mathbf{x} - \mathbf{x}' \| = \sqrt{\sum_{i=1}^{n} (x_i - x_i')^2}. \tag{3.0.9}$$

where $\mathbf{x}, \mathbf{x}' \in X$. However, Euclidean distance is not the only possible metric function, there are other such as Hamming distance, Manhattan distance or Minkowski distance [2]. For regression problems, prediction is based on an average target of the k-nearest neighbors [2, 4].

Artificial neural networks (deep learning)

The artificial neural networks (ANN) are a computational model inspired by the structure of neural networks in the brain [1, 4, 5]. Thus, an ANN is a simplification of the brain, where neurons are connected to each other in a complex communication network, giving the brain the ability to perform quite complex tasks [1, 4].

An ANN is a network of simple information processing units, called neurons and is able to model complex relationships from the interactions between a set of simple neurons [1]. Figure 3.2 shows an example of an ANN. It is composed by an input layer represented by squares, and three hidden layers connected to the input one layer and an output layer connected to the hidden layers. The input layer contains the input data X. The hidden layers are connected to the input layer and are composed by neurons, the information processing unit, represented by circles. Finally, the output layer connected to the hidden layers contains the output data Y.

Each neuron takes numerical values from the neurons of previous layers as an input and maps them to a single output value. Each input to a processing neuron is either values of input

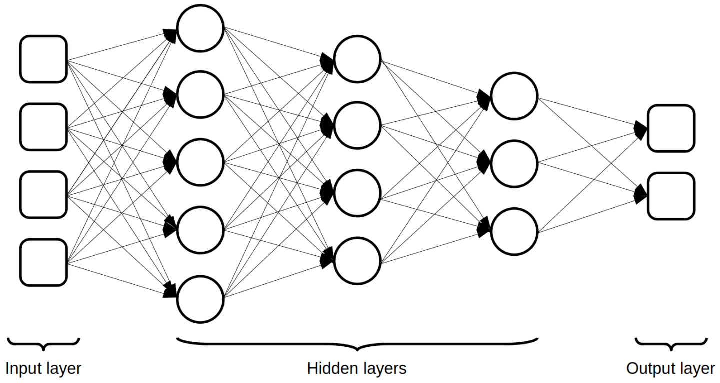

Figure 3.2: Artificial neural network.

layer or the output of another processing neuron. The arrows in the diagram represents the information flows from the neuron in a layer to the neurons in other layers [1]. The arrows or connections have a numerical value associated with them called «weight», and it affects how a neuron processes the receiving information along the connection. Essentially, training an ANN involves searching for the optimal set of weights [1].

To process information, each neuron maps the input to an output by means of a «weighted sum» of the form

$$z = \sum_{i=1}^{n} w_i x_i \tag{3.0.10}$$

over the input data. After that, the result of the weighted sum is passed to a second function that maps it to the neuron final output value [1, 2]. For the second function is possible to use different types of functions depending on the model complexity [1]. The output is called "activation value" so this second function is known as an "activation function" [1, 2].

Figure 3.3 shows how works a neuron in an ANN. The weighted sum is represented by Σ and the activation function is represented by φ. The diagram illustrates the information process,

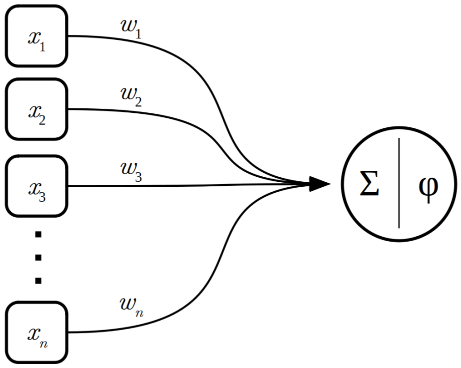

Figure 3.3: Model of an artificial neuron.

where the neuron receives n inputs $x_1, x_2, \dots x_n$, and each connection has an associated weight w_i, and the mathematical computation is given by the equation (3.0.10) [1, 2]. Then, the weighted sum result z pass through the activation function φ, and the output is given by

$$\text{output} = \text{activation\_function}\left(\sum_{i=1}^{n} w_i x_i\right) = \varphi\left(\sum_{i=1}^{n} w_i x_i\right) \tag{3.0.11}$$

The activation function defines a threshold at which the neuron is activated and the strength of the output signal [1, 2]. Some non-linear functions can be used as activation functions such as step function, «rectifying nonlinearity» also known as rectified linear unit or relu, logistic or «sigmoid», tangens hyperbolicus [1, 2], etc. Since the weighted sum is a linear model, using nonlinear function as an activation function enables a neural network to learn a nonlinear model from input to output [1].

As previous algorithms, a loss function is defined to measure the error and search for the best parameters. Learning a model involves several optimization processes such as data preparation, weight updates, «stochastic gradient descent», and others to find optimal parameters to have an accurate model [2]. In general, to solve problems using ANN, each of the neurons in a network solves one component of the larger problem, and the overall problem is solved by combining these component solutions [1]. Finally, when the ANN is trained it is able to make predictions for regression, classification and clustering tasks.

References

[1] John D. Kelleher. *Deep learning.* The MIT Press, Cambridge, MA, 2019.

[2] Jason Brownlee. *Master Machine Learning Algorithms.* eBook, 2017.

[3] Dianjing Liu, Yixuan Tan, Erfan Khoram, and Zongfu Yu. Training deep neural networks for the inverse design of nanophotonic structures. *ACS Photonics*, 5(4):1365–1369, 2018.

[4] Shai Shalev-Shwartz and Shai Ben-David. *Understanding Machine Learning: From Theory to Algorithms.* Cambridge University Press, 2014.

[5] Andreas C. Müller and Sarah Guido. *Introduction to Machine Learning with Python.* O'Reilly, 2017.

[6] Mehryar Mohri, Afshin Rostamizadeh, and Ameet Talwalkar. *Foundations of Machine Learning.* The MIT Press, 2018.

Chapter 4

Results

The results of the theoretical and numerical study of the proposed photonic-plasmonic systems are presented. The chapter is divided into three sections. The first section presents the results of the theoretical model, which include the bandgap formation and how its formation of the bandgap and how its properties change as a function of the crystal parameters, such as the size such as the lattice size, and the filling fraction. These theoretical results are compared with experimental results reported in the literature.

Subsequently, the results of the performance of the algorithms for predicting the desired properties are presented. As mentioned in the previous chapter, several machine learning algorithms were tested and compared to determine the one with the best performance in predicting the target variables. Finally, the results of the design of the hybrid photonic-plasmonic crystals are shown.

Other experimental results concerning the optical characterization method are presented in an appendix. This is not included in the main part of the manuscript, since the system analyzed with the leakage radiation microscopy technique is not directly related to the proposed systems studied theoretically. However, this appendix was added as a proof of concept and to show the operation of the device to experimentally characterize the proposed systems. In addition, the optically studied physical system is a calibration tool of the optical device for the analysis of other samples.

4.1 Theoretical model results

The theoretical model is used to study the particular structures composed of a dielectric photonic crystal on Au or Ag thin films. The photonic crystal consists of a periodic array of PMMA columns in an air matrix. The crystal lattices analyzed are a one-dimensional stack of interleaved PMMA and air layers, while the two- dimensional cases consist of a matrix of PMMA columns with rectangular and elliptical cross-sections.

The refractive index of PMMA has small variations in the 550-2000 nm range, and does not represent a significant change in the PMMA-Au dispersion relation if its dielectric function is assumed to be constant.

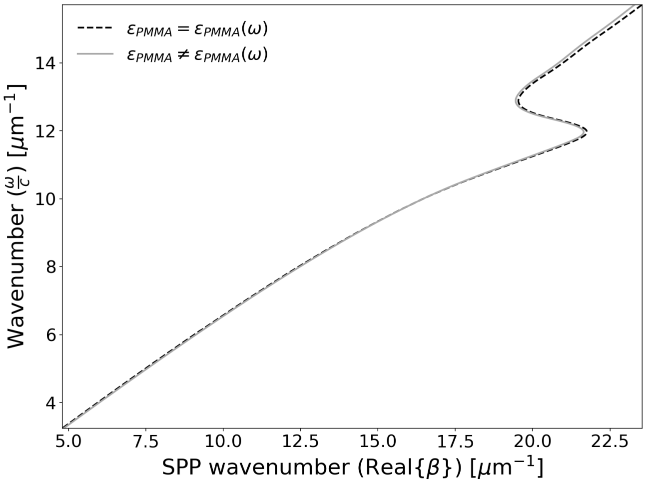

Figure 4.1: SPP dispersion relation for a PMMA-Au interface.

Figure 4.1 shows the SPP dispersion relation for a PMMA-Au interface. The dashed line is the dispersion relation considering a frequency-dependent PMMA dielectric function, as in reference [1]. The solid gray line is the dispersion relation considering a constant PMMA dielectric function. The values of the dielectric functions are $\epsilon_{PMMA} = \epsilon_b = 2.2$ for PMMA, taking the value of PMMA dielectric function at $\lambda = 633$ nm [1]; and $\epsilon_{air} = \epsilon_a = 1$ for air, such that the dielectric constants contrast is ϵ_b/ϵ_a=2.2.

As an example, Fig. 4.2 shows the inverse of dielectric function data for an air-Au interface (black circles), and for a PMMA-Au interface (black square), in the wavelength range 548.6-1937 nm. The black diamonds and triangles are the inverse of dielectric function data for air-Ag and PMMA-Ag interfaces in the range of wavelengths from 331.5 to 1937 nm, respectively. For all the interfaces, the inverse of the dielectric function is calculated using Johnson & Christy data of permittivity for Au and Ag [2]. The solid and dashed lines are the inverse of dielectric function data fitted to equation (2.2.18).

The wavelength ranges for data fitting were chosen to avoid the maximum value of the effective refractive index since, near that value, SPP propagation is considerably attenuated. The maximum value of the effective refractive for a dielectric-Au interface is located at approximately 520 nm, while for a dielectric-Ag interface, it occurs approximately at 340 nm.

The data fit parameters for the dielectric-Au interface are $\gamma_1 = 0.115218$, $\gamma_2 = 0.266632$, $\gamma_3 = -0.002649$ and $b = 12.368228$. For the dielectric-Ag interface, the data fit parameters are $\gamma_1 = 0.153906$, $\gamma_2 = 0.901489$, $\gamma_3 = -0.003654$ and $b = 19.361642$.

In the case of a dielectric-Au interface, the data fit of the inverse of the effective dielectric function has an asymptotic behavior at $b = 12.368228$, which is equivalent to a wavelength of approximately 508 nm. For a dielectric-Ag interface, the asymptotic behavior is at $b = 19.361642$, corresponding to a wavelength of about 324 nm.

To solve equation (2.2.24) for the four chosen different crystal lattices as a function of the lattice length and base size for two bases with different geometries, a python code was written.

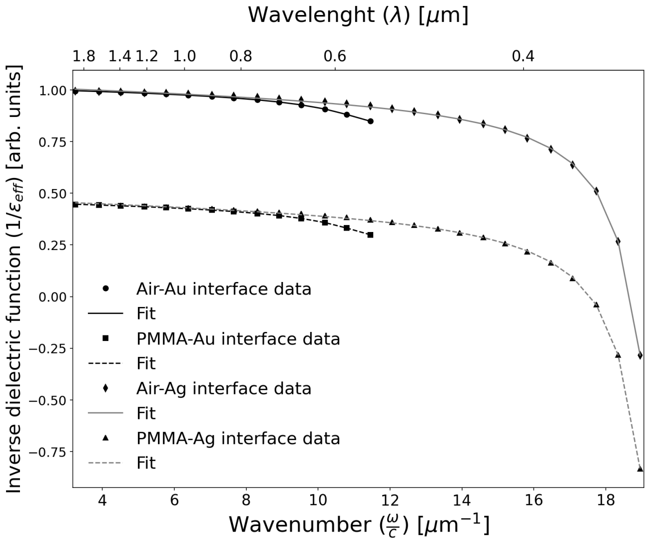

Figure 4.2: Inverse of dielectric function for four different dielectric-Au and dielectric-Ag interfaces.

4.1.1 One-dimensional photonic-plasmonic crystal

The one-dimensional photonic-plasmonic (PhPl) crystals studied is formed by layers of PMMA with width d and air on a Au or Ag thin film. The system is shown in Fig. 4.3

Figure 4.3: The one-dimensional dielectric-metallic PhPl crystal.

Figures 4.4 shows the band structure of a one-dimensional PhPl crystal with a lattice constant $a = 300$ nm and width $d = 150$ nm, so the filling fraction is $f = d/a = 0.5$. With these parameters, it has a bandgap centered at $\lambda_c = 787.22$ nm, and with a bandgap width $\Delta\lambda = 179.74$ nm for the dielectric-Au PhPl crystal. In the case of dielectric-Ag PhPl crystal, the center and width of the bandgap are $\lambda = 782.09$ nm and $\Delta\lambda = 181.78$, respectively. The properties of both bandgaps are similar when using the same crystal parameters, since the effective refractive indexes of a dielectric-Au interface and a dielectric-Ag interface are similar in the electromagnetic spectrum where the bandgap arises.

To test the validity of the model, the band structure of a one-dimensional PhPl crystal was calculated with two different filling fractions, and compared with the dispersion relations of

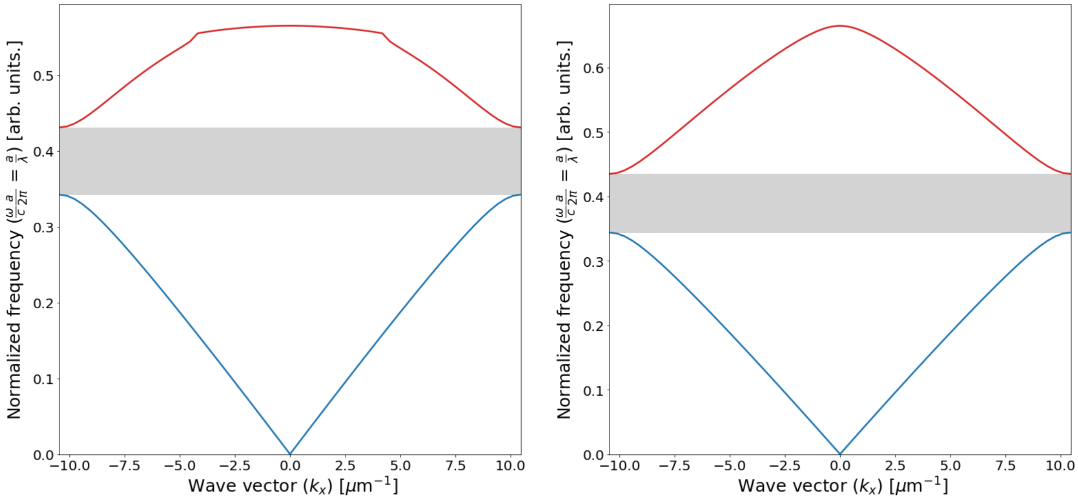

(a) One-dimensional dielectric-Au PhPl crystal band structure.

(b) One-dimensional dielectric-Ag PhPl crystal band structure.

Figure 4.4: Band structures of a one-dimensional PhPl crystals.

air-Au interface and air-PMMA interface. The first value is $f = 0$, which corresponds to a pure air-Au interface. The agreement shown in Fig. 4.5a between the PhPl crystal band structure

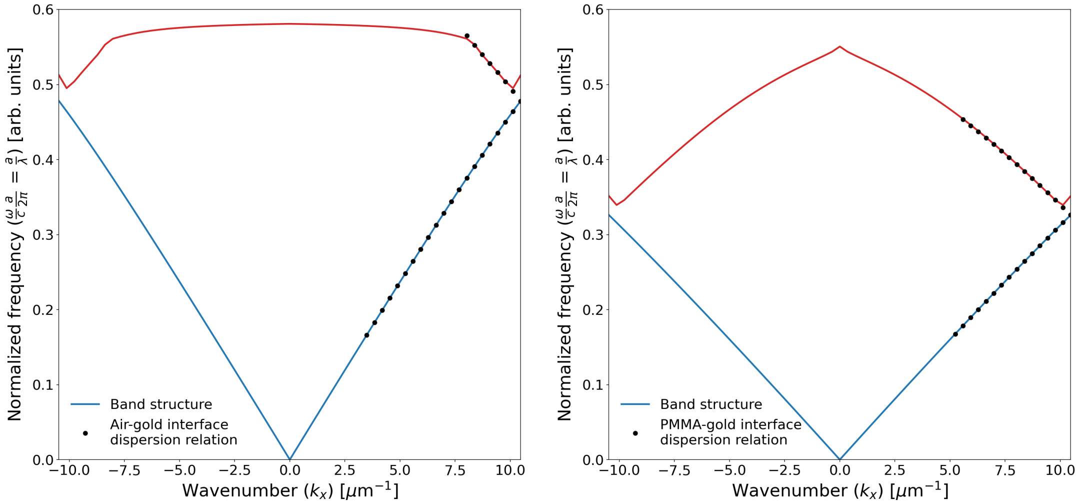

(a) Band structure of a 1-D dielectric-Au PhPl crystal for $f = 0$.

(b) Band structure of a 1-D dielectric-Ag PhPl crystal for $f = 1$.

Figure 4.5: Band structures of a one-dimensional PhPl crystals and dispersion relation for air-Au and PMMA-Au interfaces.

(represented by blue and red lines) for $f = 0$ and the dispersion relation of the SPP in an air-Au interface (black points) is evident. On the contrary, for $f = 1$, the physical system is a PMMA-Au interface, since the unit cell is completely covered by the PMMA layer. Figure 4.5b shows the corresponding band structure. As above, the blue and red lines are the PhPl crystal band structure, while the gray points are the dispersion relation of the SPP in a PMMA-Au interface. Again, there is a total agreement between the band structure and the dispersion relation.

To understand how the optical response is modified as a function of crystal parameters, the band structure was calculated for different lattice constants and filling fractions for a dielectric-Au PhPl crystal.

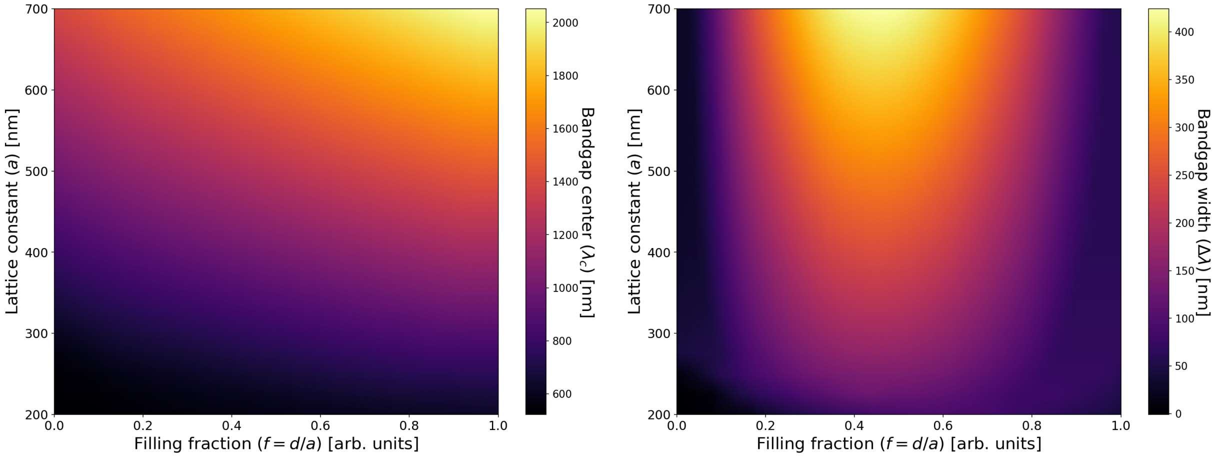

(a) Bandgap center.

(b) Bandgap width.

Figure 4.6: Bandgap properties for a one-dimensional dielectric-Au PhPl crystal.

Figure 4.6a shows the behavior of the bandgap center as a function of lattice constant and filling fraction. As it is shown in the plot, the bandgap center increases monotonically as the lattice constant and filling fraction do too. The above is consistent with results reported in reference [3], where it is observed that the center of the bandgap is red shifted as the filling fraction increases.

On the other hand, the bandgap width as a function of the lattice constant and filling fraction is shown in Figure 4.6b. In this case, $\Delta\lambda$ increases as the lattice constant do. However, as a function of the filling fraction, it increases until it reaches a maximum near $f = 0.44$, and then it decreases to zero. Also, an analogous result is reported in the reference [3], where it is concluded that the maximum width of the bandgap is close to $f = 0.42$ for SiO_2 ridges.

4.1.2 Square lattice

The first two-dimensional PhPl crystal studied is a square array of PMMA columns of rectangular cross-section, so the system has an air-Au interface and a PMMA-Au interface, as shown in Fig. 4.7. The crystalline parameters are the lattice constant a and the base sides d_x and d_y

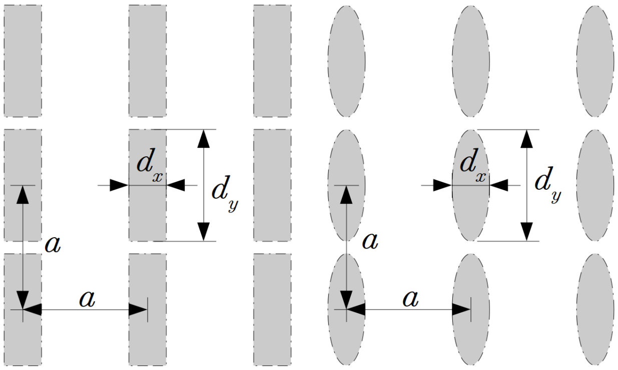

(a) Rectangular base. (b) Elliptical base.

Figure 4.7: Square lattice with two different bases.

in the x and y directions, respectively. Thus, the filling fractions are

$$f_{rec} = \frac{d_x d_y}{a^2} \quad \text{and} \quad f_{ell} = \frac{\pi d_x d_y}{4a^2}, \tag{4.1.1}$$

for the rectangular and elliptical bases, respectively.

The white zones correspond to the interface air-Au with effective dielectric function

$$\epsilon_1 = \frac{\epsilon_a \epsilon_{\text{Au}}}{\epsilon_a + \epsilon_{\text{Au}}}, \tag{4.1.2}$$

where ϵ_a is dielectric constant of the air and ϵ_{Au} is the dielectric function of Au. The gray zones are the interface PMMA-Au with effective dielectric function

$$\epsilon_2 = \frac{\epsilon_b \epsilon_{\text{Au}}}{\epsilon_b + \epsilon_{\text{Au}}}, \tag{4.1.3}$$

where ϵ_b is dielectric constant of the PMMA, which value is 2.2 at $\lambda = 633$ nm [1].

This PhPl crystal has a lattice constant $a = 300$ nm, a major axis $d_x = 165$ nm and minor axis $d_y = 132$ nm. Solving the equations (2.2.24) to find eigenvalues α and wavenumbers ω/c as a function of k_x and k_y, yields the band structure shown in Fig. 4.8a for dielectric-Au PhPl crystal, while the band structure for dielectric-Ag PhPl Crystal shown in Fig. 4.8b.

In the band structure of the dielectric-Au PhPl crystal, there is a partial bandgap along the $\Gamma - \text{X}$ orientation centered at 696.19 nm with a width of 90.30 nm, that is, no waves are propagating in the range 651.04 - 731.34 nm. In addition, there is another partial bandgap in the $\text{M} - \Gamma$ orientation, centered at 573.64 nm and with a width of 72.55 nm.

Note that bands 2 and 3 (black and red curves, respectively) coincide at Γ point with a value of 0.57, which is equivalent to a wavelength of about 526.32 nm. Moreover, the upper bands cluster near this same value, that is, close to the fitting parameter b of equations (2.2.19) and

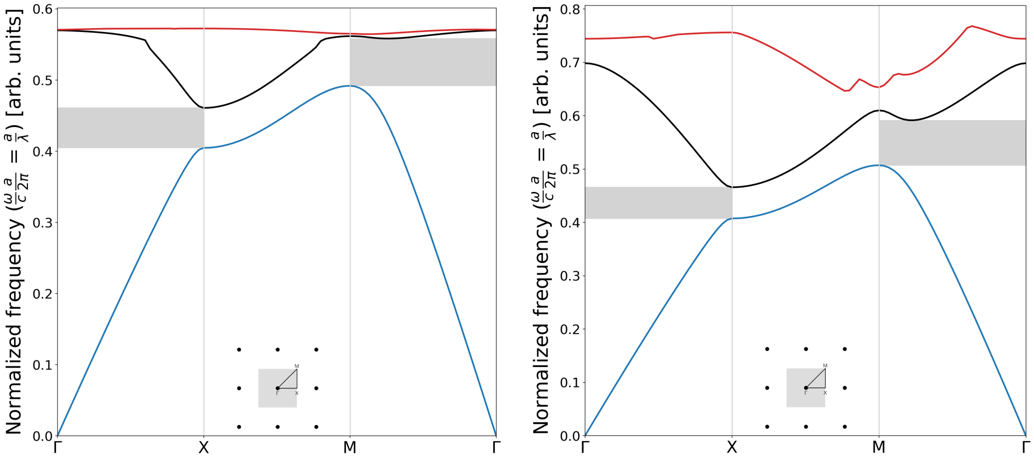

(a) Dielectric-Au PhPl crystal band structure.

(b) Dielectric-Ag PhPl crystal band structure.

Figure 4.8: Band structure of two different dielectric-metallic PhPl crystals with a square lattice and an elliptical base.

(2.2.20) for a dielectric-Au interface. This means that the bandgap is within the wavelength range in which the data fitting was performed.

Using the same parameters as above, the bandgap structure of a dielectric-Ag PhPl crystal is shown in Fig. 4.8b. The partial bandgap in the $\Gamma - \mathrm{X}$ orientation is centered at 689.94 nm and has a width of 92.37 nm. The partial bandgap in the $\mathrm{M} - \Gamma$ orientation is centered at 549.22 nm and has a width of 84.26 nm.

In this case, the properties of the bandgap in the $\Gamma - \mathrm{X}$ orientation are similar to those of the dielectric-Au PhPl crystal, because the effective refractive indexes are similar in this frequency range. However, the characteristics of both bandgaps in the $\mathrm{M} - \Gamma$ orientation are remarkably different. This is due to the difference in the effective refractive indexes in that range of the electromagnetic spectrum. As in the previous case, for a dielectric-Ag PhPl crystal, the upper bands are clustered near the parameter b of the fitting equation for the inverse of the effective dielectric function. This means that the dielectric-Ag PhPl crystal can be used over a wider range of wavelengths.

On the other hand, the existence of two partial bandgaps is due to a low dielectric constant contrast. For example, in a PhPl crystal with the same parameters, but with a dielectric constant contrast of $\epsilon_b/\epsilon_a = 9$, there are two complete bandgaps, as shown in Fig. 4.9. In this case, one of the bandgaps has a width of $\Delta\lambda = 243.76$ nm and is centered at $\lambda_c = 966.93$. The other bandgap has a width of $\Delta\lambda = 38.22$ nm and is centered at $\lambda_c = 711.9$ nm. Furthermore, as the contrast of the dielectric constants increases, the width and center of the bandgap also increase.

As in the one-dimensional case, the center and width of the bandgap were calculated for a square crystal with rectangular and elliptical bases. As it is could be verified, the geometry of

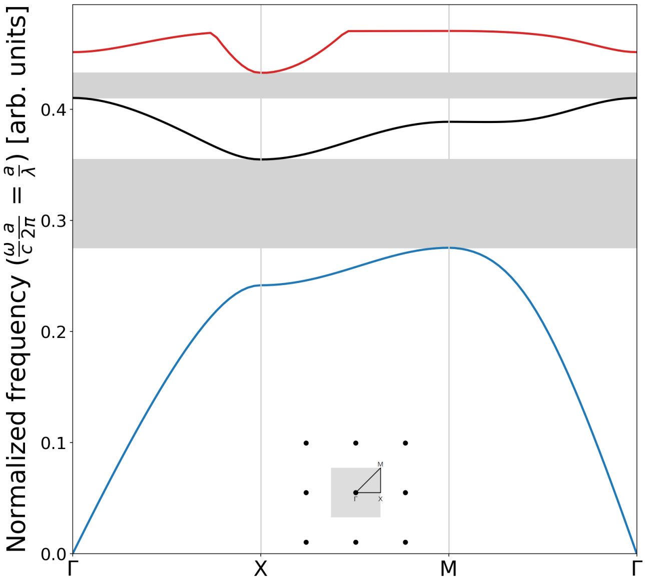

Figure 4.9: Band structure of a square lattice with an elliptical base. This band structure corresponds to a lattice constant of $a = 300$ nm, $d_x = 165$ nm and $d_y = 132$ nm, but with a dielectric constants contrast of $\epsilon_b/\epsilon_a = 9$.

the base cross-section does not represent a significant difference in the band structure, the key parameter is the filling fraction.

It is important to note that this range of forbidden frequencies can be tuned by changing the ratio d_x/a and d_y/a, that is, changing the base size concerning the unit cell size. This was done from $d_x/a = 0$ to $d_x/a = 1$ and $d_y/a = 0$ to $d_y/a = 1$, and for different lattice constants, from $a = 200$ nm to $a = 700$ nm. With this, the center and width of the bandgap were calculated as a function of the parameters a and f. This is shown in Fig. 4.10.

As it is shown in the heat map 4.10a, the center of the bandgap is an increasing function of the lattice constant and the filling fraction. Respect to the bandgap width, it is a monotonically increasing function of the lattice constant, however as a function of the filling fraction $f = d_x d_y/a$, as f increases, the bandgap width also increases until it reaches a maximum near $f = 0.38$, and then decreases to a minimum value at $f = 1$.

Considering the above, to tune the center and width of the bandgap for a square lattice, it is necessary to adjust the lattice constant and the filling fraction. In addition, it is possible to obtain a complete bandgap by varying the contrast of the dielectric constants.

4.1.3 Triangular lattice

The same bases used in the square lattice, rectangular and elliptical, were also studied for the triangular lattice. As defined above, the white zone is the air-Au interface, while the gray zone is the PMMA-Au interface, as shown in Figure 4.11. Solving the eigenvalue equation, unlike the square lattice, the triangular lattice exhibits a complete bandgap even at low dielectric

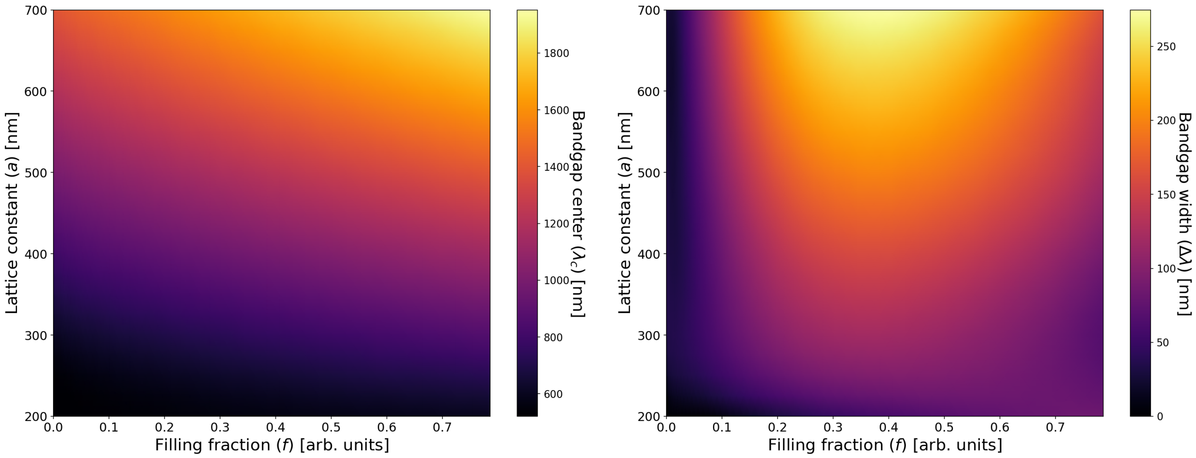

(a) Bandgap center.

(b) Bandgap width.

Figure 4.10: Bandgap properties for a dielectric-Au PhPl crystal with a square lattice and an elliptical base.

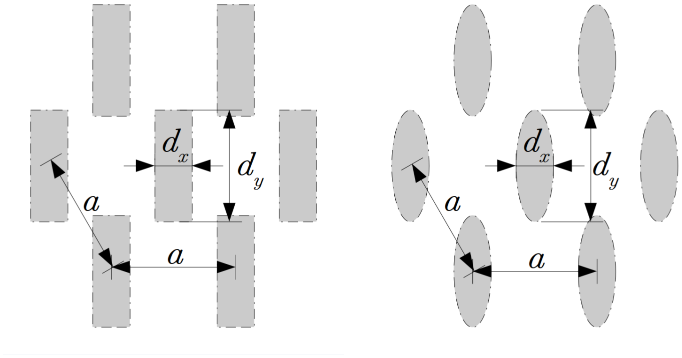

(a) Rectangular base.

(b) Elliptical base.

Figure 4.11: Triangular lattice with two different bases.

constant contrast, as shown in the photonic band structure of a dielectric-Au and dielectric-Ag PhPl crystals in Fig. 4.12.

The band structures were calculated with a lattice constant a = 330 nm, a major axis $d_x = 130$ nm and a minor axis $d_x = 100$ nm. With these parameters, for the dielectric-Au PhPl crystal, there is a complete bandgap centered at $\lambda_c = 631.33$ nm with a width of $\Delta\lambda = 42.82$ nm. For the dielectric-Ag PhPl crystal, the bandgap is centered at $\lambda_c = 620.16$ nm with a width of $\Delta\lambda = 40.98$ nm. Comparing both band structures, the significant change is in the bandgap center. The difference between both bandgap centers is about 11 nm.

The results provided by the model are compared with experimental results reported in

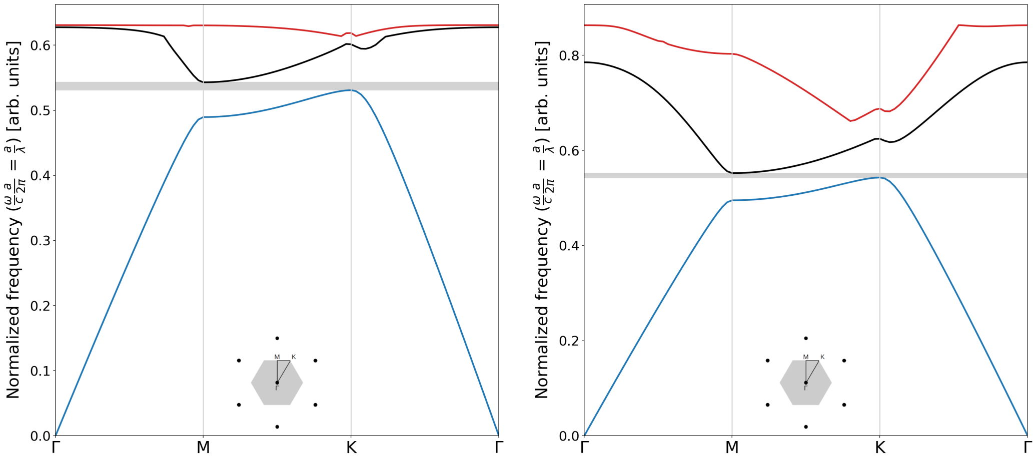

(a) Dielectric-Au PhPl crystal band structure

(b) Dielectric-Ag PhPl crystal band structure

Figure 4.12: Band structure of two different dielectric-metallic PhPl crystals with a triangular lattice and an elliptical base.

reference [4]. In that case, the base is a circular Au structure of diameter $d = 200$ nm in a triangular lattice with a lattice constant $a = 400$ nm. In the experimental data of Bozhevolnyi *et al.*, a high reflectivity is reported at $\lambda = 782$ nm, suggesting that this wavelength is within the bandgap. Furthermore, it is mentioned that the intensity of the reflected SPPs practically vanishes at $\lambda = 815$ nm, that is, this wavelength does not belong to the bandgap.

Using that parameters in the analytical model, it calculates a bandgap centered at $\lambda_c = 774.041$ nm with a width of $\Delta\lambda = 52.141$ nm. Although it is not the same physical system, the results are consistent.

Regarding the dielectric-Ag systems, the theoretical results are compared with the experimental one reported in reference [5]. That case, the triangular lattice has a period $a = 300$ nm and the base have a diameter $d = 200$ nm. With he experimental results, a bandgap centered at $\lambda_c = 634.527$ nm and with a width $\Delta\lambda = 29.211$ nm is reported.

With the same parameters, the theoretical model calculates a bandgap centered at $\lambda_c = 638.626$ nm with a width $\Delta\lambda = 41.285$ nm. Although the bases are different in composition, the calculated theoretical result is consistent with that reported experimentally in reference [5], showing that the lattice constant and the size of the base are determining parameters in the properties of the bandgap.

As in the previous case, the bandgap properties,λ_c and $\Delta\lambda$, were calculated for various lattice constants a, in the range from 300 nm to 800 nm, and for different filling fractions f, in the range from 0 to $\pi/2\sqrt{3}$. Figure 4.13 shows the center and width of the bandgap as a function of lattice size and filling fraction.

The bandgap center, as in the previous cases, is an increasing function of the lattice constant and the filling fraction, that is, the bandgap is red shifted when the lattice constant and the

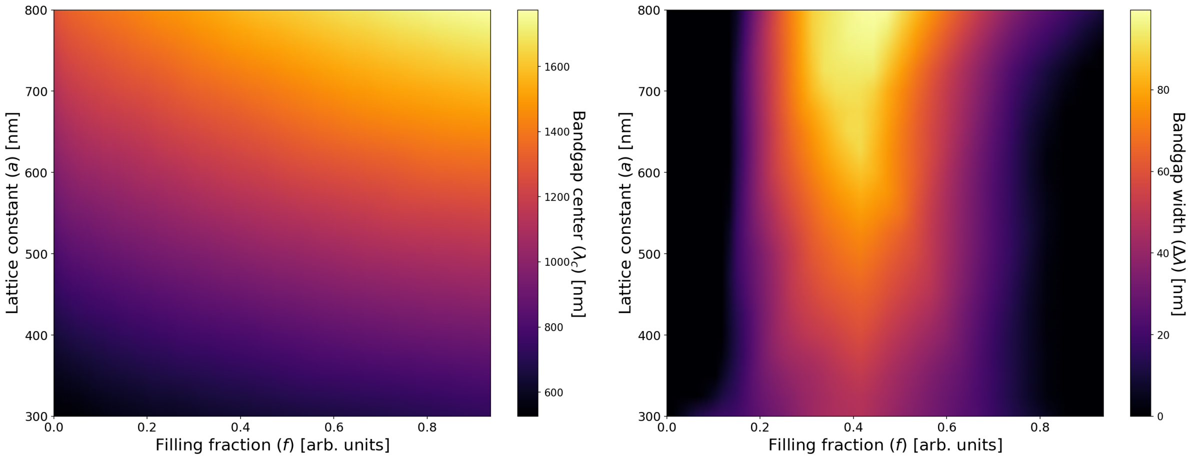

(a) Bandgap center.

(b) Bandgap width.

Figure 4.13: Bandgap properties for a dielectric-Au PhPl crystal with a triangular lattice and an elliptical base.

filling fraction are increased. On the other hand, a complete bandgap is produced when f is larger than 0.3 and less than 0.85, where the bandgap width reaches its maximum near $f = 0.44$ and then decreases to a minimum. Furthermore, the bandgap width is a monotonically increasing function of the lattice constant. For the wavelength interval used, the maximum width is $\Delta\lambda = 99.56$ nm.

This behavior of the bandgap properties is consistent with the results reported in references [6, 7]. In that case, the PhPl crystals consist of Au columns in a triangular array on a thin film of the same material, and it is experimentally verified that the bandgap broadens and is red-shifted when the filling fraction increases.

4.1.4 Rectangular lattice

In this case, the theoretical model was used to analyze the band structures of dielectric-Au and dielectric-Ag PhPl crystals in a rectangular lattice, with elliptical and rectangular bases. The interfaces are shown in Fig. 4.14 and, as in the previous cases, the white zones are the air-metal interface and the gray zones are the PMMA-metal interface.

Figure 4.15b shows the photonic band structure of a dielectric-Au PhPl in a rectangular lattice with a circular base, where this base is considered a particular case of an elliptical base. The lattice constant in the x-direction is $a_x = 300$ nm, in the y-direction is a $a_y = 480$ nm, and the diameter of the cross-section is $d = 235$ nm. Using the same parameters, the band structure of a dielectric-Ag PhPl crystal was calculated, as shown in Fig. 4.15a.

In both cases, there are two partial bandgaps in the fitting range, one on the $\Gamma{-}\mathrm{X}$ orientation and the other on the $\mathrm{Y} - \Gamma$ orientation. The former is centered at $\lambda_c = 747.09$ nm and has a width of $\Delta\lambda = 90.95$ nm, while the latter is centered at $\lambda_c = 1242.28.09$ nm and has a width

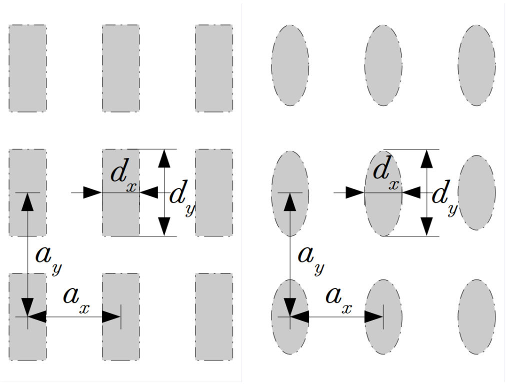

(a) Rectangular base. (b) Elliptical base.

Figure 4.14: Rectangular lattice with two bases differents.

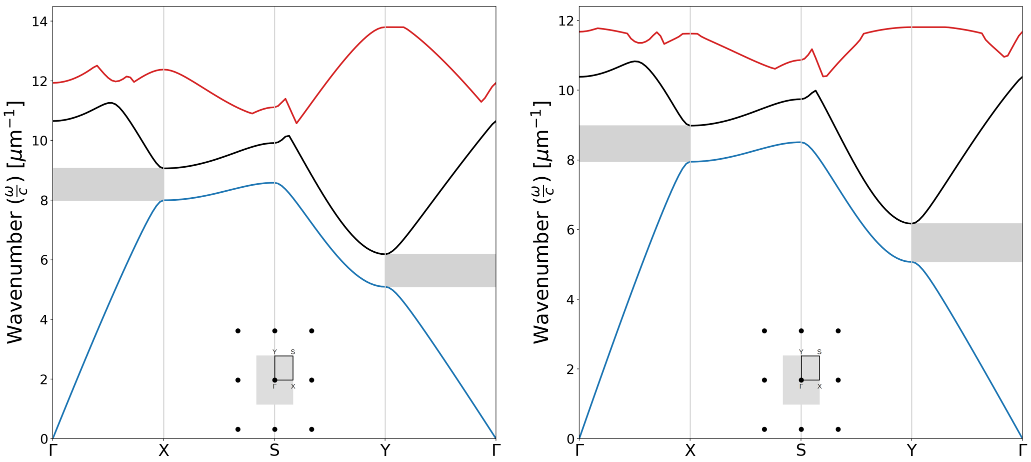

(a) Dielectric-Ag PhPl crystal band structure

(b) Dielectric-Au PhPl crystal band structure

Figure 4.15: Band structure of two different dielectric-metallic PhPl crystals with a rectangular lattice and an elliptical base.

of $\Delta\lambda = 222.11$ nm.

In addition, the first band of the band structure of both PhPl crystals is similar because the effective refractive indexes are similar in that frequency range. The above means that the dielectric-Au and dielectric-Ag PhPl crystals have almost the same optical response in that range of the electromagnetic spectrum. However, the third band presents significant differences, since the inverse of the effective refractive index has a wider fitting range. Besides, the dielectric-Ag PhPl crystal can operate over a wider frequency range.

On the other hand, as shown above, for a square lattice with a low contrast of dielectric constants (in particular ϵ_b/ϵ_a =2.2), complete bandgaps are not formed. However, using the theoretical model to analyze a rectangular lattice, and considering an analogous path to the square lattice, (in this case $\Gamma - \mathrm{X} - \mathrm{S} - \Gamma$), a complete bandgap can be found for some a_y/a_x ratios and filling fractions f.

Figure 4.16 shows the photonic bandgap structure of a rectangular PhPl crystal with $a_x =$ 300 nm, $a_y = 465$ nm and $d = 230$ nm. For these parameters, the center and width of the bandgap are $\lambda_c = 714.12$ nm and $\Delta\lambda = 36.49$ nm, respectively. With this lattice, it is possible to have a complete bandgap even with a small refractive index contrast, by considering a path $\Gamma - \mathrm{X} - \mathrm{S} - \Gamma$. With the same parameters, for a dielectric-Ag PhPl crystal, the bandgap is centered at $\lambda_c = 707.63$ nm and has a width $\Delta\lambda = 36.06$ nm.

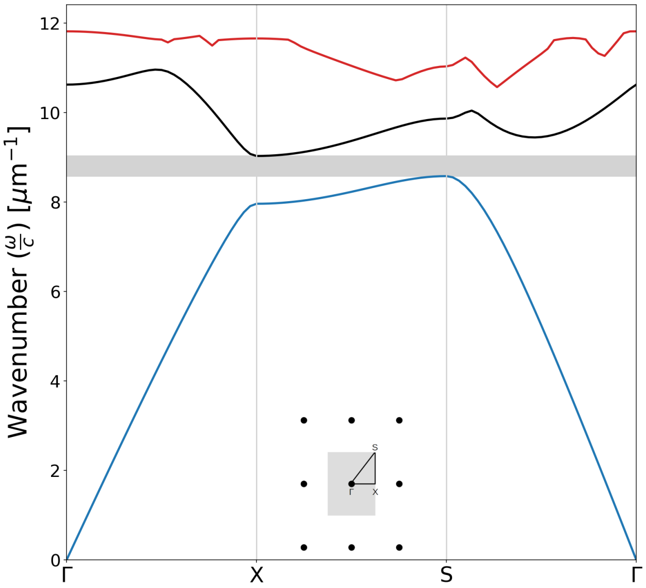

Figure 4.16: Band structure of a rectangular plasmonic crystal with $a_x = 300$ nm, $a_y = 465$ nm and $d = 230$ nm.

To get a clearer picture of bandgap formation, a heat map of bandgap width as a function of lattice side ratio $r_a = a_y/a_x$ and filling fraction f is shown in Fig. 4.17. This plot corresponds to a lattice constant of $a_x = 300$ nm, with a variation of the lattice constant a_y. This variation was between 20% and 180% of the lattice constant a_x.

From the heat map, it can be seen that the bandgap appears when the ratio $r_a = a_y/a_x$ is between 1.6 and 1.8. Furthermore, to have a complete bandgap, the filling fraction must have values between 0.1 and 0.6. In this particular case, the maximum width, $\Delta\lambda = 59.79$ nm, is obtained for $r_a = 1.5$ and $f = 0.33$.

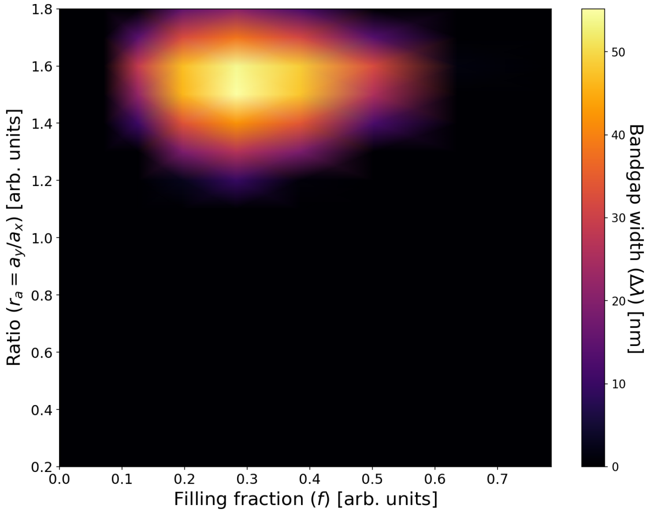

Figure 4.17: Bandgap width as a function of $r_a = a_y/a_x$ and f, for rectangular lattice with an elliptical base.

4.2 Machine learning algorithms

Several machine learning algorithms were used for forward design, i.e., predicting the optical response from the crystal parameters. In addition, these same algorithms were used for inverse design, that is, predicting the structural parameters for a target optical response. The algorithms used were linear and polynomial regression, k-nearest neighbors (KNN), decision trees and artificial neural networks (ANN).

The data set used to train the algorithms was built through the analytical model, where the optical properties of the PhPl crystal, that is, the center λ_c and the width $\Delta\lambda$, were calculated from the structural parameters of the crystal. These structural parameters were varied as reported in Table 4.1.

These parameters were chosen so that the center of the bandgap is consistent with the frequency range established for the fit of the inverse of the effective dielectric function. The parameters $f_x = dx/a$ and $f_y = dy/a$ are the filling fraction in the x and y directions, respectively, for the square and triangular lattice; and $f_x = d_x/a_x$, $f_y = d_y/a_y$ for the rectangular lattice.

In the rectangular lattice, the size a_y was varied from $1.2a_x$ to $1.8a_x$ for each a_x. This means that the size in the y-direction is larger than the size in the x-direction. These parameters were chosen because, in that range, a complete bandgap for the rectangular lattice arises in a shortened path ($\Gamma - \mathrm{X} - \mathrm{S} - \Gamma$).

To train the algorithms for forward design, the input data used were the crystal parameters a, d_x and d_y for square and triangular lattice, while for rectangular lattice the input data used were the crystal parameters a_x, a_y, d_x and d_y. For the three lattices, the output data or objective variable were the optical response of interest, that is, the bandgap center λ_c and

Crystal parameters		Lattice		
		Square	Triangular	Rectangular
a		200 - 700 nm	300 - 700 nm	-
a_x		-	-	200 - 700 nm
a_y		-	-	$1.2a_x$ - $1.8a_x$
f_x	Rectangular	0 - 1	0 - ($\sqrt{3}$ - 1)	0 - 1
	Elliptical	0 - 1	0 - 1	0 - 1
f_y	Rectangular	0 - 1	0 - ($\sqrt{3}$ - 1)	0 - 1
	Elliptical	0 - 1	0 - 1	0 - 1

Table 4.1: Parameters to generate data

bandgap width $\Delta\lambda$.

For the inverse design, the input data were the bandgap properties (optical response), λ_c and $\Delta\lambda$ for the three lattices. The output or target variables were the structural parameters, that is the lattice constant a and filling fraction f for the square and triangular lattices, and lattice constants a_x, a_y and filling fraction f for rectangular one.

The filling fraction f was chosen instead of the base sizes d_x and d_y because, with this parameter, the algorithms perform better in predicting structural features. Finally, to avoid redundant data, for the inverse design only square and circular bases were used for the square and triangular lattices, and elliptical bases for the rectangular lattice. This was done because a filling fraction can have several d_x and d_y values associated with it.

4.2.1 Square lattice

Linear and polynomial regression

For this crystal lattice, a data set with 16800 instances was used to train the model that predicts the optical response from the crystal parameters. The lattice constant a and the basis sizes d_x and d_y were used as input data, and the optical response λ_c and $\Delta\lambda$ were used as output data or target variables. The data set was splitted into 75% of the data to train the model and 25% to test or validate the model.

Polynomial regression from 1 to 15 degrees was used, as shown in Fig. 4.18a. The accuracy of the model in predicting the optical response as a function of a, d_x annd d_y is very similar in both the training and test data sets. As the model becomes more complex, that is, when the degree is higher, the accuracy is higher, close to 1.

In the case of linear regression, the accuracy of the train model is 0.8098 and the test is 0.8052. However, both accuracies increase rapidly and for a 4-degree polynomial, the accuracy

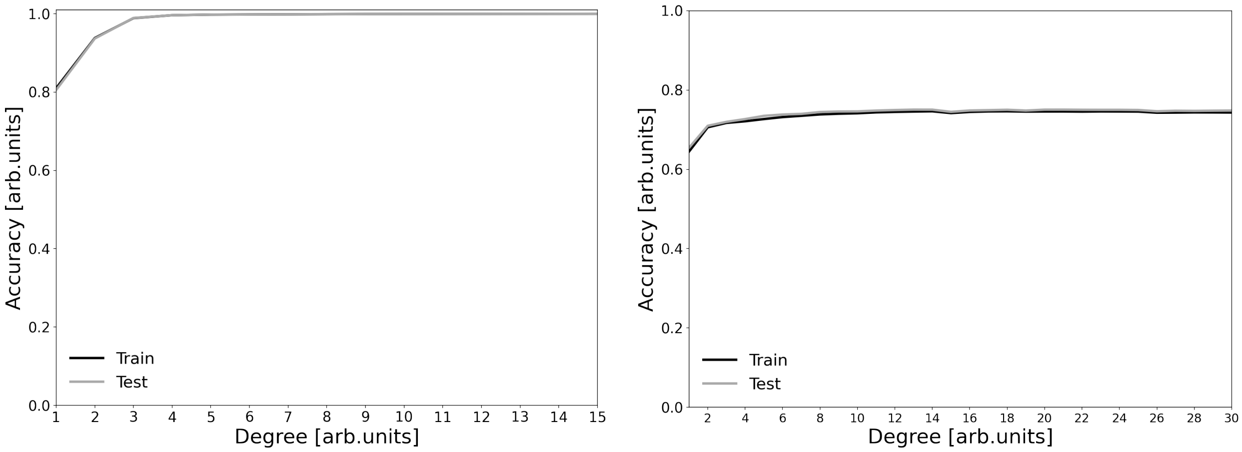

(a) Forward design

(b) Inverse design

Figure 4.18: Polynomial regression accuracy.

is up to 0.99. When a 6-degree polynomial is used for regression, the accuracy of the training set is 0.9982, while the accuracy of the test set is 0.9983. For higher degrees the accuracy increases, for example, for a polynomial of 15-degree, the test accuracy is 0.9998.

Thus, a polynomial regression of degree 4 is a suitable model for predicting optical response as a function of crystal parameters, but a higher degree will have higher accuracy for predicting optical response as a function of crystal parameters.

Concerning the inverse design, polynomial regression is not a suitable model for predicting structural parameters as a function of the optical response. For the regression, polynomials of degrees 1 to 30 were used and the accuracy of the training and test set was measured. Figure4.18b shows the training accuracy and as a function of degree. Both accuracies increase as the model becomes more complex, and reach their maximum for a model of degree 13, where the training and test accuracies are 0.7457 and 0.7505, respectively.

K-nearest neighbors

The K-nearest neighbors algorithm was used for the direct and the inverse designs, varying the number of nearest neighbors from 1 to 30. Figure 4.19a shows the accuracy from 1 to 15 nearest neighbors. For K=1, the training and test accuracy is 1 and 0.9782 respectively, suggesting that the model is overfitted. When K is increased, both training and testing accuracy increase to a maximum with 5 nearest neighbors for training accuracy and 4 nearest neighbors for testing accuracy. The accuracy with K=4 is 0.9984 for training and 0.9976 for testing.

Using the same algorithm, a model for the inverse design was trained, where the accuracy for the training and test is shown in Fig. 4.19b. As in the previous design, the model is overfitted for K=1, and when the number of nearest neighbors is increased, the test accuracy also increases, while the training accuracy decreases. The best performance obtained was for 30 nearest neighbors, where the accuracy for the training data set is 0.7722, and for the test

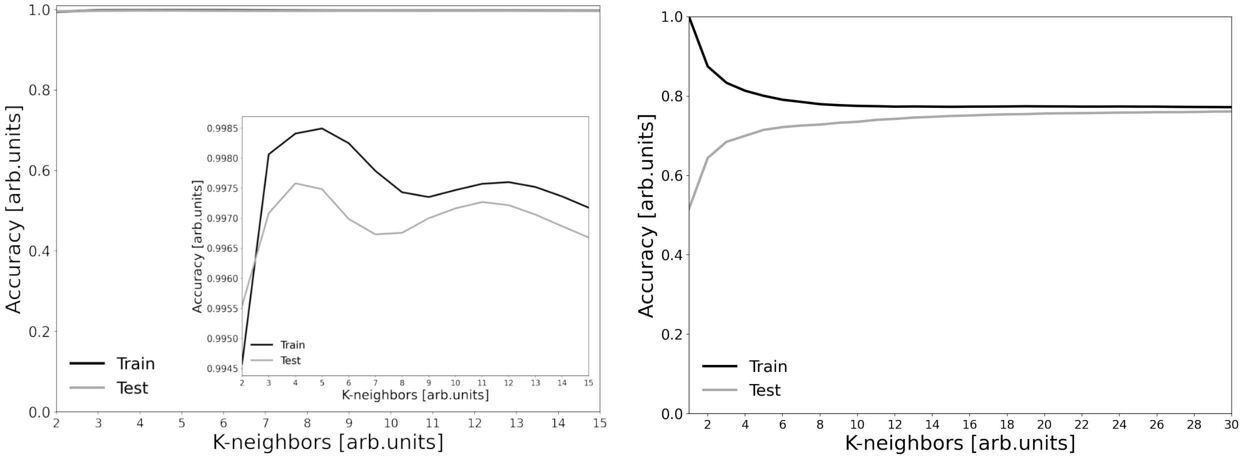

(a) Forward design.

(b) Inverse design

Figure 4.19: Accuracy of K-nearest neighbors algorithm as a funtion of nearest neighbor number.

data set is 0.7612.

Similar to polynomial regression, the best accuracy achieved with the studied parameters is up to 0.75, however, K-nearest neighbors is not the best model to achieve predictions with high accuracy for inverse design.

Decision trees

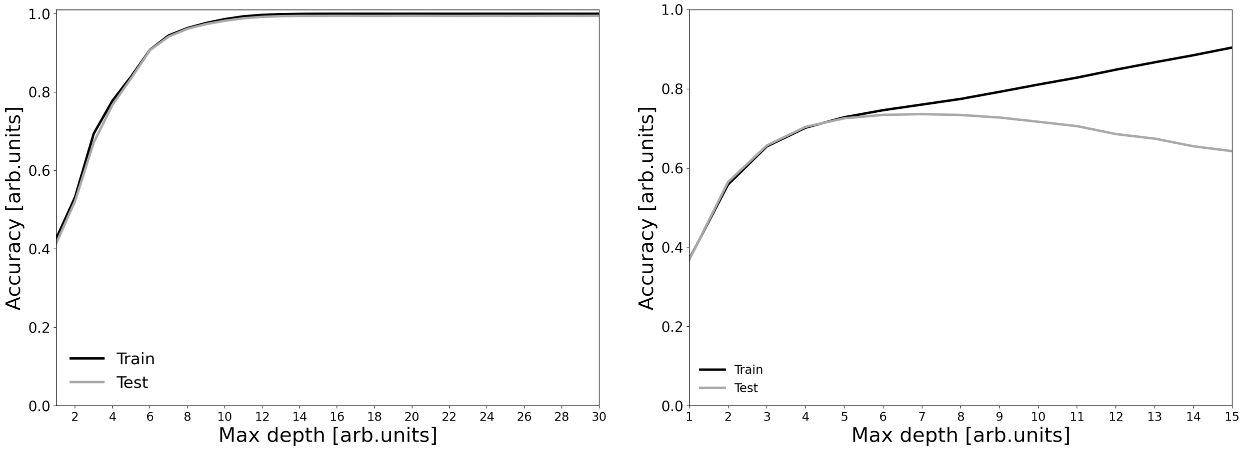

(a) Forward design.

(b) Inverse design.

Figure 4.20: Accuracy of decision tree algorithm as a funtion of max depth number.

The decision tree algorithm was used to have a maximum depth from 1 to 30. As shown in Fig. 4.20a, for the forward design, the accuracy increases from 0.4270 and 0.4151 in the training and test data sets, when the maximum depth is 1, to reach accuracies above 0.96 when the maximum depth is 8. For a maximum depth equal to 15, the accuracy of the training and test data is 0.9999 and 0.9944, respectively.

In the case of the inverse design, the maximum depth used was from 1 to 15, since from a maximum depth of 8 the model is overfitted. The test accuracy increases up to a maximum at the maximum depth equal to 7 and then decreases, while the training accuracy increases with increasing maximum depth.

The best performance for generalizing occurs when the maximum depth equals 7, for which the training accuracy is 0.7605 while the testing accuracy is 0.7363. As in the previous algorithms, the accuracy for predicting the structural parameters for a target optical response is less than 0.8.

Table 4.2 shows the results of the machine learning algorithms for the square lattice. The accuracy indicated in the table is the best performance of each algorithm in both the direct and inverse design. All three algorithms used are adequate for predicting the optical response as a function of crystal parameters, but fail to predict with high accuracy the structural parameters for a target optical response.

Table 4.2: Machine learning algorithms results for square lattice

	Forward design		Inverse design	
Algorithm	Train accuracy	Test accuracy	Train accuracy	Test accuracy
Polynomial regression	0.9982	0.9983	0.7457	0.7505
K-nearest neighbors	0.9984	0.9976	0.7722	0.7612
Decision tree	0.9999	0.9944	0.7605	0.7363

4.2.2 Triangular lattice

Linear and polynomial regression

For the triangular lattice, the data set consists of 12486 instances to predict the optical response from the crystal parameters. As in the previous lattice, the input parameters are the lattice constant a, and the base sizes d_x and d_y, while the output variables are the optical response λ_c and $\Delta\lambda$. Again, the data set was splitted into 75% of the data to train the model and 25% to test or validate the model.

For polynomial regression, the training data set was fitted using degrees from 1 to 15, as shown in Fig. 4.21a. The accuracy of the prediction of the optical response as a function of a, d_x and d_y increases as the degree of the polynomial increases, and the accuracy of the training and test data sets is very similar. Also, as in the previous case, for a more complex model, the accuracy increases, approaching 1.

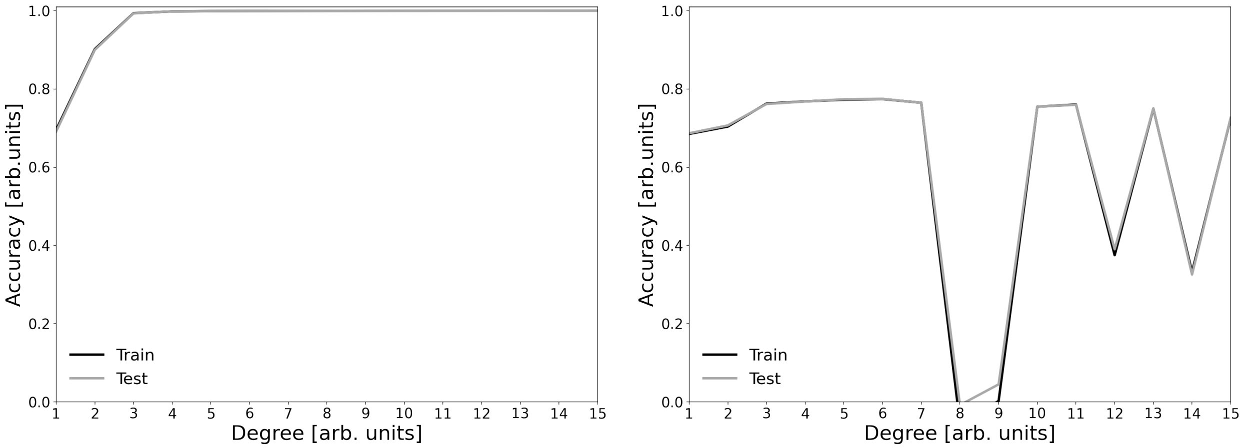

(a) Forward design (b) Inverse design

Figure 4.21: Polynomial regression accuracy.

In this case, using linear regression, the train accuracy is 0.6956 and the test accuracy is 0.6914. For higher degrees the accuracy increases rapidly, for example, for a 2-degree polynomial the accuracy is about 0.90 and for a 3-degree polynomial, the accuracy is up to 0.99. The accuracy of 5-degree polynomial regression algorithm is 0.9992, while the test accuracy is 0.9993. The polynomial regression algorithm is a suitable model for predicting the optical response as a function of crystal parameters when the polynomial degree is greater than 4.

Figure 4.21b shows the train and test accuracy for predicting structural parameters as a function of the optical response. Polynomials of degrees 1 to 15 were used to fit the data set where it can be seen that the accuracy is less than 0.8 for both train and test. The best accuracy is 0.7712 for train and 0.7715 for test, when using a polynomial of degree 7. For the range of degrees used, polynomial regression is not the best model for predicting structural features as a function of the optical response.

K-nearest neighbors

As for the square lattice, the K-nearest neighbors algorithm was implemented for the direct and inverse design, using a range of nearest neighbors from 1 to 30. Figure 4.22a shows the accuracy of the forward design as a function of nearest neighbors. When K=1, the training and test accuracies is 1 and 0.9968 respectively, although both values are similar, the model is overfitted. As K increases, the training accuracy decreases, while the test accuracy tends to increase up to K=6. The minimum difference between train and test accuracy is for 6 nearest neighbors, where train accuracy is 0.9983 and test accuracy is 0.9981.

With the same parameters, but for the inverse design, the training and test accuracies are shown in Fig. 4.22b. The model is overfitted for K=1, since the training accuracy is 1.0 and

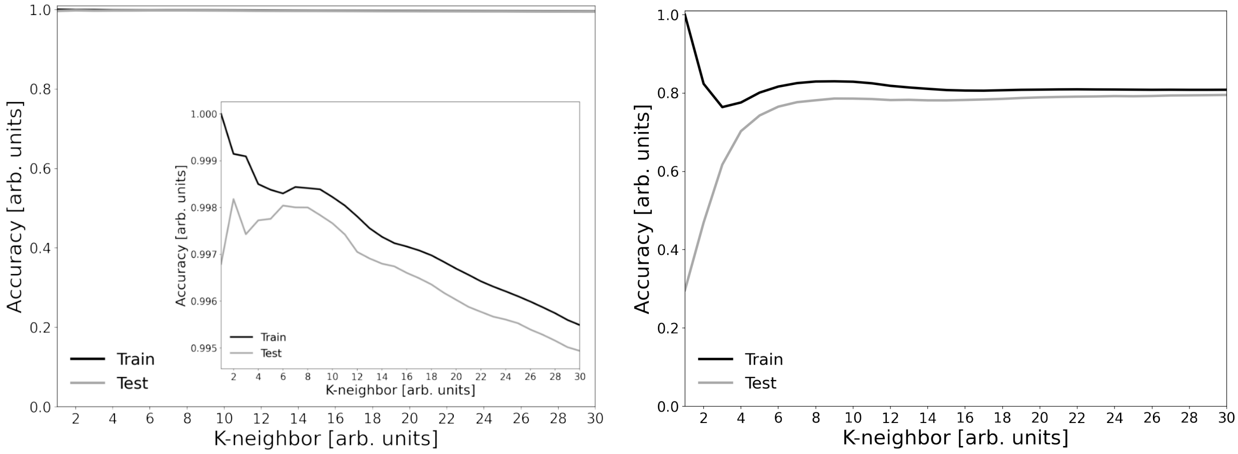

(a) Forward design.

(b) Inverse design

Figure 4.22: Accuracy of K-nearest neighbors algorithm as a funtion of nearest neighbor number.

the test accuracy is 0.3747; however, the training accuracy tends to decrease as K increases, and the test accuracy increases as K increases. For an algorithm with 13 nearest neighbors, the training and test accuracies are 0.8317 and 0.8017, respectively, and both do not exhibit significant changes as K increases.

Decision trees

Concerning the decision tree algorithm, the maximum depth range used was from 1 to 30. For the forward design, the accuracy increases as the maximum depth increases, reaching values close to 1 for a maximum depth up to 11, as shown in Fig. 4.23a. The accuracy of the training and test data set for a maximum depth equal to 15 are 0.9999 and 0.9836, respectively.

For the inverse design, the train accuracy increases as the maximum depth increases, as shown in Fig. 4.23b, however, the test accuracy reaches a maximum at the maximum depth equal to 7 and then decreases. The optimal maximum depth parameter is 7 when the training and test accuracies are 0.8402 and 0.8239, respectively. When this parameter is larger, the model is overfitted.

As in the previous cases, this algorithm is accurate in predicting the optical response as a function of the crystalline parameters. However, for predicting structural features for a target optical response, it is not the optimal model.

Artificial neural networks

Since complete bandgaps are produced for this network, a fourth algorithm, artificial neural networks (ANNs), was used. Several architectures were tested, and the best performance was obtained with five hidden layers in which, the first layer has 100 neurons, the second 200, the

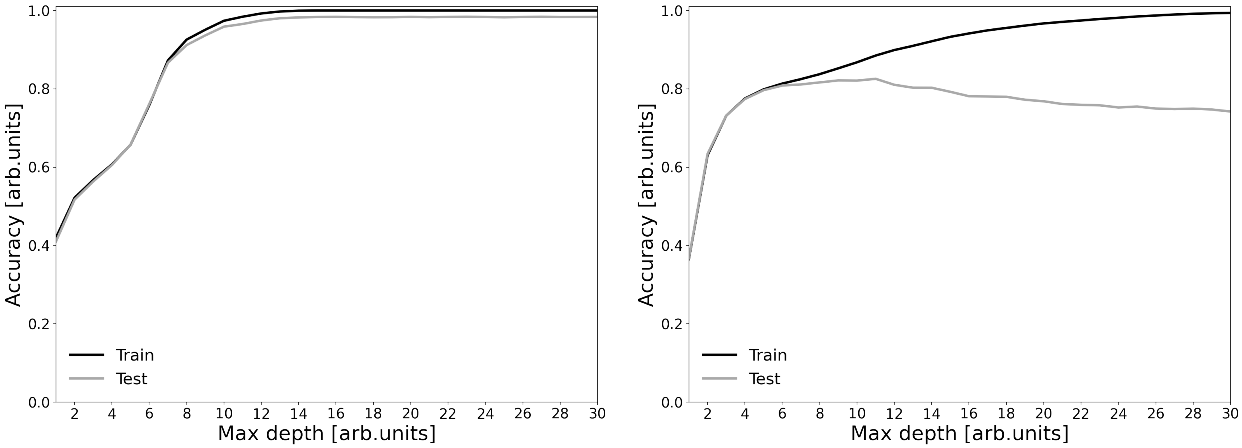

(a) Forward design. (b) Inverse design.

Figure 4.23: Accuracy of decision tree algorithm as a funtion of max depth number.

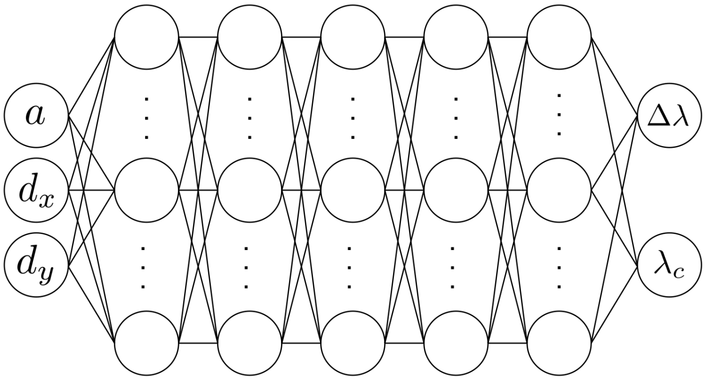

Figure 4.24: ANN architecture used for forward design.

third 300, the fourth 200, and the fifth 100 neurons. A diagram of the architecture is shown in Fig. 4.24.

Also, several hyperparameters were tested, where the optimal performance was obtained with 200 epochs, «adam optimizer» with a «learning rate» of 0.004, guillemotleft mean squared error» was used as loss function, «accuracy» was for metrics, and the activation function used was ReLU. In Fig. 4.25a, the loss function as epochs function is shown. As it can be seen, the loss function decays rapidly, and for a few epochs is near to zero. So, a high accuracy is obtained for a few epochs, as it can be seen in 4.25b.

For the inverse design, several ANN architectures and hyperparameters were tested. For this lattice, the best performance was obtained with 15 hidden layers of 500 neurons each. The optical response λ_c and $\Delta\lambda$ were used as input data, and the structural parameters a and f as output data. The architecture diagram is shown in Fig. 4.26.

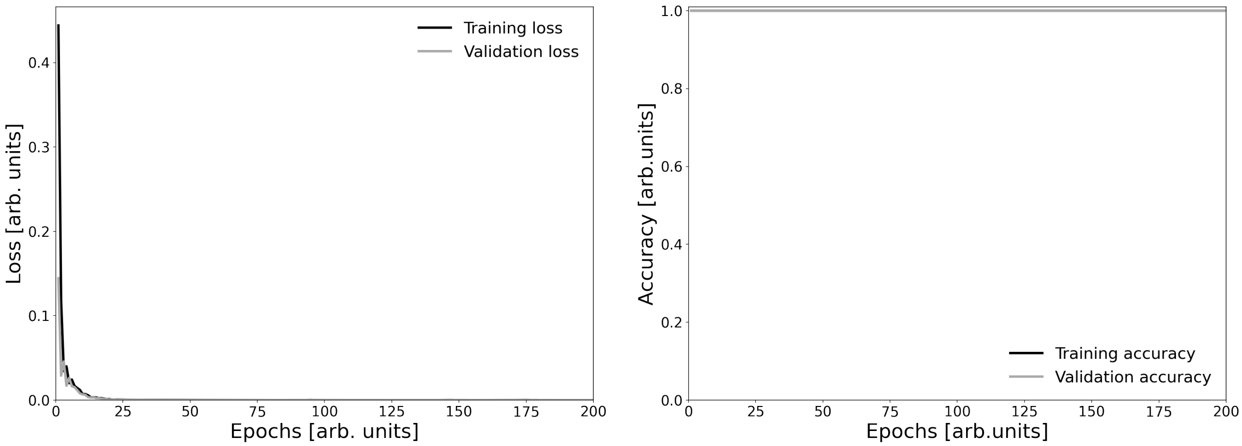

(a) Loss function. (b) Accuracy

Figure 4.25: Artificial neural networks algorithms performance for forward design.

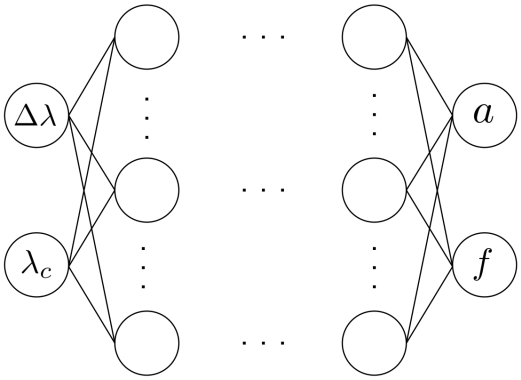

Figure 4.26: ANN architecture used for inverse design.

The optimal performance was obtained with 200 epochs, an adam optimizer with a learning rate of 0.003, as loss function the mean square error was used, as metric the «cosine similarity» was used, and as activation function the ReLU function. The loss function and accuracy are shown in Fig. 4.27 as a function of the number of epochs.

In Fig. 4.27a, it is possible to see the rapid decay of the loss function, and for 100 epochs the loss function is less than 0.01. Concerning the accuracy, it increases as the number of epochs increases, reaching a cosine similarity of 0.9853 for the training accuracy, and 0.9848 for the test or validation accuracy, as shown in Fig. 4.27b.

Table 4.3 shows the performance results of the machine learning algorithms for the triangular lattice. As in the previous lattice, for the accuracy reported in the table, the algorithms are more accurate for the direct design than in the inverse design

ANN, like polynomial regression, K-nearest neighbors, and decision tree, predict the optical

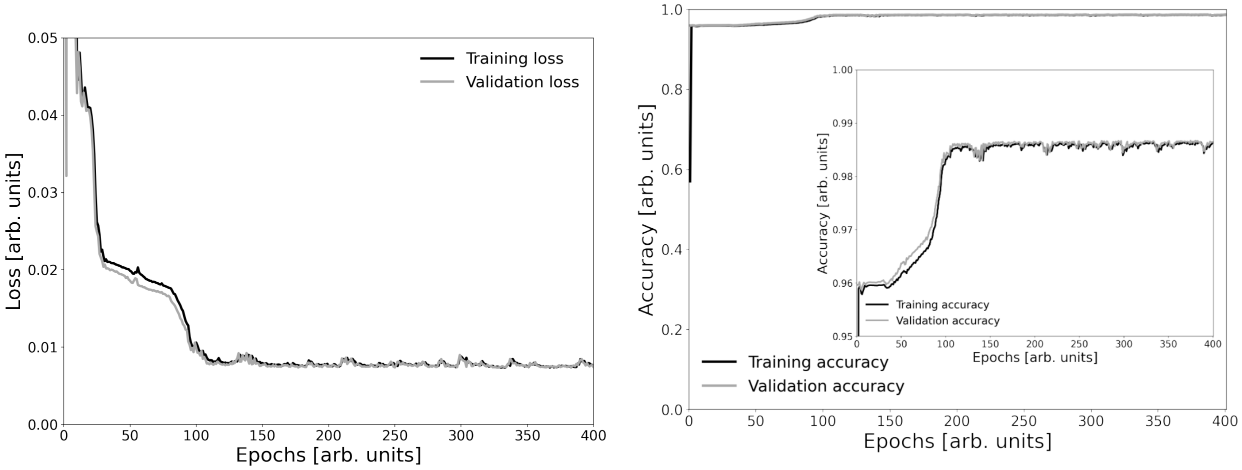

(a) Loss function.

(b) Accuracy

Figure 4.27: Artificial neural networks algorithms performance for inverse design.

Table 4.3: Machine learning algorithms results for triangular lattice

	Forward design		Inverse design	
Algorithm	Train accuracy	Test accuracy	Train accuracy	Test accuracy
Polynomial regression	0.9992	0.9993	0.7712	0.7715
K-nearest neighbors	0.9983	0.9981	0.8317	0.8017
Decision tree	0.9999	0.9836	0.8402	0.8239
ANN	1	1	0.9853	0.9848

response as crystal parameters with high accuracy, close to 1. However, unlike the other algorithms, ANN predicts the structural parameters for a target optical response with high accuracy, which makes this algorithm optimal for the inverse design tasks for this particular photonic system.

4.2.3 Rectangular lattice

The dataset used to train the forward design model has 10416 instances, of which 75% were used in the training dataset and 25% in the test or validation dataset. In this case, the input data consist of the lattice constants a_x, a_y and the base sizes d_x and d_y, while the optical response λ_c and $\Delta\lambda$ were used as output data. On the other hand, for the inverse design model, the dataset has 262600 instances, where 90% was used as a training dataset and 10% as test dataset. As input data, the optical response λ_c and $\Delta\lambda$ were used, while the structural parameters a_x, a_y

and f are the output data.

Linear and polynomial regression

As in the previous lattices, several algorithms were used for the forward and inverse design. Starting with polynomial regression with the same degree range, from 1 to 15, the accuracy is shown in Fig. 4.28a

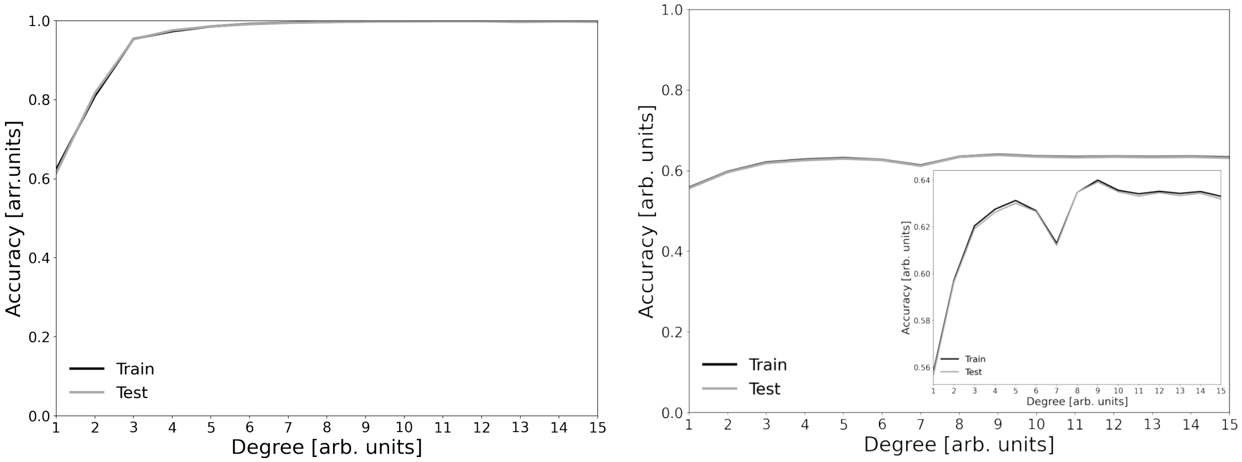

(a) Forward design

(b) Inverse design

Figure 4.28: Polynomial regression accuracy.

For linear regression, the train accuracy is 0.6223 and the test accuracy is 0.6141. For a higher polynomial degree, the accuracy in predicting the optical response increases, reaching an accuracy of 0.99 for a polynomial of degree 6. As it can be seen, the model has a high accuracy for a polynomial regression of degree 12, where the values are 0.9993 for the training set and 0.9986 for the test set.

As for the inverse design, both the train and test accuracies are below 0.64 for the degree range used, as shown in Fig. 4.28b. The highest accuracy is obtained when the grade is 14, where it is 0.6390 for the train data set and 0.6375 for the test data set. From both results, it can be inferred that polynomial regression is a suitable model for predicting the optical response as a function of crystal parameters, but it is not the most suitable for predicting structural features as a function of the optical response.

K-nearest neighbors

As in the previous cases, the k-nearest neighbor algorithm was used in a range from 1 to 30 nearest neighbors.

Figure 4.29a shows the accuracy as a function of the number of nearest neighbors. For K=1, the training and testing accuracies are 1 and 0.8261 respectively. The model reaches its optimal

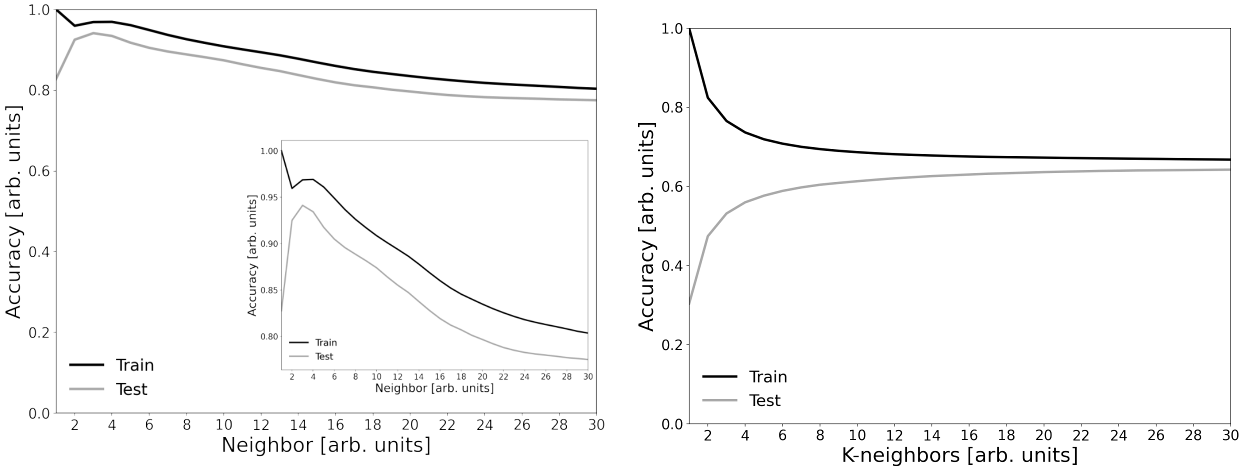

(a) Forward design.

(b) Inverse design

Figure 4.29: Accuracy of K-nearest neighbors algorithm as a funtion of nearest neighbor number.

generalization with 3 nearest neighbors, where the training accuracy is 0.9688 and the testing accuracy is 0.9430, and, after that, when increasing K, both training and testing accuracy also decrease.

With the same range of nearest neighbors, the accuracy of the inverse design is shown in 4.29b. As in the forward design, the model is overfitted for K=1, and when the number of nearest neighbors increases, the train accuracy decreases, while the test accuracy increases. In this case, the best performance in the evaluated range is obtained for 30 nearest neighbors, where the accuracy for the training data set is 0.6947, and for the test data set is 0.6702.

Decision trees

Figure 4.30a shows the accuracy obtained for the forward design using the decision tree algorithm. The accuracy increases from 0.4771 and 0.4619, for the training and test, when the maximum depth is 1, to values above 0.96 when the maximum depth is 20. The training and test accuracies reach their maximum values, 0.9679, when the maximum depth is 23.

With respect to the inverse design, the train accuracy increases as the maximum depth parameter does, reaching an accuracy of 0.8972 when the maximum depth equals 30, however, at this point the model is overfitted since the test accuracy is 0.4412. As for the test accuracy, it increases until it reaches a maximum value of 0.6589 when the maximum depth is equal to 10, and then decreases monotonically.

Artificial neural networks

For the forward design, the architecture was the same as used for the triangular lattice: five hidden layers with 100, 200, 300, 200, and 100 neurons respectively, as shown in Fig. 4.24.

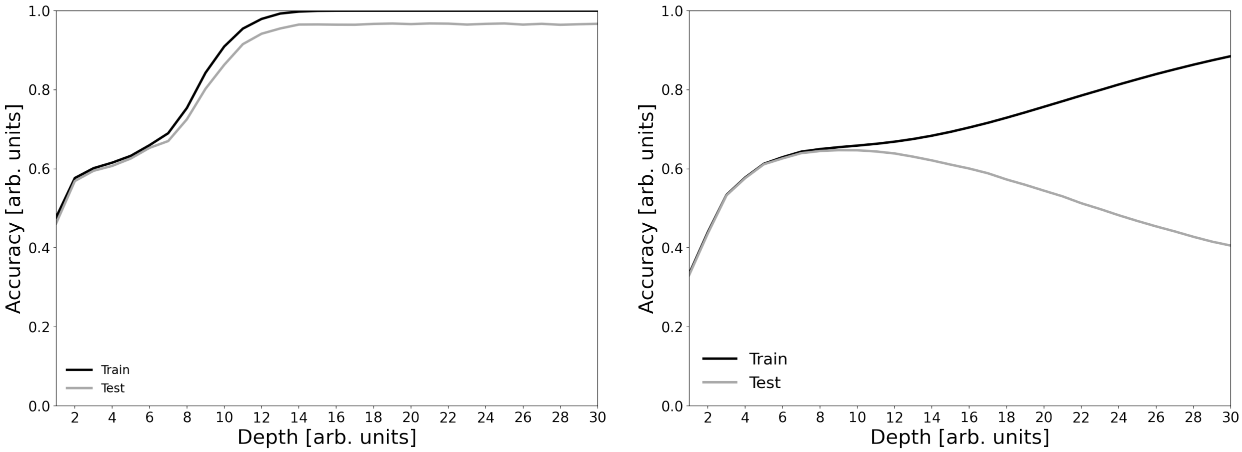

(a) Forward design.

(b) Inverse design.

Figure 4.30: Accuracy of decision tree algorithm as a funtion of max depth number.

From the search of the optimal parameters and hyperparameters, the optimal performance was obtained with 200 epochs, adam optimizer with a learning rate of 0.009, as a loss function the mean square error was used, the metric used precision, and the activation function was used ReLU.

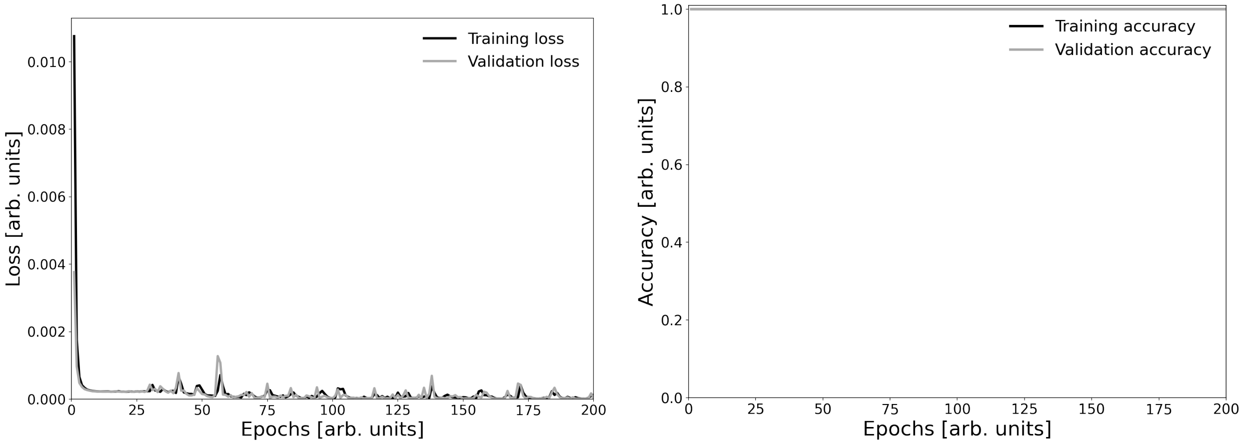

(a) Loss function.

(b) Accuracy

Figure 4.31: Artificial neural networks algorithms performance for forward design.

Figure 4.31a shows the loss function as a function of epochs, where it can be seen how the function decays rapidly tending to zero. For the test accuracy, it quickly reaches a value of 1, giving a high accuracy with few epochs, as shown in Fig.4.31b.

On the other hand, the architecture used for the inverse design is shown in 4.32. This ANN

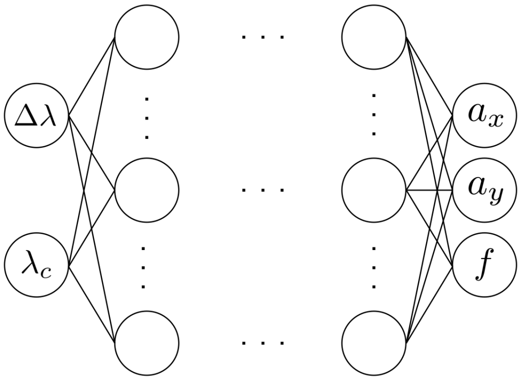

Figure 4.32: ANN architecture used for inverse design.

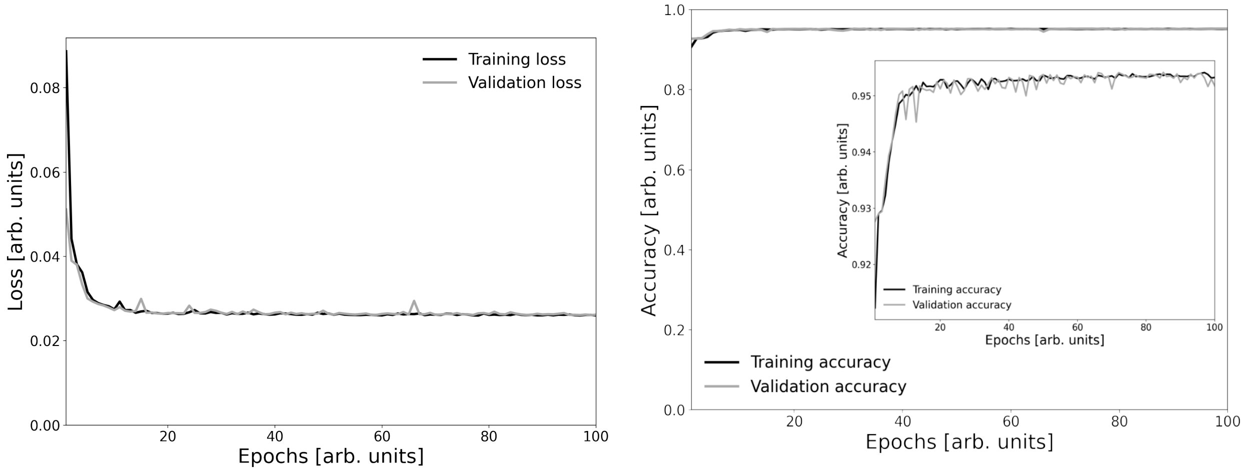

(a) Loss function.

(b) Accuracy

Figure 4.33: Artificial neural networks algorithms performance for inverse design.

has 15 hidden layers with 500 neurons each, the number of epochs used was 100, the optimizer was adam with a learning rate of 0.0015, the loss function was mean squared error, cosine similarity was used as metric, and the ReLU function as activation function.

As it can be seen in Fig. 4.33a, the loss function decreases rapidly as a function of the number of epochs, stabilizing near the value 0.025 for both training and test accuracies. On the other hand, the accuracy increases as the epochs increase, reaching a value of 0.9546 for the training accuracy and 0.9540 for the test accuracy.

Table 4.4 shows the results of the machine learning algorithms for the rectangular lattice. The accuracy indicated in the table is the best performance of each algorithm, both in the direct and inverse designs.

In summary, the algorithms used for all lattices can predict, with an accuracy better than

Table 4.4: Machine learning algorithms results for rectangular lattice

	Forward design		Inverse design	
Algorithm	Train accuracy	Test accuracy	Train accuracy	Test accuracy
Polynomial regression	0.9993	0.9986	0.6390	0.6375
K-nearest neighbors	0.9668	0.9430	0.6947	0.6702
Decision tree	1	0.9679	0.6713	0.6589
ANN	1	1	0.9546	0.9540

0.9, the optical response from the PhPl crystal characteristics. In other words, all algorithms used for forward design are suitable models for generalizing predictions from the data used for training. However, some perform better than others, where the accuracy is better than 0.99.

On the other hand, only ANNs adequately predict, with an accuracy better than 0.95, the structural features as a function of the optical response. From the results, ANNs are the appropriate model to perform the inverse design of these studied photonic-plasmonic systems. In general, machine learning algorithms can be a very useful tool in the design of photonic devices, both to optimize the theoretical study and the fabrication process.

4.3 Hybrid photonic-plasmonic crystals design

The algorithms were tested using various crystal parameters and compared with the theoretical model. In the case of the forward design, the input data are the lattice constant a and the base sizes d_x and d_y for the square and triangular lattices. In the case of the rectangular lattice, the input data are the lattice constants a_x and a_y and the base sizes d_x and d_y. For all lattices, the optical properties λ_c and $\Delta\lambda$ were used as output variables.

For the inverse design, the parameters λ_c and $\Delta\lambda$ were used as input for the triangular and rectangular lattices. For the triangular lattice, the output data were the lattice constant a and the filling fraction f, while the output data for the rectangular lattice were the lattice constants a_x and a_y and the filling fraction f. Finally, from the filling fraction, the base sizes d_x and d_y were calculated.

4.3.1 Square lattice

The algorithms results were tested using a lattice constant $a = 300$, and base sizes $d_x = 100$ nm and $d_y = 150$ nm. With this parameters the partial bandgap in $\Gamma - \mathrm{X}$ orientation is centered at $\lambda_c = 674.446$ nm and has a width of $\Delta\lambda = 82.113$ nm. The results obtained with machine learning algorithms are shown in table 4.5. As it can be seen, the machine learning algorithms predict correctly the optical properties as a function of crystal parameters, where the minimum discrepancy among results is obtained with k-nearest neighbors, for both bandgap center and

Table 4.5: Results comparison between theoretical model and machine learning algorithms for square lattice and forward design.

Bandgap properties	Theoretical model	Polynomial regression 12 degree	K-nearest neighbors 4 nearest neighbors	Decision tree max depth = 15
Center (λ_c) [nm]	674.446	672.876	673.241	676.822
Porcentual error	-	0.233%	0.179%	1.397%
Width ($\Delta\lambda$) [nm]	82.113	84.104	80.503	84.930
Porcentual error	-	2.424%	1.961%	3.431%

bandgap width. Quantitatively, this can be verified from the percent errors, among which the smallest is for the K-nearest neighbors algorithm. However, for the rest, the percent errors do not reach 4

4.3.2 Triangular lattice

For triangular lattices, the optical response was calculated using the same crystal parameters: a lattice constant $a = 300$ nm and a base with major axis $d_x = 100$ nm and minor axis $d_y = 150$ nm. The analytical model with these parameters predicts a bandgap centered at 588.724 nm and with a width of 25.198 nm. The prediction and comparison of the machine learning algorithms are in table 4.6. As it can be seen, the prediction of the optical response for all the algorithms is close to the calculations using the analytical model, as shown by the percent errors. Of the four algorithms used, the lowest percent errors were obtained for the decision tree and ANN algorithms., which is consistent with the accuracy reported above.

Table 4.6: Results comparison between theoretical model and machine learning algorithms for triangular lattice and forward design.

Bandgap properties	Theoretical model	Regression 5 degree polynomial	K-NN 2 NN	Decision tree max depth = 15	ANN
Center (λ_c) [nm]	588.724	587.060	595.989	588.613	586.659
Percent error	-	0.283%	1.234%	0.019%	0.351%
Width ($\Delta\lambda$) [nm]	25.198	27.745	24.181	25.130	24.846
Percent error	-	10.108%	4.036%	0.270%	1.397%

On the other hand, in table (4.7) are the inverse design results. The structural parameters predicted correspond to an target bandgap centered at $\lambda_c = 633$ nm and with a width $\Delta\lambda = 20$ nm. With these predicted parameters, the optical response was calculated using the analytical model. The lattice constant a predicted is within the range 322.365 to 343.333 nm, while the base size is within 124.007 and 155.267 nm.

Table 4.7: Predicted parameters and their respective optical response calculated with the analytical model.

Algorithm	Structural parameters		Calculated optical response	
	(a) [nm]	d [nm]	(λ_c) [nm]	$(\Delta\lambda)$ [nm]
Regression 7 degree polynomial	322.365	155.267	637.423	42.868
Percent error	-	-	0.699%	114.34%
K-NN K = 30	337.833	128.130	635.456	22.428
Percent error	-	-	0.388%	10%
Decision Tree max depth = 10	343.333	124.007	639.395	16.953
Percent error	-	-	1.010%	15.235%
ANN	329.968	126.149	620.884	19.505
Percent error	-	-	1.914%	2.475%

The correspondig bandgap properties are in the range 620.884 to 639.395 nm for bandgap center, and 16.953 to 42.868 nm for bandgap width. As expected, the bandgap width is larger for a larger base size, as observed with the polynomial regression and decision tree predictions. In addition, the most accurate predictions for bandgap width were obtained using K-nearest neighbors, decision tree and ANN, where the base diameter is between 124.007 and 128.130 nm. However, ANNs have, in general, a better performance, since their percent errors are 1.914% for the center and 2.475% for the width of the bandgap.

To corroborate the results obtained from the machine learning results and the theoretical model, numerical simulations were performed as shown in Fig. 4.35. Based on the machine learning algorithm predictions and theoretical model calculations, the simulated system is a triangular lattice with lattice constant $a = 330$ nm and a circular PMMA base of diameter $d = 130$ nm on a Au thin film, so, this way, the system has two interfaces, an air-Au interface and a PMMA-Au interface. Using these parameters, the analytical model calculates a bandgap centered at $\lambda_c = 627.184$, with a width of $\Delta\lambda = 26.439$ nm. The band structure is shown in Fig. 4.34.

Figure 4.35a shows the SPPs incidence on a PhPl crystal in $\Gamma - \mathrm{M}$ orientation, while the Fig. 4.35b shows the SPPs incidence on $\Gamma - \mathrm{K}$ crystal orientation. In both configurations the SPPs does not propagate deeply in the PhPl crystal, but they are reflected and interfere with the incident SPPs.

The above can be seen clearly in Fig. 4.36, where the SPPs propagating in free space are compared with SPP propagating in PhPl crystal. The SPPs in free space decay exponentially, as shown by dashed line, while the SPPs in PhPl crystal are attenuated, as show by the solid

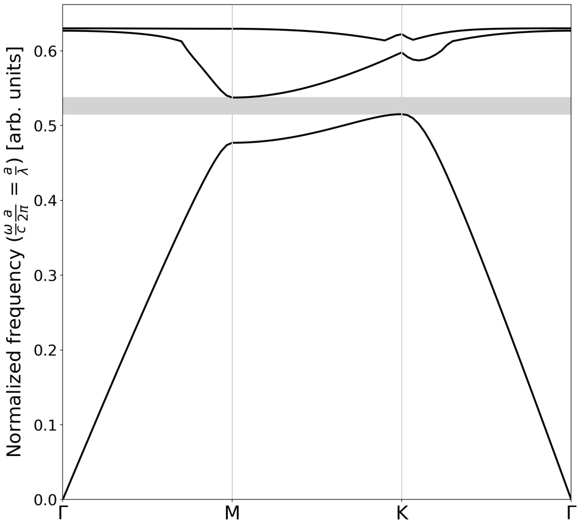

Figure 4.34: Band structure of a triangular lattice with a circular base. This band structure corresponds to a lattice constant $a = 330$ nm and diameter base $d = d_x = d_y = 130$ nm.

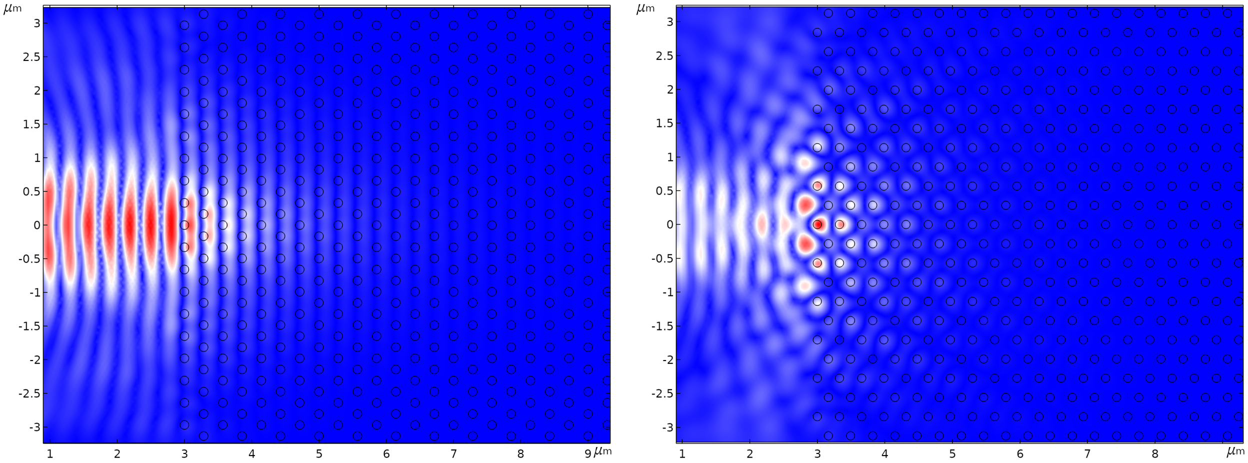

(a) $\Gamma - \mathrm{M}$ orientation.

(b) $\Gamma - \mathrm{K}$ orientation

Figure 4.35: Numerical simulation.

line. In this case, it arises an interference pattern due multiple reflections in the crystal.

Experimentally it is not straightforward to measure the transmittance through the PhPl crystal, however, an indirect way to quantify such quantity is through the optical signal that passes through it. This was done by implementing numerical simulations of the physical systems and the profile of the electric field along the y-axis was recorded at specific points on the x-axis for different wavelengths. That profile is compared with the profile of the SPP electric field propagating freely.

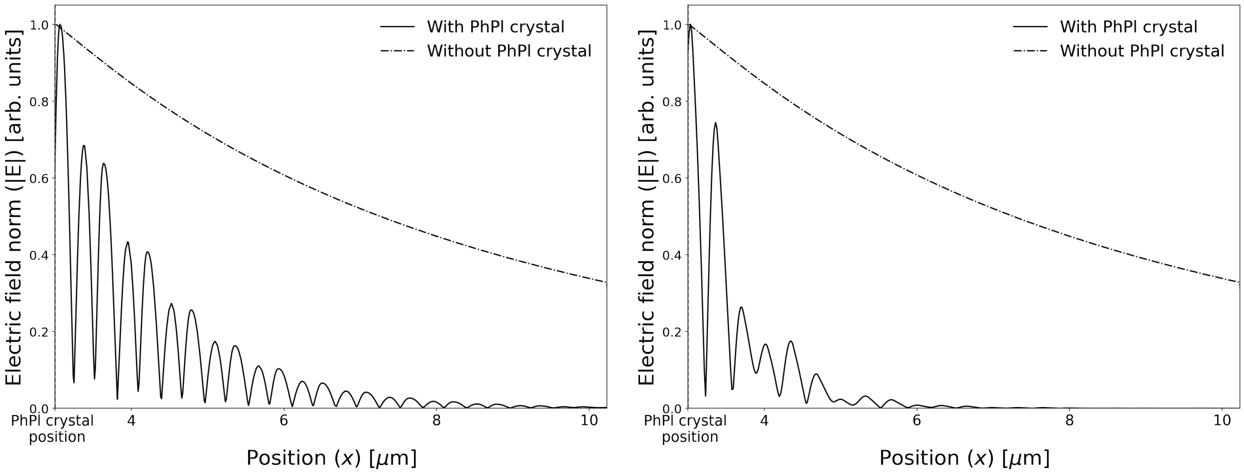

(a) $\Gamma - \mathrm{M}$ orientation.

(b) $\Gamma - \mathrm{K}$ orientation

Figure 4.36: SPPs intensity in free space and PhPl crystal.

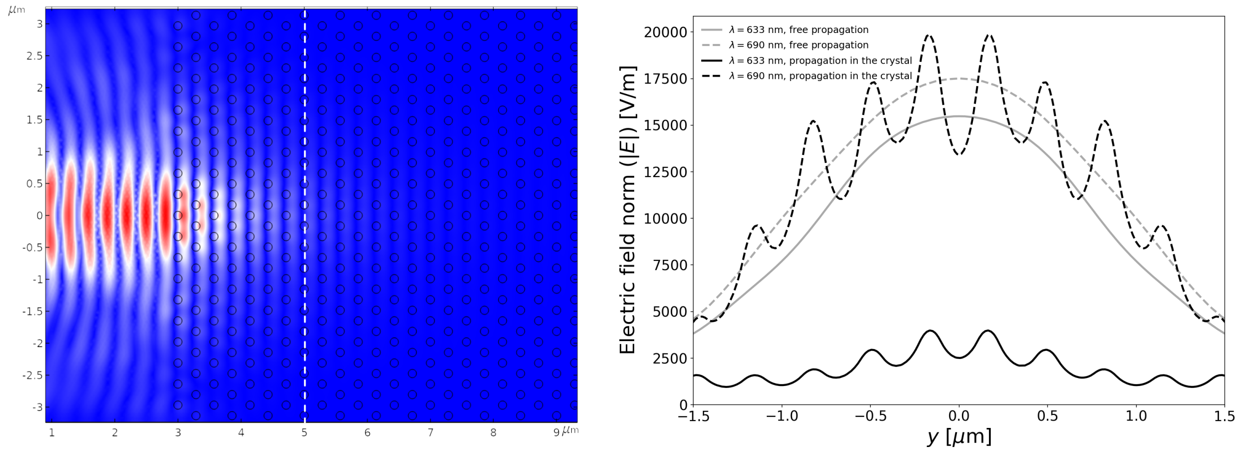

(a) $\Gamma - \mathrm{M}$ orientation with a cutline at $x = 5$ μm.

(b) Electric field profile

Figure 4.37: Electric field profile along y-axis at $x = 5$ μm.

As example, Fig. 4.37 shows the numerical simulation of the above system in which the intensity profile along the y-axis at $x = 5$ was recorded. As can be seen in the Fig. 4.37b, the electric field attenuates markedly for the wavelength within the bandgap ($\lambda = 633$ nm, solid curves), while for wavelength outside the bandgap ($\lambda = 690$ nm, dashed curves), the electric field magnitude undergoes slight variations.

In the same way, the figure shows the electric field profile at $x = 5$ μm for the G $-$ K orientation. As for the previous orientation, the electric field attenuates when the SPP frequency is within the bandgap. As expected, for frequencies outside the bandgap, the electric

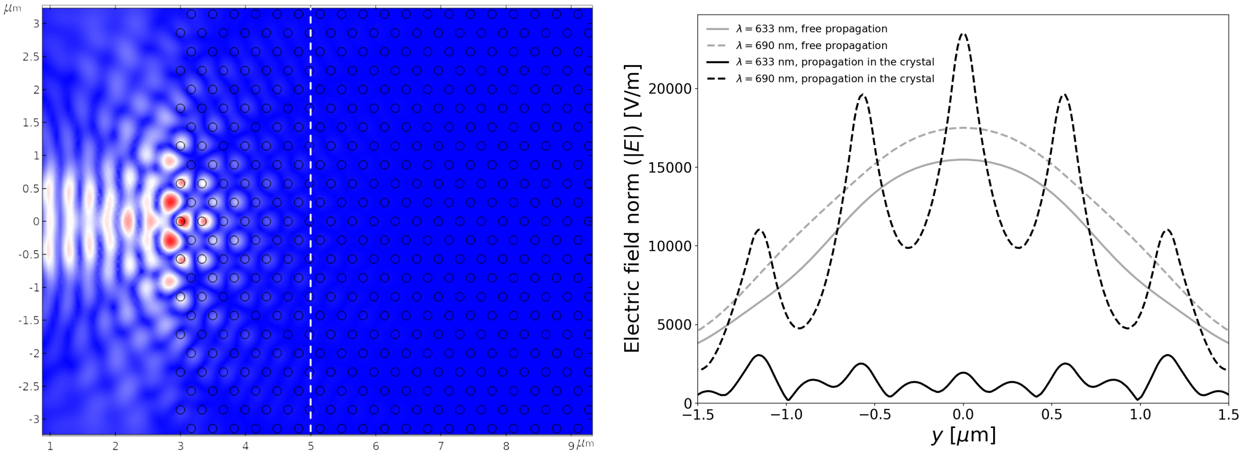

(a) $\Gamma - \mathrm{K}$ orientation with a cutline at $x = 5$ μm.

(b) Electric field profile

Figure 4.38: Electric field profile along y-axis at $x = 5$ μm.

field profile undergoes variations without significant losses.

In both cases, the electric field at the frequency inside the bandgap is considerably attenuated, while for the frequency studied outside the bandgap the electric field does not suffer significant losses and propagates like free space. This is predicted from the theoretical model.

4.3.3 Rectangular lattice

Table 4.8: Results comparison among theoretical model and machine learning algorithms

Bandgap properties	Theoretical model	Regression 11 degree polynomial	K-NN 3 NN	Decision tree max depth = 15	ANN
Center (λ_c) [nm]	655.245	652.154	655.653	651.866	652.340
Porcentual error	-	0.472%	0.062%	0.516%	0.433%
Width ($\Delta\lambda$) [nm]	26.011	34.872	24.594	33.859	21.678
Porcentual error	-	34.066%	5.448%	30.172%	16.658%

For the rectangular lattice, the parameters used were $a_x = 300$ nm, $a_y = 480$ nm, $d_x = 100$ nm and $d_y = 240$ nm. With these parameters, the theoretical model calculates a bandgap centered at $\lambda_c = 655.245$ nm with a width $\Delta\lambda = 26.011$ nm. These parameters were used in the algorithms and the results are shown in table 4.8.

All algorithms predict the center of the bandgap with a discrepancy of less than 4 nm and a percent error of less than 1%. On the other hand, the width discrepancy is less than 9 nm, which represents a percent error of approximately 34%. In this particular case, the algorithms predict the bandgap center better than the bandgap width.

Regarding the inverse design, the predicted parameters for a bandgap center $\lambda_c = 633$ nm and width $\Delta\lambda = 20$ nm are shown in table 4.9. The best performance to predict the lattice constants was obtained with polynomial regression, k-nearest neighbors and ANN, where the range of lattice constant a_x is between 256.403 and 258.906 and a lattice constant a_y in a range of 383.173 to 391.840, while decision tree predicts a lattice constants $a_x = 271.527$ nm and $a_y = 407.885$ nm.

Table 4.9: Predicted parameters and their respective optical response calculated with the analytical model.

Algorithm	Structural parameters				Calculated optical response	
	(a_x) [nm]	(a_y) [nm]	d_x [nm]	d_y [nm]	(λ_c) [nm]	($\Delta\lambda$) [nm]
Regression 10 degree polynomial	256.403	383.173	179.228	267.842	636.673	41.391
Porcentual error	-	-	-	-	0.580%	106.955%
K-NN K = 30	257	391.840	176.082	268.467	636.406	46.064
Porcentual error	-	-	-	-	0.539%	130.320%
Decision Tree max depth = 15	271.527	407.885	178.480	268.111	656.410	49.051
Porcentual error	-	-	-	-	3.698%	145.255%
ANN	258.906	388.033	171.963	257.729	633.919	45.964
Porcentual error	-	-	-	-	0.145%	129.820%

The base size predicted for all algorithms is in the range 171.963 to 179.228 nm for d_x, and 257.729 nm to 268.467 nm for d_y. With the trained algorithms, for the predicted structural parameters, the bandgap width calculated with the analytical model is approximately twice as large as the target. However, the information is useful for outlining the target parameters. The bandgap center and width were calculated with the analytical model, using the parameters $a_x = 260$ nm, $a_y = 390$ nm, $d_x = 170$ nm, $d_y = 250$ nm, in the paths $\Gamma - \mathrm{X} - \mathrm{S} - \mathrm{Y} - \Gamma$ and $\Gamma - \mathrm{X} - \mathrm{S} - \Gamma$. Both photonic band structures are shown in Fig. 4.39.

For the former path, there are two partial bandgaps, one for $\Gamma - \mathrm{X}$ orientation, centered at $\lambda_c = 660.844$ nm and with a width $\Delta\lambda = 102.971$ nm. The other bandgap is centered at $\lambda_c = 938.830$ nm and has a width $\Delta\lambda = 152.377$ nm. For the second path, a complete bandgap arises, centered at $\lambda_c = 632.728$ nm and has a width $\Delta\lambda = 46.739$ nm. These last results are consistent with the ANN prediction.

In Fig. 4.40, the numerical simulation is shown for two orientations. These simulations were performed using the parameters mentioned above with a wavelenght $\lambda = 633$ nm. Figure 4.40a corresponds to a SPPs incident on a PhPl crystal for the $\Gamma - \mathrm{X}$ orientation, where it is possible to observe the inhibition of propagation into the PhPl crystal, as suggested by the

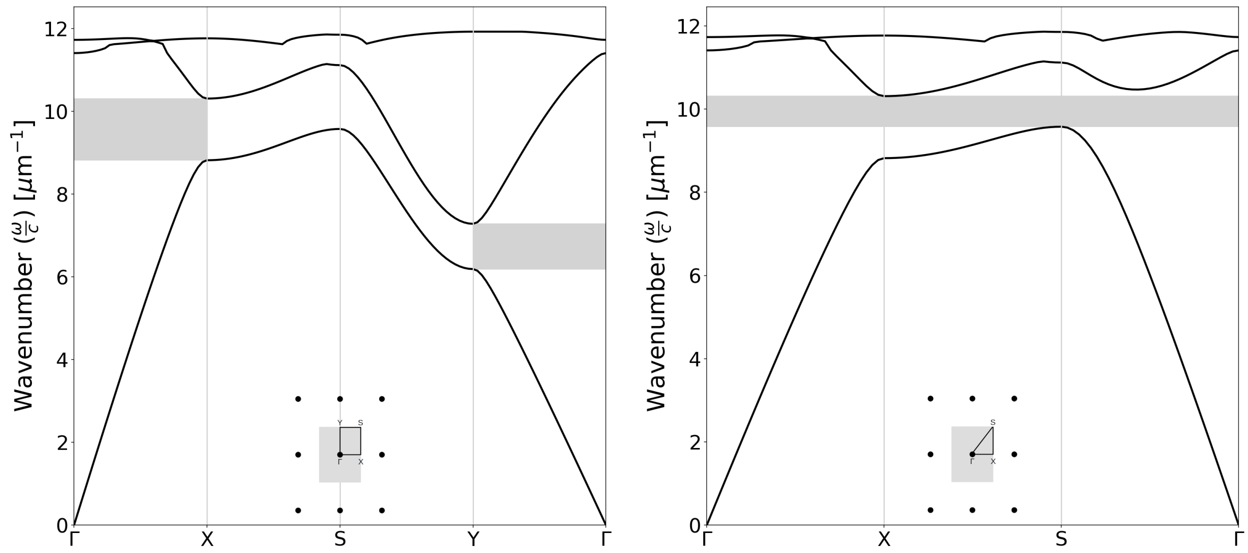

(a) $\Gamma - \mathrm{X} - \mathrm{S} - \mathrm{Y} - \Gamma$ path. (b) $\Gamma - \mathrm{X} - \mathrm{S} - \Gamma$ path

Figure 4.39: Band structure of rectangular lattice with an elliptical base.

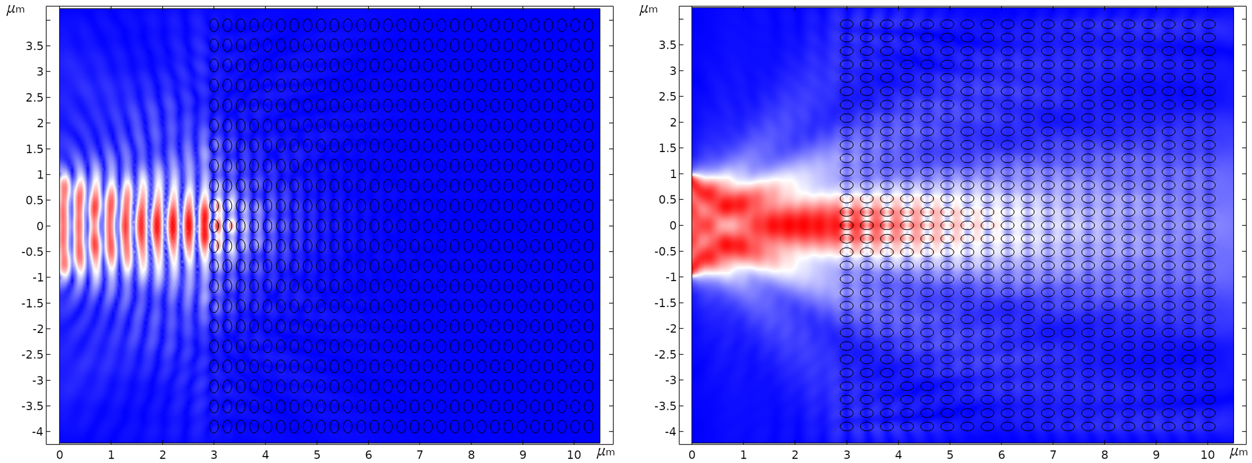

(a) $\Gamma - \mathrm{X}$ orientation. (b) $\Gamma - \mathrm{Y}$ orientation

Figure 4.40: Numerical simulation.

band structures shown in Fig. 4.39.

In contrast, for $\Gamma - \mathrm{X}$ orientation, the SPPs propagate as shown in Fig. 4.40b. Although there is interference, it does not significantly affect the propagation of SPPs, as it can be seen in Fig. 4.40b, SPPs propagate in this orientation in a similar way as in an air-Au interface.

Figure 4.41a shows the comparison of the intensity of SPPs in the PhPl crystal in the $\Gamma - \mathrm{X}$

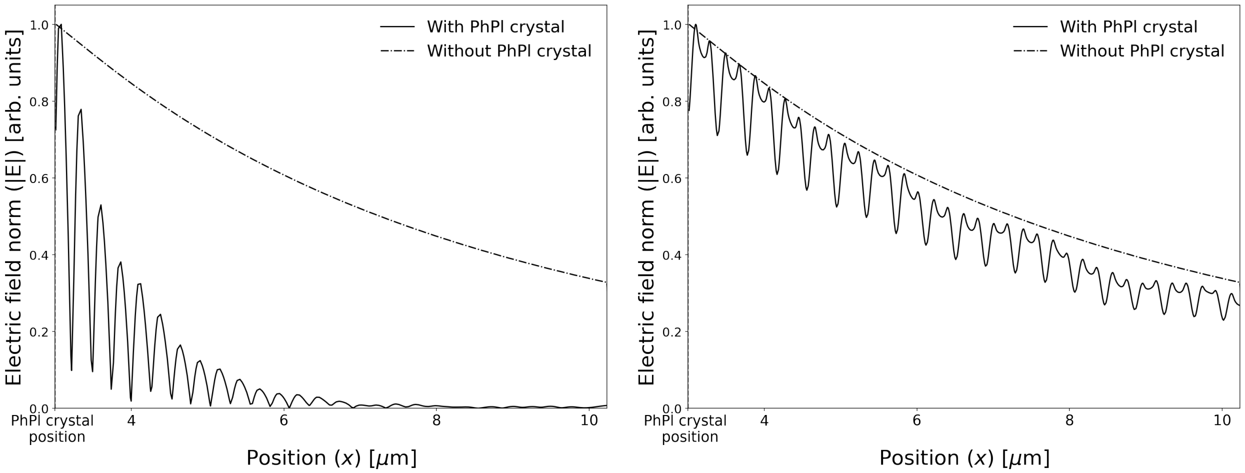

(a) $\Gamma - \mathrm{X}$ orientation.

(b) $\Gamma - \mathrm{Y}$ orientation

Figure 4.41: SPPs intensity in free space and PhPl crystal.

orientation, while Fig. 4.41b shows the intensity in the $\Gamma - \mathrm{Y}$ orientation. Both are compared with the intensity of SPPs at an air-Au interface. As it can be seen, the intensity decreases faster for SPPs propagating in the PhPl crystal in the $\Gamma - \mathrm{X}$ orientation, as expected from the band structure. On the other hand, for SPPs propagating in the PhPl crystal in the $\Gamma - \mathrm{Y}$ orientation, the intensity is quantitatively similar to that of SPPs propagating at the air-Au interface, which is also supported by the band structure showed in Fig. 4.39a.

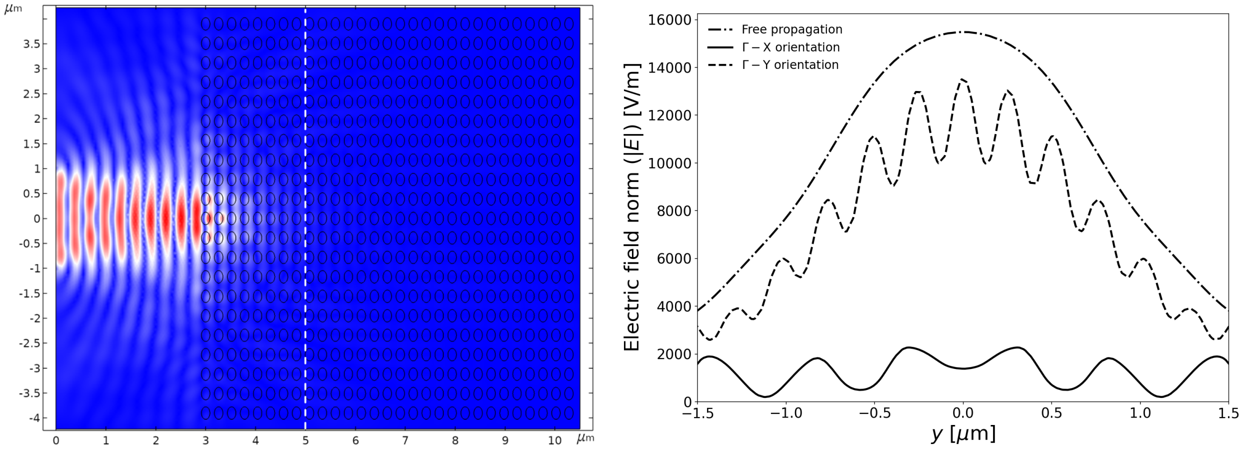

(a) $\Gamma - \mathrm{X}$ orientation with a cutline at $x = 5$ μm.

(b) Electric field profile

Figure 4.42: Electric field profile along y-axis at $x = 5$ μm.

As in the previous lattice, the electric field profiles are shown in the figure. In this case, the electric field profiles correspond to SPP excited at 633 nm, and are compared for the two crystal orientations. As expected, for the $\Gamma - \mathrm{X}$ orientation there is an inhibition of the electric field, (solid curve). On the other hand, for the $\Gamma - \mathrm{Y}$ orientation, although not significant, there is a slight attenuation, as represented by the dashed line. Again, these numerical results are predicted from the theoretical model

References

[1] Xiaoning Zhang, Jun Qiu, Xingcan Li, Junming Zhao, and Linhua Liu. Complex refractive indices measurements of polymers in visible and near-infrared bands. *Appl. Opt.*, 59(8):2337–2344, Mar 2020.

[2] P. B. Johnson and R. W. Christy. Optical constants of the noble metals. *Phys. Rev. B*, 6:4370–4379, Dec 1972.

[3] Sukanya Randhawa, María Ujué González, Jan Renger, Stefan Enoch, and Romain Quidant. Design and properties of dielectric surface plasmon bragg mirrors. *Opt. Express*, 18(14):14496–14510, Jul 2010.

[4] Sergey I. Bozhevolnyi, John Erland, Kristjan Leosson, Peter M. W. Skovgaard, and Jørn M. Hvam. Waveguiding in surface plasmon polariton band gap structures. *Phys. Rev. Lett.*, 86:3008–3011, Apr 2001.

[5] S. C. Kitson, W. L. Barnes, and J. R. Sambles. Full photonic band gap for surface modes in the visible. *Phys. Rev. Lett.*, 77:2670–2673, Sep 1996.

[6] V. S. Volkov, S. I. Bozhevolnyi, K. Leosson, and A. Boltasseva. Experimental studies of surface plasmon polariton band gap effect. *Journal of Microscopy*, 210(3):324–329, 2003.

[7] A.-L. Baudrion, J.-C. Weeber, A. Dereux, G. Lecamp, P. Lalanne, and S. I. Bozhevolnyi. Influence of the filling factor on the spectral properties of plasmonic crystals. *Phys. Rev. B*, 74:125406, Sep 2006.

Chapter 5

Conclusions

This thesis deals with the study of hybrid photonic-plasmonic crystals. A general theoretical model is presented to calculate the band structure of dielectric photonic crystals on a thin film of Au or Ag. However, the model can be extended to other metals by approximating the inverse of the dielectric function to a suitable analytic function.

The proposed model is adjusted for an optical response in the wavelength range of 548.6-1937 nm for the case of Au, while for Ag the range is 331.5-1937 nm. These adjustment ranges are adequate for SPP propagation since in both cases the optical response is far from the maximum value of the effective refractive index, where the losses are greater.

It was verified that the model was consistent with the studied physics. This was done for two different filling fractions, and the calculated band structure was compared with the dispersion relation of the physical system. For both types of crystals, the band structure and the dispersion relation match perfectly.

The dielectric-Au and dielectric-Ag PhPl crystals respond very similarly in the 600-1937 nm range because the effective dielectric functions are very similar. However, dielectric-Ag PhPl crystals offer a wider range of performance, practically throughout the entire visible and near-infrared spectrum.

Of the three two-dimensional structures studied, only the triangular lattice produces complete bandgaps with the contrast of refractive indices used, while the square and rectangular lattices shows partial bandgaps for certain orientations. The bandgap can be made complete by increasing the contrast of refractive indices, so the properties of the bandgap are also determined by this quantity. Furthermore, for the rectangular lattice, it is possible to generate a complete bandgap by shortening the path of the points of maximum symmetry, in particular for a trajectory analogous to that of the square lattice.

From the theoretical studies, it was observed that the base geometry has no significant influence on the bandgap properties. Such properties are mainly determined by the lattice constant, the base size and the combination of both parameters. The results show that the center of the bandgap is a monotonically increasing function of the lattice constant and the filling fraction. The width of the bandgap, on the other hand, is a monotonically increasing function of the lattice constant but, as a function of the filling fraction, it reaches a maximum and then decreases as the filling fraction approaches 1.

The relationship between the lattice constant and the filling fraction that determines the bandgap properties is not obvious, so machine learning algorithms were used to tune the optical response. These algorithms are polynomial regression, nearest neighbors, decision trees and artificial neural networks. All of them are quite efficient to calculate the optical response from the structural properties with accuracies close to 100% for the three two-dimensional crystal lattices.

Regarding the inverse design, that is, predicting the structural properties from the optical response, only the the artificial neural networks performed adequately, with an accuracy above 98% in the case of the triangular lattice, and above 95% for the rectangular lattice.

The results obtained from the artificial neural networks for a target optical response were compared with the theoretical model calculations showing percent errors of less than 2.5%. From the above it can be concluded that ANNs perform better than the rest of the algorithms when implemented in the inverse design. To corroborate the results, numerical simulations were performed that reveal the correct performance of the hybrid PhPl crystals to inhibit the propagation of SPPs in them.

As for the experimental results, the stage reached in this work was the excitation of SPPs. Using FIB, a slit was fabricated in an Au thin film to scatter light and excite SPPs. Such a structure fabricated on the Au film surface is a source of evanescent moments to excite SPPs.

This work contributes to the integration of theoretical tools and optimization algorithms to make the design of photonic and plasmonic elements more efficient. It includes mathematical tools to solve an electromagnetism problem, as well as computational algorithms to make the design of the studied physical systems more efficient. It is important to mention that the algorithms do not replace the analytical work, but complement it, allowing it to approach experimental problems and integrate them with their theoretical aspect.

In general terms, a theoretical-numerical tool is presented to calculate the optical response of PhPl hybrid crystals of Au and Ag. In addition, with this tool, it is possible to define the structural properties of these photonic-plasmonic systems to tune their optical response. These physical systems can be applied in various devices such as plasmonic waveguides, reflectors, cavities, sensors, among others.

Appendix A

Experimental techniques

This appendix describes the operation of the experimental techniques used in this work. These experimental methods refer to the samples fabrication using lithography techniques, in addition to the optical technique for sample characterization. The most detailed explanation is about the fundamentals on which the Leakage Radiation Microscopy (LRM) is based for its experimental implementation, since it is the main detection technique that will be used, due to the fact that it allows acquiring more information than other conventionally used techniques. The importance of this characterization method lies in its versatility to excite SPPs locally, in addition to the fact that it is possible to "visualize" the propagation in the direct space and in the Fourier space.

Samples fabrication

Sample fabrication by mean of lithography techniques are versatile method to obtain nanostructures with complex and detailed geometrical shapes. Also, with these techniques, a wide materials variety can be used to synthesize the samples.

In this subsection, a qualitative description of two different lithography techniques is exposed. These lithography techniques are «focus ion beam lithography» (FIBL) and «electron beam lithography» (EBL). As in the algorithms, the description of the samples fabrication will be brief, avoiding falling into an exhaustive explanation of the technical details [1].

Focus ion beam lithography (FIBL)

The focus ion beam (FIB) is a high resolution microscopy technique that allows the sample preparation and the analysis of particular zones of the sample [2]. One of the most used microscopy technique is the scanning electron microscopy (SEM), however, has limitations that FIB can overcome, especially when it comes to resolution limitations [2].

Ions are more massive that electrons, so they can be cause damage in the sample when it is analyzed. From the interaction of the ion beam with the the sample atoms, an amount of material is removed from the specimen, but the above can be an advantage to modify the sample in a controlled way [2]. This process, known as «sputtering», is useful to create very varied patterns on the surface of the sample.

In general, a FIB system is made up of some basic components such as a system and vacuum camera, a liquid metal ion source (LMIS), an ions column where are the "optical" elements such as electromagnetic lenses, aperture, the platform to control the sample, the detectors and a computer to integrate all components as a whole system [3].

For a good performance of the FIB system, the preassure must be lesser than 1×10^{-4} torr. In particular, the sample camera works approximately at 1×10^{-6} torr. On the other hand, to avoid the source contamination and the interaction between the ions with some molecules within the ions column, the operation preassure is about 1×10^{-8} torr [3].

In most of the cases, ions are obtained from a liquid galium (Ga) source although, another sources can be used. Using Ga has advantages over other materials since it minimizes reactions among liquid and tungsten (W) constructed parts, plus its low melting point volatility provides long source life, and its low vapor pressure ensures that the Ga is in its pure form [3, 4].

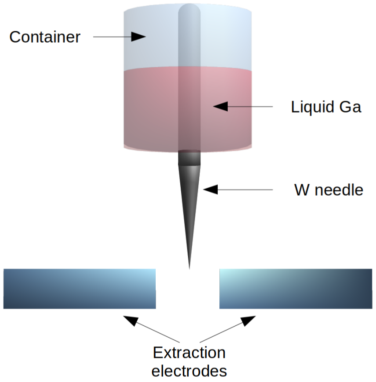

Figure A.1: Liquid metal ion source

The ion source is in a container that is in contact with a W needle, and the liquid metal flows through the needle. To extract ions, a strong electric field is applied to efficiently ionize Ga, as it shown in Fig. A.1.

The extracted ions are accelerated through the ions column applying a voltage towards several optical elements. Typically, the FIB systems, in ions column, has a condenser lens to defines the beam and an objective lens to focus it on the sample. In addition to the lenses, another optical elements such as apertures are used to define the beam. In Fig. A.2, a diagram of FIB system is shown.

One of the most important elements in a FIB system is the sample platform, and its importance lies in the accuracy control of the specimen position. Generally, this platform has five movement axis, three for X, Y and Z positions, one for rotation and one for tilt [3], and the resolution is, usually, about 0.1 μm.

When the ion beam interacts with the sample atoms, several physical processes arises. Some of these are reflection and backscattering of ions, secondary electron emission, atomic

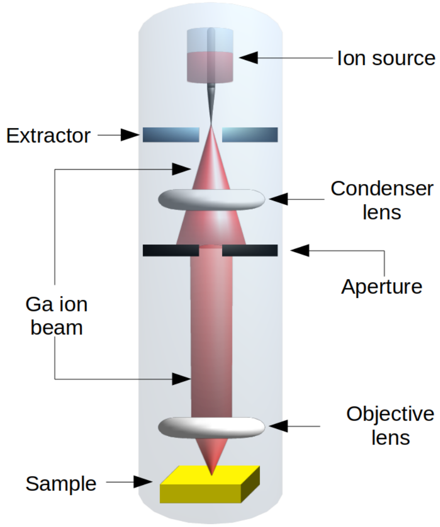

Figure A.2: FIB system diagram

«sputtering», and ion emission and damage in the sample [4]. From the interaction, there are elastic and inelastics collisions, and, finally ions are implanted in the sample, [3, 4].

For elastic collisions, the ion energy is transferred to the sample atoms, which in turn causes another collisions between the atoms [3, 4]. For a enough energy and, if this collisions occur near to the sample surface, the atoms can be ejected from it [5]. This above process is known as sputtering and offer one of the most useful capabilities of FIB system, milling. If the ion beam characteristics are controlled, the FIB are a useful tool to modify the sample surface and fabricate nanostructures [6].

One of the advantages of nanofabrication by milling is that it is a mask-free process, the patterns are transferred directly to the surface sample from the interaction with the ion beam [5]. This process can be controlled in an accurate way, with a high resolution, and in a wide variety of materials [5]. The above shows the great versatility of FIB systems for both analysis and sample fabrication [4, 5, 6].

Electron beam lithography

The electron beam lithography (EBL) is an widely used technique to fabricate nanostructures. Basically, it consists of exposing an electrically sensitive materials to an electron beam with the aim to induce changes in its chemical properties [6].

In general, the EBL is made up of an electron gun, a vacuum system and a control system [1, 6]. The electron gun source generates the electron beam, it is accelerated, focused, and projected to the sample by lenses and a deflection system [1, 6]. The vacuum system establishes the optimal conditions for high vacuum in the electron gun column and in the working chamber. Finally, the control system coordinates the electron beam properties and the sample position. With this, the pattern transfer to the sample can be successful [6].

There are two ways to produce electrons. The thermionic emission consists in heating up the material emission until a sufficiently high temperature. This method is widely used since it has a higher efficiency to produce electrons a lower cost. The other method is by field emission, where the electrons are extracted by applying an intense electric field [6]. Basically, the electron source consists of three electrodes: a cathode, an electrode to focus known as «Wehnelt electrode», and an anode [6].

In thermionic emission, the material is heated sufficiently for the electrons to obtain the energy necessary to overcome the work function, and these electrons can be extracted applying an electric field [6]. However, the emission material must have a low work function, so the most used materials in both sources types are Tungsten (W) and Tantalum (Ta) [1, 6].

Once the electrons are extracted from the cathode by applying an electric field, the potencial between the Wehnel electrode and the anode shapes the beam to converge to the focal point [6]. The beam is characterized by several parameters such as diameter, focal point distance, current density, etc. These parameters are tuned by a deflection system depending on the desired particular aplications [6].

The lenses in the electron gun are electromagnetic and, with that, it is possible to deflect and focus the beam and, forming the images. These lenses, which function as convex lenses to magnify the object image, commonly are made up by permanent magnets or coils. Their design is based on fundamental electromagnetic laws such as the Lorentz force law; however, it is important to consider effects analogous to those found in light optics, such as aberration and astigmatism [6].

The pattern transfer depends mainly on the sample materials, which are used as recording and transfer media in the lithography process. This material is a resist, that is, a polymeric solution deposited on the substrate surface. From the interaction with the beam, the molecules that constitute the material are ionized or excited, resulting in chemical reactions, which cause the resist to modify its structural characteristics [6].

Subsequently, during the developing process, the resist is treated with a solution. Depending on the nature of the resist, some parts of it will be removed. If the resist is positive, the exposed parts are removed, and if it is negative, the parts not exposed to the beam are removed [1, 6].

For a positive resist, the beam breaks the bonds of the polymer, the exposed areas remain with a low molecular weight and are eliminated by the developer, while the rest of the resist remains practically intact. For a negative resist, the process is based on crosslinking of the exposed zone, which is insoluble after exposure to the beam [1, 7].

One of the most commonly used materials is polymethyl methacrylate (PMMA), which can be used as a positive or negative resist depending on the dose of the electron beam. The resolution presented in this material can be as high as 10 nm, when it is positive, and 50 nm, when it behaves as a negative resist [1, 6, 7]. Other materials that are used in positive resistors are the copolymer methyl methacrylate and methacrylic Acid (P(MMA-MAA)) and, Polybutene Sulfone (PBS), which present high sensitivity [7]

Regarding negative resins, among the materials used are the copolymer of glycidyl methacrylate and ethylacrylate P(GMA-co-EA), known as COP, which have an advantage when high speed synthesis is required, but have a low resolution of approximately 1 μm [6].

Once the pattern on the resist surface is written, it is necessary to transfer it to the substrate.

There are two types of transfer methods, the additive in which there are two processes, lift-off and plating, and the subtractive method [6].

In the lift-off process, after the beam passes through the resist, it remains soluble even though other material is deposited on the surface. Subsequently, the sample is developed and the soluble part of the resist is lifted off, leaving the desired structure on the surface [6]. Figure A.3a shows schematically the lift-off process. In the other additive process, the plating process, a metallic film is deposited directly on the areas where the resist has been removed after the development [6], as shown in Fig. A.3b.

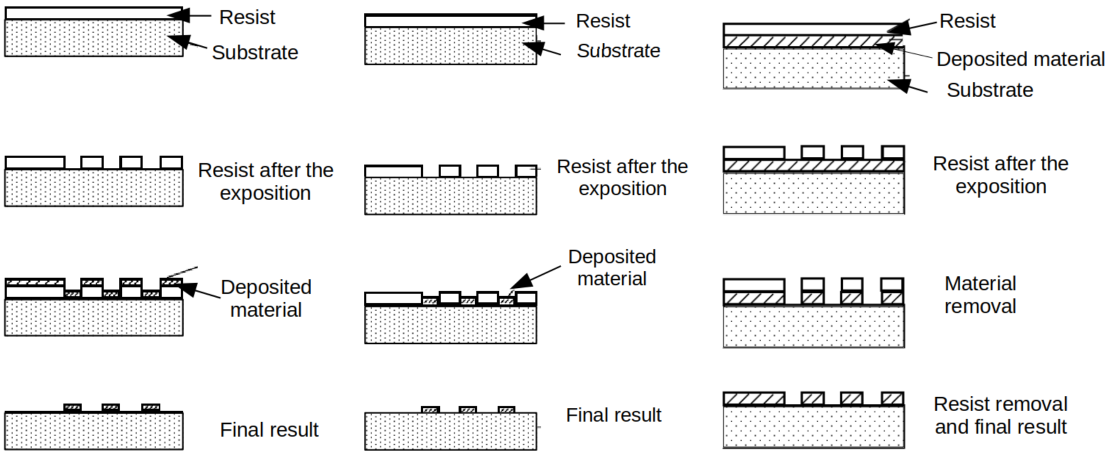

(a) Liftoff process. (b) Plating process. (c) Sustractive process.

Figure A.3: Transfer process.Modified from Yao and Wang, 2005.

In the subtractive process the patterned resist works as a mask. The layer on which the lithography is to be performed is deposited directly on a substrate, and on it, it is deposited the resist, which is exposed to the electron beam to produce the desired pattern, and is subsequently developed. After development, the parts of the layer that were not protected by the resist are removed by immersing them in a liquid or exposing them to a plasma reactor, resulting in the lithography on the layer. The first removal method is known as «wet etching» and the second is known as «dry etching» [6].

Leakage radiation microscopy

Since the Surface Plasmons Polaritons (SPPs) are an electromagnetic phenomenon, they can be studied through the classical electrodynamics. From the Maxwell equations, the problem can be approached by solving the wave equation for the TM-polarized electromagnetic wave and applying the appropriate boundary conditions for an interface formed between two semi-infinite media, one dielectric and the other conducting. This way, it is possible to determine the dispersion relation of the SPPs [8, 9, 10, 11] in a dielectric-conductor interface.

From the dispersion relation, it is known that the real part of the SPPs wavenumber at such an interface (Re{β}) is larger than the wavenumber of light propagating in the air or in vacuum (k_0) [8, 9, 10]

$$\text{Re}\{\beta\} = \frac{\omega}{c}\text{Re}\left\{\sqrt{\frac{\epsilon_c \epsilon_d}{\epsilon_c + \epsilon_d}}\right\} > \frac{\omega}{c} = k_0, \tag{A.0.1}$$

where ω is the frequency of the incident light, c the velocity of light in vacuum, ϵ_c the dielectric function of the conductor and ϵ_d the dielectric function of the dielectric. Physically, equation (A.0.1) means that it is not possible to excite SPPs by simply illuminating the interface, which implies the need to use special optical techniques to increase the wavenumber of the light to achieve phase matching [8].

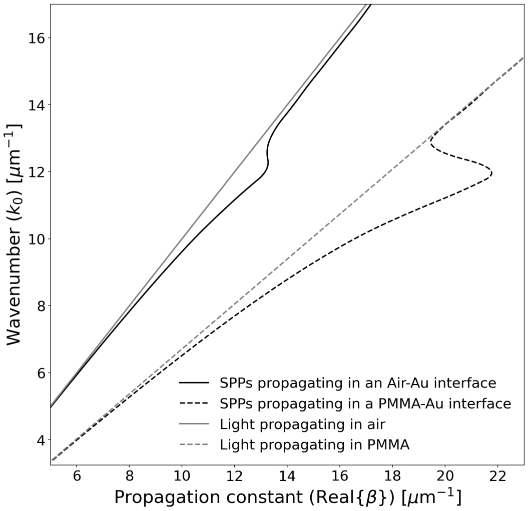

Figure A.4: SPPs dispersion relations for two different interfaces compared to light propagation in air and in PMMA.

To illustrate the above, Fig. A.4 compares four dispersion relations: SPPs propagating at an air-gold interface (continuos black line), SPPs propagating at an PMMA-gold interface (dashed black line), the light propagating in the air (continuos gray line) and the light propagating in PMMA (dashed gray line). However, in practice, metallic media of finite thickness are used, so that the problem corresponds to that of a conductive film of thickness d, where its dielectric function is given by $\epsilon_2(\omega) = \epsilon_2' + i\epsilon_2''$.

Defining the system geometry, the thin film is in the positive part of the z-axis, between two dielectric media with dielectric functions ϵ_1 and ϵ_3, respectively. This way, the thin film lies between $z = 0$ and $z = d$, where the component normal to the surface coincides with the z-axis. Assuming, without loss of generality, that the SPPs propagation is along the x-axis, the y component of the magnetic field of a TM-polarized wave in each of the media are [8, 10, 12]

$$\begin{aligned} &\text{a)} & H_{y1}(\vec{r},t) &= Ae^{i\beta x}e^{-k_1 z}e^{-i\omega t} & z &\geq d \\ &\text{b)} & H_{y2}(\vec{r},t) &= e^{i\beta x}\left[Be^{k_2 z} + Ce^{-k_2 z}\right]e^{-i\omega t} & 0 < z &< d \\ &\text{c)} & H_{y3}(\vec{r},t) &= De^{i\beta x}e^{k_3 z}e^{-i\omega t} & z &\leq 0, \end{aligned} \tag{A.0.2}$$

where

$$k_j = k_{z,j} = \sqrt{\beta^2 - \left(\frac{\omega}{c}\right)^2 \epsilon_j} \tag{A.0.3}$$

is the z component of the wave vector, with $j = 1, 2, 3$ corresponding to each medium and β is the wavenumber of SPPs.

According to the boundary conditions, the following must be satisfied [10]

$$\begin{aligned} H_{y1}(z = d) = H_{y2}(z = d) \quad &, \quad \frac{1}{\epsilon_1}\frac{\partial H_{y1}}{\partial z}|_{z=d} = \frac{1}{\epsilon_2}\frac{\partial H_{y2}}{\partial z}|_{z=d} \\ H_{y2}(z = 0) = H_{y3}(z = 0) \quad &, \quad \frac{1}{\epsilon_2}\frac{\partial H_{y2}}{\partial z}|_{z=0} = \frac{1}{\epsilon_3}\frac{\partial H_{y3}}{\partial z}|_{z=0}. \end{aligned}$$

From the above equations, and with the corresponding algebraic manipulations, the following implicit equation is obtained

$$\left(\frac{\epsilon_2 k_1}{\epsilon_1 k_2} + 1\right)\left(\frac{\epsilon_2 k_3}{\epsilon_3 k_2} + 1\right) = \left(\frac{\epsilon_2 k_1}{\epsilon_1 k_2} - 1\right)\left(\frac{\epsilon_2 k_3}{\epsilon_3 k_2} - 1\right) e^{-2k_2 d}, \tag{A.0.4}$$

which reduces to the equation (A.0.1) when $d \to \infty$. It is possible to obtain the dispersion relation of the SPPs by solving the equation numerically, as shown in Fig. A.5.

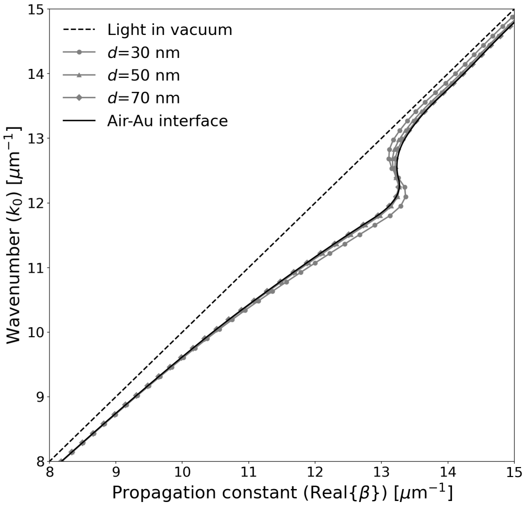

Figure A.5: Dispersion relations of SPPs for thin films with different thicknesses between two semi-infinite media.

The image shows the SPPs dispersion relations in an interface formed between air and gold thin films of 30, 50, and 75 nm thickness, and it is compared with the SPPs dispersion relation in an interface formed by air and gold of semi-infinite thickness. These dispersion relations were calculated numerically through Python code, and the gold permittivity data were extracted from reference [13].

The curves plotted show a good agreement among the dispersion relation of SPPs propagating in an interface formed between two semi-infinite media, and the dispersion relations for a 50 nm and 75 nm thin films. Therefore, it is a good approximation to consider them as equivalent, at least in the area of the spectrum that is of interest.

Respect to the imaginary part of the propagation constant β, it is related to the propagation length of the SPPs. This quantity is defined as the distance at which the intensity decays to $1/e$ [10, 14], that is, when

$$\frac{I(x)}{I_0} = e^{-2\beta'' L_{SPP}} = \frac{1}{e}, \tag{A.0.5}$$

where I_0 is the initial intensity, β'' is the imaginary part of the propagation constant β, and L_{SPP} is the propagation length of SPPs. This way, the propagation length is defined as

$$L_{SPP} = \frac{1}{2\beta''}. \tag{A.0.6}$$

Figure A.6 shows the SPPs propagation lengths at an air-gold interface and at an PMMA-gold one.

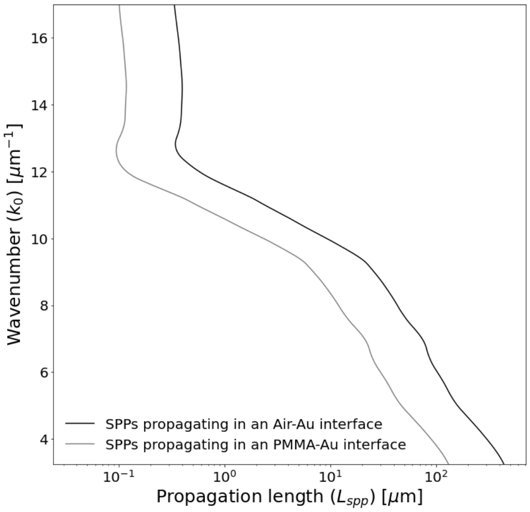

Figure A.6: SPPs propagation length at an air-gold interface and at a PMMA-gold interface.

As mentioned above, it is necessary to achieve phase matching to excite SPPs using light. One of the most used optical techniques is the prism coupler. In this method, also known as «Atenued total reflection» (ATR), the sample is placed on one side of the prism in what is known as the «Kretschman-Raether configuration». There is another configuration of this coupler, called the «Otto configuration», where the nanostructure is separated by about one wavelength from one of the prism faces [8, 9, 10]. Both configurations are illustrated in Fig. A.7.

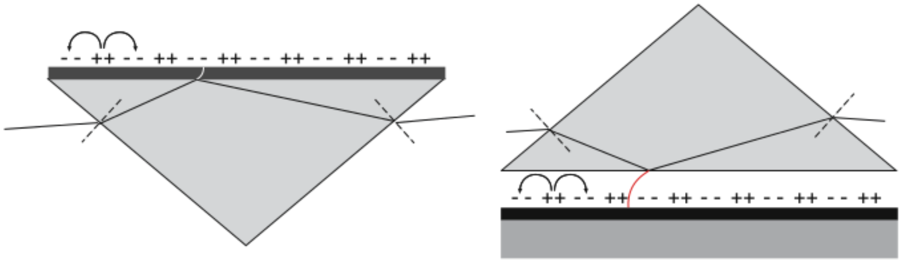

Figure A.7: Prism coupler. Kretschman-Raether configuration (left) and Otto configuration (right). Modified from reference Zayats, 2005.

Experimentally, this SPPs excitation technique is accessible, where, in the simplest case, the sample adheres to one of the prism faces and its reflectance is measured as a function of the angle of incidence and/or wavelength. The excitation of SPPs is identified, conventionally, by a decrease in the intensity of the reflected beam at angles larger than the total internal reflection.

However, this method has limitations, for example when it comes to studying the local excitation of SPPs. The main difficulty is that the spot size can significantly affect the experimental data. In addition, it is not always easy to identify the nanostructures on the surface and illuminate them and illuminate them from the prism. Furthermore, there are another techniques to obtain more complete information about the propagation, even, “visualize” it, such as near-field microscopy [15, 16].

Another optical method to excite SPPs is by diffraction of the light interacting with elements on the interface [10]. Even excitation can be achieved by light scattered by small defects in a flat metal film [9, 17], which are works as a source of evanescent moments to match the light dispersion relation to that of the SPPs [12]. Considering the above, it is possible to design elements with well-defined sizes and geometric shapes to take advantage of light scattering and achieve local excitation.

Once SPPs are excited and propagate at the dielectric-conductor interface, it is necessary to have the right tools to extract as much information as possible. «Leakage Radiation Microscopy» (LRM) is a method based on the far-field detection of radiation caused by propagating SPPs. One of the advantages of this technique is that it is possible to obtain images that allow quantitative analysis of SPPs propagation [12].

In this technique, to excite SPPs, the light beam is focused at a nanostructure on the interface with a lens or a microscope objective. Since the nanostructure works as a source of evanescent momentum, the light is scattered by it, resulting in phase matching and partial coupling of light in SPPs [12]. These propagate along the interface and their electromagnetic field decay exponentially. By conservation of momentum, the SPPs are detected as emitted leaky radiation, at a certain angle, towards the medium with the largest refractive index [12, 18], which in this case is the substrate, as shown schematically in Fig. A.8.

The above is supported by the dispersion relation shown in Fig. A.9. As an example, the image shows several dispersion relation of SPPs for different systems. The gray curve with triangles is the dispersion relation of SPPs propagating at an interface formed between air and

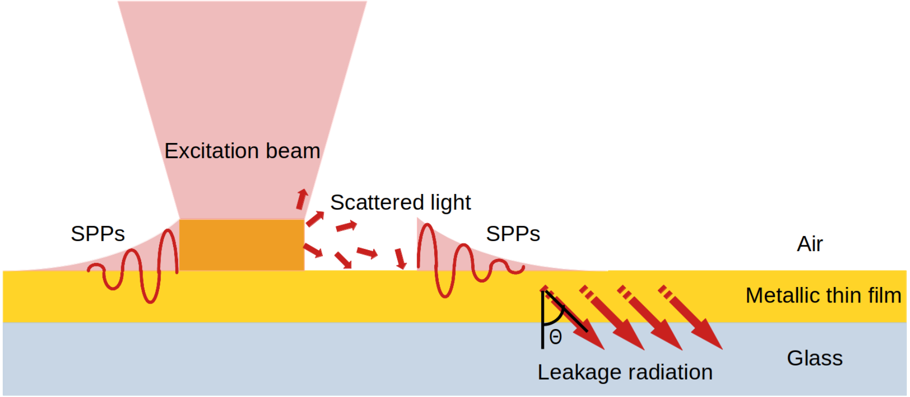

Figure A.8: The physical mechanism of excitation and decay of SPPs.

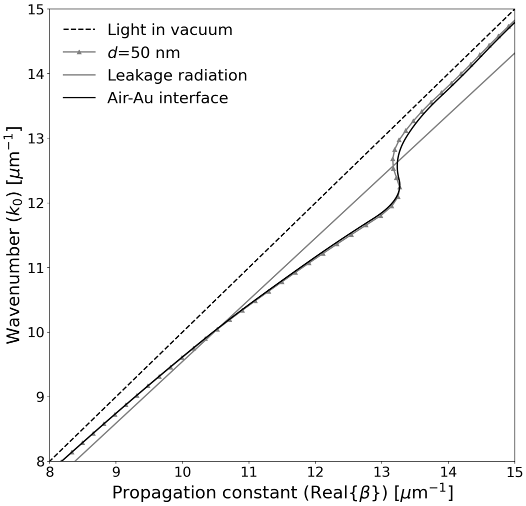

Figure A.9: SPPs dispersion relations for a 50 nm thin film and for an interface formed by semi-infinite media.

a 50 nm thin film. The solid black curve is the dispersion relation of SPPs propagating at the interface formed between two semi-infinite media. Both curves intersects with the dispersion relation of a light beam propagating at an angle of $\theta = 43.39°$ in BK7 glass medium, represented by the solid gray line.

Respect to the above, the parallel component of the wavevector of this emitted light is given by

$$k_x = n_3 k_0 \text{sen}\theta, \tag{A.0.7}$$

where n_3 substrate refractive index, and $k_0 = \omega/c$ is the wavenumber in free space. This way, the intersection of both dispersion relations mathematically means

$$\mathrm{Re}\{\beta\} = k_0 \mathrm{Re}\left\{\sqrt{\frac{\epsilon_1\epsilon_2}{\epsilon_1+\epsilon_2}}\right\} = n_3 k_0 \mathrm{sen}\theta_{SPPs}, \tag{A.0.8}$$

where θ_{SPPs} is the angle at which the radiation emits toward the substrate when the SPPs propagate at the interface.

An experimental setup for the implementation of LRM technique is shown in the following figure. The diagram shows the different elements for excitation, in this case a first microscope objective focusing the light on a nanostructure on the conductor surface. For detection and visualization, a second microscope objective is used with a the lens array and a CCD camera.

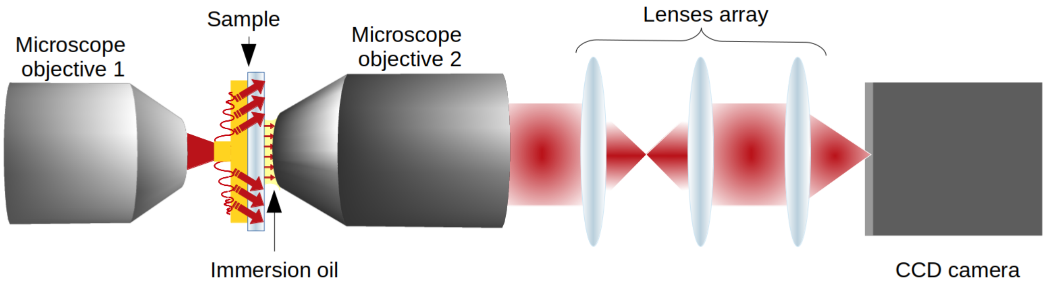

Figure A.10: Experimental setup of LRM

To infer the information about SPPs, the radiation leaked from the interface through the substrate is collected with a «large numerical aperture» microscope objective (NA>1), since the emission angle is larger than the critical one for the total internal reflection for a air-glass interface. The light collected by the second objective of the microscope and transferred through it, is directed to a CCD camera and, depending on the lens array, it is possible to access the direct plane or the Fourier plane.

The most important element in the LRM setup is the microscope objective. It is characterized by different properties, one of the most relevant is the numerical aperture. This dimensionless quantity defines a range of angles in which the optical system can accept or emit light [19]. This parameter is defined as

$$\mathrm{NA} = n\mathrm{sen}\theta, \tag{A.0.9}$$

where n is the refractive index and θ is the emission or incidence angle of the light. Relating this equation to the equation (A.0.8), it is obtained

$$\mathrm{Re}\left\{\beta\right\} = k_0\mathrm{AN} \Rightarrow \mathrm{Re}\left\{\frac{\beta}{k_0}\right\} = \frac{\beta'}{k_0} = \mathrm{AN} = n_3\mathrm{sen}\theta. \tag{A.0.10}$$

This quantity is known as «efective refractive index »[8, 18, 20], since

$$\frac{\beta}{k_0} = \sqrt{\frac{\epsilon_1\epsilon_2}{\epsilon_1+\epsilon_2}} = n_{eff} \tag{A.0.11}$$

In practice, a larger numerical aperture is obtained when the refractive index is increased in equation (A.0.9), by applying an immersion oil or water. As an example, for an oil microscope objective with a numerical aperture of 1.3, the angle of acceptance is 59°.

On the other hand, a microscope objective is an arrangement of optical elements that together works as a lens. So, it is well known that these systems are capable of performing two-dimensional Fourier transforms in the back focal plane. In this way, the microscope objective develops exactly the Fourier transform of the image placed in its front focal plane [21].

Typically the back focal plane, also known as "Fourier plane", is within the lens system of the microscope objective, so the information it provides is not easily accessible. Taking advantage of the lenses' ability to perform Fourier transforms, the information contained in the Fourier plane within the microscope objective is extracted by means of a «$4f$» system or «4f correlator».

The $4f$ system is an indispensable tool for extracting the information contained in the Fourier plane within the objective. Lens 1 of the system is placed at a distance f_1 from the Fourier planeΞ, where f_1 is the focal length of the lens. It, in turn, performs the Fourier transform of the information contained in Ξ but in the focal plane Σ', that is, the second Fourier transform of the radiation at the air-metal interface, resulting in the inverted image found in the image plane Σ.

The second lens of the system $4f$, which has a focal length f_2, is placed at a distance $f_1 + f_2$ from the first lens f_1, that is, at a distance f_2 from the plane Σ'. This lens performs the Fourier transform of the image in the Σ' plane, that is, the Fourier transform of the inverted image in the Σ plane, resulting in an image of the intensity in the space of moments.

To access and project the Fourier plane, the experimental setup is shown in Fig. A.11. The image plane of the system, Σ, is at the sample surface, that is, at the air-metal interface. Then, to excite SPPs, the first microscope objective focus the light at the structure. In order to detect the leakage radiation, the second microscope objective focused at the interface performs the Fourier transform in the back focal plane Ξ to collect the radiation emitted by the propagating SPPs.

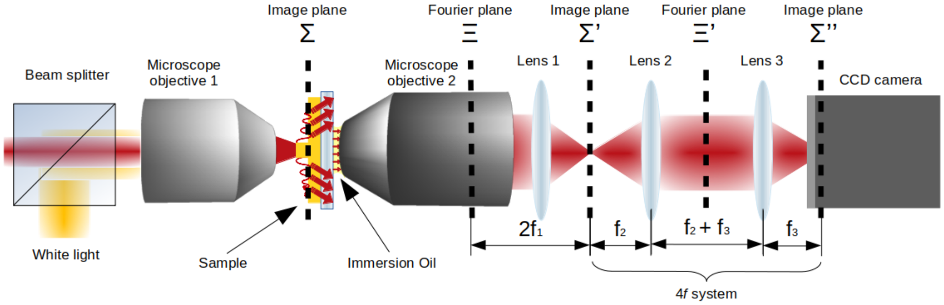

Figure A.11: Experimental setup to access to the Fourier plane.

To obtain the information of the image plane, a third lens is added so that the $4f$ system is formed by the lenses 2 and 3. This lens system projects the inverted image of the Σ' plane on the CCD camera, as shown in Fig. A.12. For this $4f$ system, lens 2 is placed so that its

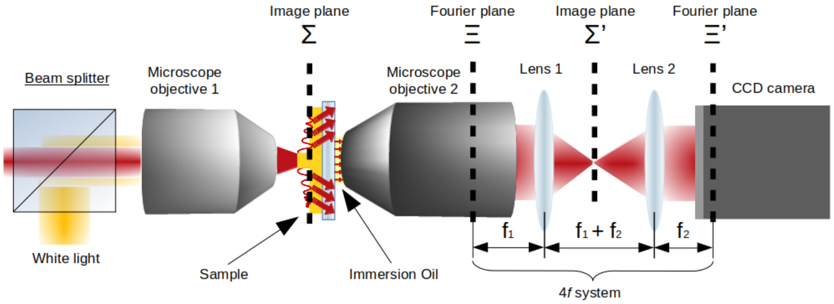

Figure A.12: Experimental setup to access to the image plane.

focus coincides with the Σ' plane, and performs the Fourier transform in the plane Ξ', as in the previous configuration. The third lens is placed at a distance f_3 from the Fourier plane Ξ', collects the information of this plane, and performs the Fourier transform, resulting the inverted image of the Σ' plane, or the image of the interface in the Σ plane. In this way, it is possible to obtain information on the propagation and characteristics of the PPS at the interface.

The information and the image obtained from the direct plane through the intensity of the detected radiation is useful to determine the direction, to calculate the imaginary part of the effective refractive index and to quantify the propagation distance of the SPPs [20]. It is also possible to measure the imaginary part of the wavenumber. As for the Fourier plane, the image obtained provides information on the distribution of the wave vectors of the PPS, its angular distribution [20], the direction of propagation and the effective refractive index.

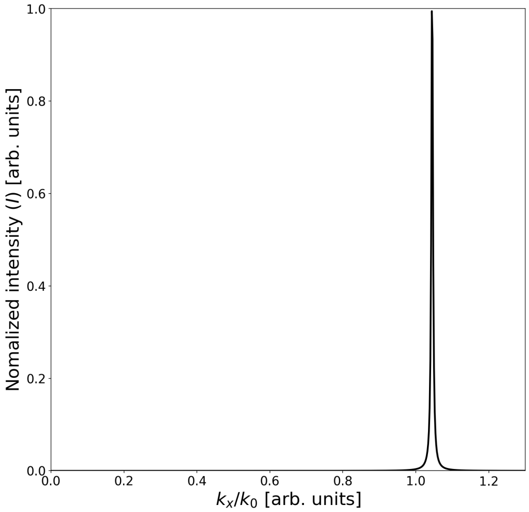

Figure A.13: Statistical distribution of wavevectors.

In the analytical problem, the SPPs propagating at the air-conductor interface are described by the equation (A.0.2). These are represented as a TM-polarized wave packet in a Fourier basis, so that in the far-field, the Fourier transform of this radiation is detected [12]. At the interface, the magnetic field is

$$H_y(\vec{r},t) = Ae^{i\beta x}e^{-k_1 d}e^{-i\omega t}, \tag{A.0.12}$$

and its Fourier transform is

$$\mathcal{F}\left\{H_y\right\} = \mathcal{H} \propto \frac{1}{i(k_x-\beta')+(\beta'')} \tag{A.0.13}$$

with $\beta = \beta' + i\beta''$. From the above, a statistical distribution of wavevector is obtained

$$I(k_x) = \frac{\text{cte}}{(k_x-\beta')^2+(\beta'')^2} \tag{A.0.14}$$

where $2\beta''$ defines the full width at half the maximum [12]. As an example, in Fig. A.13, the statistical distribution (A.0.14) is presented as a function of the parameter k_x/k_0, by introducing the corresponding values of ϵ_2 for gold into the corresponding equation (A.0.1) for $k_x/k_0 = 655$ nm.

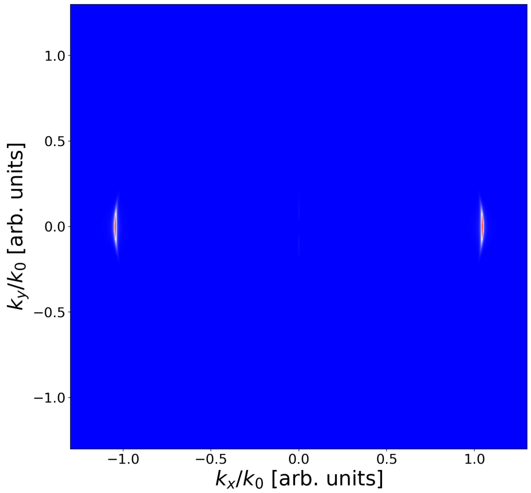

Figure A.14: SPPs at Fourier plane.

In the image, the profile along the variable k_x is shown, taking into account that the SPPs propagation is in the positive x-direction. On the other hand, Fig. A.14 shows a two-dimensional plane of the statistical distribution of wavevectors. This image corresponds to the two-dimensional extension of the equation (A.0.14), or, alternatively, to the squared module of the two-dimensional Fourier transform of the equation (A.0.12), approximating the Dirac delta function as a Gaussian function.

As it can be seen, the image in the Fourier plane of excited SPPs with light polarization parallel to the x-axis, and freely propagating, corresponds to a circumferential segment of radius

k_0. The maximum of the intensity coincides with the direction of polarization, as expected, since the charge densities move in that direction.

In the experimental part, the techniques described above were put into practice to support the analytical results.

Appendix B

Experimental setup implementation

The experimental setup for optical characterization was tested on a 50 nm thick Au thin film that was subjected to a FIBL process to fabricate a slit. This thin film was deposited on a conventional glass coverslip in the Photophysics Laboratory of ICAT-UNAM in collaboration with Dr. Citlali Sánchez Aké. The FIBL process was carried out at the Nanosciences and Micro and Nanotechnologies Center (CNMN) of the IPN, in collaboration with Dr. Adrián Martínez Rivas.

The experimental study of the nanostructures was performed at excitation beam wavelengths of 633 nm and 655 nm, so the samples were designed and fabricated to have their optimum performance at these wavelengths. The wavenumbers of the SPPs excited with these beams is equal to $\beta_{633} = (10.371 + 0.051i)\ \mu\text{m}^{-1}$ and $\beta_{655} = (9.972 + 0.032i)\ \mu\text{m}^{-1}$, which translates to a wavelength of SPPs equal to $\lambda_{633} = 605.769$ nm and $\lambda_{655} = 630.076$ nm, respectively.

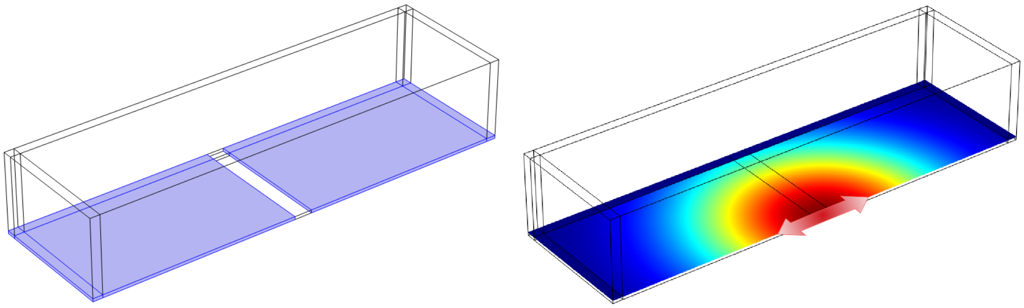

(a) Slit in thin film.

(b) Excitation beam at slit.

Figure B.1: Comsol Multyphysics Simulation scheme.

The FIBL parameters were adjusted such that the slit had a width of 300 nm. This value was chosen to achieve the optimal SPPs excitation at the mentioned wavelengths, and was determined by numerical simulations using Comsol Multiphysics® software. The physical system designed is a 50 nm thick gold (Au) thin film, in which a slit was fabricated that works as a coupler to excite SPPs. This coupler has a rectangular shape, where the numerical simulations were performed by changing the slit width to find the maximum excited electric field. Figure B.1 illustrates the simulated system.

The excitation beam has a Gaussian shape, with a wavelength of $\lambda_0 = 655$ nm, a 4 μm waist, the polarization is parallel to the x-axis and perpendicular to the slit axis, as shown in Fig. B.1b. As the beam interacts with the slit, the light is scattered and two plasmonic beams are excited, one on each side of the coupler in the light polarization direction as shown in Fig. B.2a. From the numerical data, the z component of the electric field was extracted, since this corresponds to an excited component of the SPP electric field. Then, the slit width was varied from 100 nm to 500 nm in 50 nm intervals in search of the optimum width, which was determined by finding the most intense E_z component.

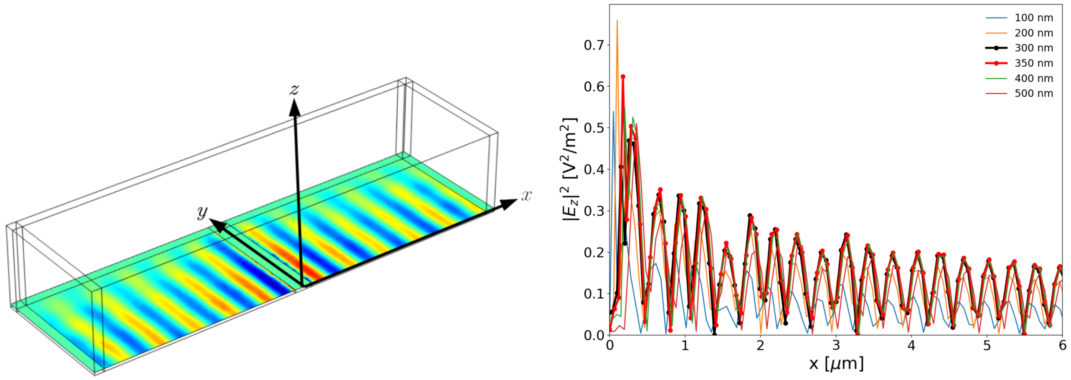

(a) E_z component of SPPs excited at thin film. (b) Intensity of E_z for different slit widths.

Figure B.2: E_z component of SPPs excited.

Figure B.2b presents the numerical results of the magnitude of the z component of the electric field for seven different slit widths. For the sake of clarity, only the data for some of them are presented. The comparison shows that E_z component magnitude is larger for $w = 300$ and $w = 350$ nm than for the rest, so a 300 nm wide slit was chosen as the experimental parameter.

The numerical data obtained were fitted to determine the E_z propagation constant. This constant was determined with a value of $\beta'_{num} = (9.977 \pm 0.016)$ μm^{-1}, equivalent to an SPP wavelength equal to $\lambda_{num} = (633.6 \pm 1)$ nm. Although the numerical results are not conclusive, they provide an outline of the system response. In this particular case, the discrepancy between the theoretical value and the numerical result is small, less than 4 nm.

Based on the numerical results, a 300 nm wide and 20 μm long aperture with the SPP coupler function was planned to be fabricated. However, experimentally the structure obtained has a width of 347 nm and length of 10 μm. Figure B.3 shows a photograph of the nanostructure obtained by FIBL taken by the experimental setup. In addition to the coupler, two 190 nm wide and 5 μm long slits were fabricated on one side of the coupler.

As mentioned above, the optical tests performed on this sample were at wavelengths of 633 nm and 655 nm, where images of the leakage radiation were obtained both in the image

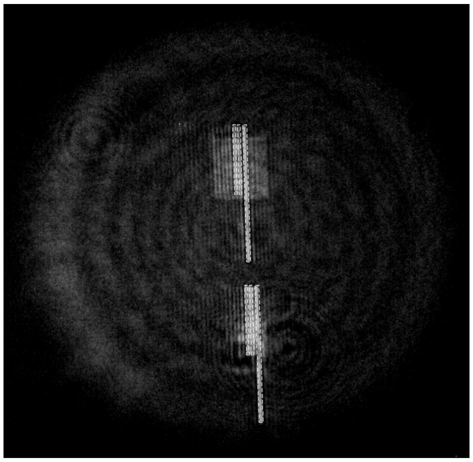

Figure B.3: Nanostructure fabricated by FIBL.

plane and in the Fourier plane. Theoretically, the effective refractive indexes for an interface formed by air and an Au thin film with no surface defects, for the wavelengths mentioned, are $n_{eff-633} = 1.045 + 0.005i$ and $n_{eff-655} = 1.040 + 0.003i$, respectively.

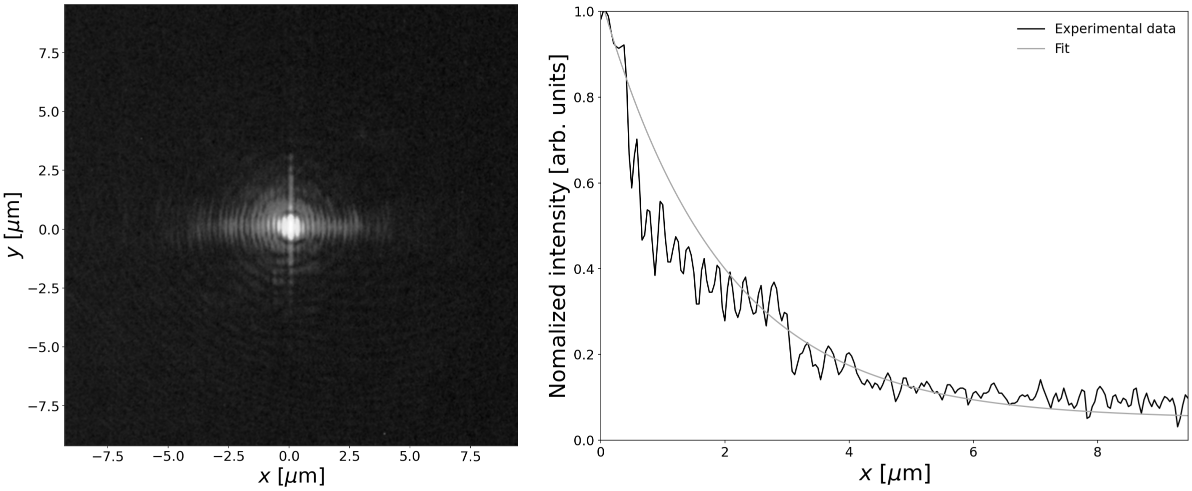

(a) Image of LRM.

(b) Intensity profile of SPPs excited.

Figure B.4: Leakage radiation microscopy (LRM) in the image plane of SPPs excited at $\lambda = 633$ nm.

Figure B.4 shows the intensity in the image plane of the leakage radiation of SPPs excited at a wavelength of 633 nm. Figure B.4a is the two-dimensional image acquired with the CCD camera, while plot B.4b is the intensity profile along the x-axis at $y = 0$. In the two-dimensional image, the two excited plasmonic beams are visible, one on each side of the coupler.

The electromagnetic field strength of SPPs decays exponentially as $e^{-2\beta x}$, then the experimental data in Fig. B.4 were fitted to a function of the form

$$I(x) = Ae^{-2Bx} + C. \tag{B.0.1}$$

Data analysis yields $A = 0.982 \pm 0.064$, $B = 0.258 \pm 0.013$ and $C = 0.103 \pm 0.011$. With these fitting parameters, it is obtained that $\beta''/k_0 = 0.026 \pm 0.001$ and the SPP propagation length is $L_{SPP} = (1.937 \pm 0.098)\mu$m.

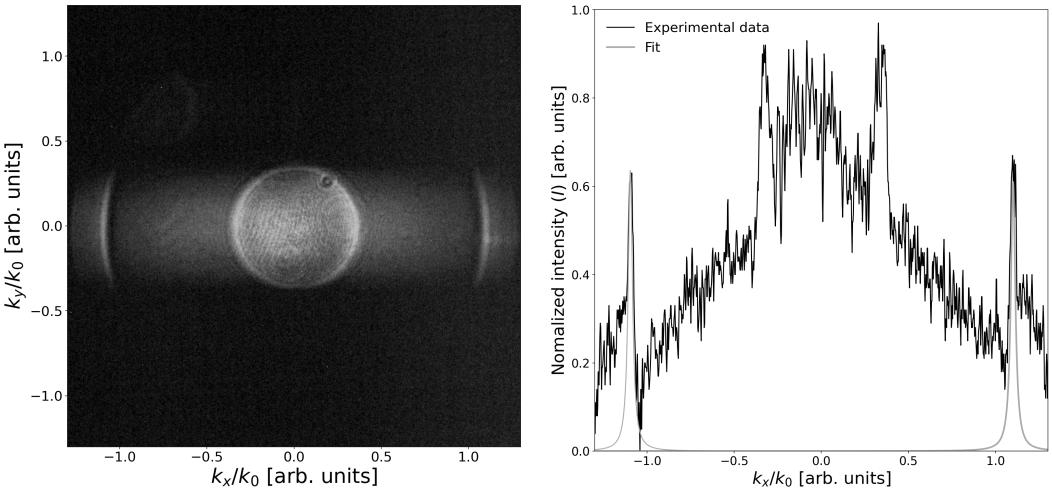

(a) Image of LRM.

(b) Intensity profile os SPPs excited.

Figure B.5: LRM in the Fourier plane of SPPs excited at $\lambda = 633$ nm.

Accessing the Fourier plane, the image shown in Fig. B.5a was acquired, while the intensity profile in that plane is shown in Fig. B.5b along the k_x/k_0 axis at $k_y/k_0 = 0$ with its respective fit. From the parameters obtained from the data fit, for the propagating SPPs on the right-hand side, the effective refractive index is $\beta/k_0 = (1.100 \pm 0.001) + (0.031 \pm 0.003)i$, and for the SPPs on the left-hand side, the obtained result is $\beta/k_0 = (1.100 \pm 0.001) + (0.021 \pm 0.003)i$.

Considering both values, the average effective refractive index is $n_{eff-633} = \beta/k_0 = (1.100 \pm 0.001) + (0.026 \pm 0.003)i$. This implies that the imaginary part of the propagation constant is $\beta'' = (0.258 \pm 0.030)$ μm^{-1}, which corresponds to a propagation length $L_{SPP} = (1.937 \pm 0.225)$ μm .

Between the real part of the theoretical and experimental effective refractive index, there is a difference of 0.05868, which translates into a difference in angle of 2.22 °in the Kretschmann configuration. Also, the discrepancy in the imaginary part of the effective refractive index between the theoretical and experimental values is remarkable. The above may be a product of SPPs scattering due to the natural surface roughness of the Au thin film surface, in addition to the damage it suffered from being subjected to the ion beam during the lithography process.

On the other hand, it is important to highlight the consistency between the experimental values obtained for the imaginary part of the effective refractive index obtained both in the image plane and in the Fourier plane. From the information acquired in the image plane, it was determined that $\beta''/k_0 = 0.026 = 0.001$, while from the information acquired from the Fourier plane, the result is $\beta''/k_0 = 0.026 \pm 0.003$.

The propagation length, experimentally determined from the quantity β'', is $L_{SPP} = 1.937$ μm, while the theoretical value is 9.804 μm. It is pertinent to clarify that the theoretical values mentioned above are only used as a reference, since the experimental system is far from being an ideal system as the one studied theoretically.

In the experimental results, the propagation length of the SPPs is affected by the defects on the thin film surface, resulting in a decrease of the propagation length, in addition to causing a broadening of the peaks in the intensity profile of the SPP in the Fourier plane. However, the experimental setup is a tool that allows extracting information about the plasmonic properties of the physical systems mentioned above.

References

[1] Gemma Rius Suñé. *Electron beam lithography for Nanofabrication.* PhD thesis, Universitat Autònoma de Barcelona, 2008.

[2] Joseph I. Goldstein, Dale E. Newbury, Joseph R. Michael, Nicholas W.M. Ritchie, John Henry J. Scott, and David C. Joy. *Scanning Electron Microscopy and X-Ray Microanalysis.* Springer, New York, 2018.

[3] Lucille A. Giannuzzi and Fred A. Stevie, editors. *Introduction to focused ion beams: instrumentation, theory, techniques and practice.* Springer, Boston, MA, 2004.

[4] C. A. Volkert and A. M. Minor. Focused ion beam microscopy and micromachining. *MRS Bulletin*, 32(5):389–399, 2007.

[5] Zhiming M. Wang, editor. *FIB Nanostructures.* Lecture Notes in Nanoscale Science and Technology. Springer, Cham, 2013.

[6] Nan Yao and Zhong Lin Wang, editors. *Handbook of Microscopy for Nanotechnology.* Springer, Boston, MA, 2005.

[7] Nezih Pala and Mustafa Karabiyik. *Electron Beam Lithography (EBL)*, pages 1033–1057. Springer Netherlands, Dordrecht, 2016.

[8] Stefan A. Maier. *Plasmonics: Fundamentals and Applications.* Springer, 2007.

[9] H. Raether. *Surface Plasmons.* Springer, Berlin, 1988.

[10] Anatoly V. Zayats, Igor I. Smolyaninov, and Alexei A. Maradudin. Nano-optics of surface plasmon polaritons. *Physics Reports*, 408(3):131–314, 2005.

[11] Takashi Wakamatsu and Kazuhiro Saito. Interpretation of attenuated-total-reflection dips observed in surface plasmon resonance. *J. Opt. Soc. Am. B*, 24(9):2307–2313, Sep 2007.

[12] A. Drezet, A. Hohenau, D. Koller, A. Stepanov, H. Ditlbacher, B. Steinberger, F.R. Aussenegg, A. Leitner, and J.R. Krenn. Leakage radiation microscopy of surface plasmon polaritons. *Materials Science and Engineering: B*, 149(3):220–229, 2008. E-MRS 2007 Spring Conference Symposium A: Sub-wavelength photonics throughout the spectrum: Materials and Techniques.

[13] P. B. Johnson and R. W. Christy. Optical constants of the noble metals. *Phys. Rev. B*, 6:4370–4379, Dec 1972.

[14] V.M. Shalaev and S. Kawata, editors. *Nanophotonics with Surface Plasmons*. Advances in Nano-Optics and Nano-Photonics. Elsevier, Amsterdam, 2007.

[15] Sergey I. Bozhevolnyi, John Erland, Kristjan Leosson, Peter M. W. Skovgaard, and Jørn M. Hvam. Waveguiding in surface plasmon polariton band gap structures. *Phys. Rev. Lett.*, 86:3008–3011, Apr 2001.

[16] Sergey I. Bozhevolnyi, Valentyn S. Volkov, and Kristjan Leosson. Localization and waveguiding of surface plasmon polaritons in random nanostructures. *Phys. Rev. Lett.*, 89:186801, Oct 2002.

[17] A.J. Braundmeier and H.E. Tomaschke. Observation of the simultaneous emission of roughness-coupled and optical-coupled surface plasmon radiation from silver. *Optics Communications*, 14(1):99–103, 1975.

[18] C. E. García-Ortiz. *Diseño y caracterización de dispositivos plasmónicos*. PhD thesis, Universidad Autónoma de Nuevo León., 2013.

[19] Microscopyu. Numerical aperture, 2017. Last accessed 5 January 2022.

[20] E. Pisano-Chávez. *Plasmónica clásica: control de la propagación de ondas en escala nanométrica*. PhD thesis, Centro de Investigación Cientfica y de Educación Superior de Ensenada, 2016.

[21] J.W. Goodman. *Introduction to Fourier Optics*. McGraw-Hill physical and quantum electronics series. W. H. Freeman, 2005.